ISSN (Online): 3005-5571
ISSN (Print): 3005-5563
Vol. 3, Issue 2
(January - June 2026)

UCP Journal of Science and Technology(UCP-JST)

HEC Recognized (Y Category)

Volume 3

Issue 2

Faculty of Science and Technology
&
Faculty of Pharmaceutical Sciences

University of Central Punjab, Lahore, Pakistan

Advisory Board
International Members

National Members

Copyright

Subscription Charges

National: PKR 1000 per issue

International: US$ 200 per issue

Acknowledgment

We are pleased to present Issue 2, Volume 3 of the *UCP Journal of Science & Technology (UCP-JST).* This issue reflects the continued dedication of our editorial team, reviewers, and authors in maintaining the journal's academic quality.

We are proud that UCP-JST has been recognized as a Y Category journal by the Higher Education Commission (HEC) of Pakistan, affirming our commitment to rigorous scholarly standards. Moving forward, we remain focused on enhancing the journal's impact and progressing toward higher levels of recognition.

UCP-JST serves as an open platform for the dissemination of innovative research in science and technology. While published works may be cited with proper acknowledgment, copyright responsibility rests with the respective authors. On behalf of the editorial board, I sincerely thank all contributors for their valuable support and trust.

Sincerely,
Dr. Hafiza Rizwana Kausar
Editor-in-Chief
UCP -JST

Disclaimer

UCP Journal of Science & Technology (UCP-JST) primarily focuses on providing a platform to promote and contribute to science and technology; however, editors, reviewers, and the publisher do not accept any legal responsibility for errors, omissions, or claims, nor do they provide any warranty, express or implied, with respect to published information. All articles published in the UCP-JST can be cited with due acknowledgement. The author will take responsibility if any copyright infringement or any other violation of any law is committed by publishing the research work by the author.

UCP Journal of Science and Technology
Vol. 3, Issue 2 (January - June 2026)
Journal website: http://ojs.ucp.edu.pk/index.php/ucpjst/index

Table of Contents

UCP Journal of Science and Technology
Vol. 3, Issue 2 (January - June 2026)
Journal website: http://ojs.ucp.edu.pk/index.php/ucpjst/index

Feed Restriction Impairs Immunity and Lymphoid Organ Development in Broiler Chicks: Enabling Accurate Body Weight Prediction Through Machine Learning

Ghulam Mustafa[1,3#], Aliya Alvi[3#], Sara Hayee[1#], Azka Zafar[2#], Usama Khalid[4], Khajid Ullah Khan[1], Ihtisham Jamil[1], Deok-Won Kim[3], Ramesh Kumar[3], Yasser Mustafa Butt[1*], Muhammad Tariq Zahid[1*], Byong-Hun Jeon[3*]

Abstract

This study evaluated how limiting the amount of food that chickens could consume influenced their growth rates, immune system responses, and body mass estimates. Eighty chickens were started at 1 day old and raised for 56 days. All of the chickens were grouped into four different groups. On days 21-35, each chicken from groups A, B, and C had unlimited access to food during either six (Group A), twelve (Group B), or twenty-four (Group C) hours a day. Each chicken in Group D was fed unrestricted as the control. Limitations on feeding resulted in significant alterations to several haematologic parameters ($p < .01$); these changes included a decrease in white blood cell count in chickens that experienced severe levels of stress; an increase in the ratio of heterophils to lymphocytes; and a decrease in serum titer antibodies against Newcastle disease virus compared to those in the control group. Significant reductions in weight of lymphoid tissues (the bursa of Fabricius, thymus, spleen) and an elevation in mortality rate ($p < .05$) in chickens that consumed limited amounts of feed were also found. Mortality rates were especially high in chickens from all of the restricted feed groups after they were challenged by exposure to Newcastle disease virus. Machine learning models were created to estimate body mass based on an expanded set of physiological variables. Limitation of feed significantly impairs broiler immune systems and growth. Regression models, including ridge regression, XGBoost regression model, and gradient boosting model, provided the best accuracy ($R^2 > 0.92$) when used to estimate body weight under conditions of stress. Deep neural networks and lasso regression models provided poor accuracy. These models provide a reliable method to assess poultry production under conditions of feed limitations.

Keywords: Angara Disease; Bursal Disease; Infectious Bronchitis; Total Leukocyte Count; Newcastle Disease

[1]Department of Zoology, Government College University Lahore, Lahore, 54000, Pakistan.
[2]School of Basic Medical Sciences & School of Public Health, Faculty of Medicine, Yangzhou University, Yangzhou, 225009, China.
[3]Department of Earth Resources and Environmental Engineering, Hanyang University, Seoul, 04763, South Korea.
[4]Computer Science Department, Hanyang University, Seoul, 04763, South Korea.
[#]These authors contributed equally.
[*]Correspondence: Byong-Hun Jeon (bhjeon@hanyang.ac.kr); Muhammad Tariq Zahid (tarizahid@hanyang.ac.kr); Yasser Mustafa Butt yasserbutt1@yahoo.com
Received: 07 March 2026; Received in revised form: 02 June 2026; Accepted: 16 June 2026.
Available online: 13 July 2026.

DOI: https://doi.org/10.24312/ucp-jst.03.02.830

1. Introduction

The majority of the world's population depends on poultry, particularly broiler chickens, for their protein intake, as they have been genetically engineered to grow quickly and be fed efficiently (Gaweł et al., 2022; R Mohammadalipour et al., 2017). However, due to logistical issues including delays in delivering food to them due to transportation, hatchery processing, and delivery to farms, broilers are often deprived of feed for 6 to 48 hours after hatching (Abou-Elnaga & Selim, 2018; Shinde Tamboli et al., 2018). As the initial days after hatching represent an important developmental stage; however, the middle-growth phase (days 21 through 35) represents a critical period for rapid metabolic needs and somatic development. During this time frame, even minor changes in environment and nutrition can dramatically affect how the bird develops physiologically (Bortoluzzi et al., 2013). Feed restrictions applied at this time will reduce the amount of energy the chicken has available to use for both maintaining itself and developing its muscles and immune system while it grows ("Evaluation of different changes in diurnal feed restriction for broilers," 2021; Kouki et al., 2016). Even though there are some reports that indicate that the application of short term physical restriction could potentially cause the birds to exhibit compensatory growth patterns in later stages of life, if the birds are subjected to prolonged or extreme levels of nutrient deprivation throughout this 21 to 35 day phase, the birds will likely experience long term depression in total body weight gain and irreversible damage to their immune organs which would make them highly vulnerable to disease causing pathogens (Bortoluzzi et al., 2013; Saber et al., 2011).

Early feed restriction has an impact on the animals' health and also the long-term health of the business. The effects of extended feed restriction can be detrimental to many physiological systems, such as growth, body weight, gastrointestinal function, and musculoskeletal development (Jawad, 2023). Early post-hatch feed restriction (first 36 hours) causes changes in enterocyte populations, hampers gut morphological development, and damages the intestinal barrier function (Hollemans et al., 2018; Jacobs et al., 2016; Kang et al., 2018). Starvation has been shown to increase the colonization and maturation of lymphoid tissue; particularly, the bursa of Fabricius plays a critical role in the development of B and T cells in avian species (Madej et al., 2024). Early onset of malnutrition results in impaired immunocompetence, reduced potential weight gains ($p < 0.05$), increased disease vulnerability, and elevated death rates during extended periods of refeeding (Liu et al., 2020; Panda et al., 2015; Selim et al., 2021; Wijnen et al., 2021).

Newcastle Disease Virus (NDV) presents a significant risk to global poultry producers through respiratory diseases, suppression of immunity, and loss of profit (Oviedo-Rondon et al., 2013). It is common practice in poultry to administer live NDV vaccines at an early age in the chicks' lives. However, the efficacy of these vaccinations depends upon proper development of the immune system (Al-Abdullatif et al., 2024). Poultry that have limited nutrition will most likely not develop a proper response when administered antibodies or cells; therefore, they may be more susceptible to disease while in the field (Gholami et al., 2020).

A subset of Data Science, "Machine Learning," is an area where computers can use the information provided by large databases to learn and forecast events based upon this information. As a result, machine learning methods improve predictive capabilities through adaptation to new data. Traditional statistical approaches will be valuable; however, these traditional statistical approaches do not perform well when there are numerous complex relationships or many individuals are upset about one particular event.

Therefore, we must research whether machine learning provides a viable alternative, since machine learning has been successful in predicting various outcomes, particularly those associated with large, complicated databases. Machine learning (ML) is an effective way to analyze multivariate data to develop predictions related to complex biological features. Furthermore, machine learning models can identify non-linear associations and interactions within physiologic measures that can help determine how stress affects development (Kuhle et al., 2018). Recent studies in poultry science have demonstrated that machine learning models can be used to determine the amount of weight in birds; the probability of disease in birds; and the efficiency of production in poultry using data obtained from the bird's blood samples and its management history. However, very little research has investigated using machine learning to predict the body weight of broilers under conditions of feed restriction stress, and even less research has assessed the performance of such models using data sets that were not part of the original training set to evaluate model bias due to overfitting at smaller sample sizes. (Ghosh et al., 2021; Pirompud et al., 2024).

The objective of this study was to comprehensively evaluate the influence of feed deprivation durations (6, 12, and 24 hours daily during the critical period days 21-35) on the growth performance, immune response to NDV vaccination, hematological parameters, lymphoid organs, and mortality rate in broiler chicks. Develop and compare traditional (Linear, Ridge, Lasso Regression), ensemble (Random Forest, Gradient Boosting, XGBoost, AdaBoost, Decision Tree), and deep learning (DNN) regression models for predicting body weight from physiological and management variables using an augmented dataset, with rigorous evaluation on held-out test data.

2. Materials and Methods

2.1 Ethical Statement

All experimental procedures were approved by the Institutional Bioethics Committee at Government College University, Lahore, Pakistan. All methods followed institutional and national guidelines for humane animal treatment and care.

2.2 Broiler Chicks Purchase and Rearing

One-day-old broiler chicks of uniform weight (40-45 g) and feed were obtained from M/S Sabir's Poultry Breeders and transferred to the Zoology Department, GC University Lahore, Pakistan. The chicks were reared at 35 °C in an artificial brooder (1 sq ft/chick). A total of 80 chicks were randomly assigned to four groups (A, B, C, D), with 20 chicks per group. The vaccination schedule was as follows: day 7, Infectious Bursal Disease (IBD) vaccine; day 14, Newcastle Disease (ND) vaccine and Infectious Bronchitis (IB) vaccine; day 21, Hydropericardium Syndrome (HPS) vaccine (Table 1). Chicks had ad libitum access to a standard broiler finisher diet and water except during designated feed restriction periods.

Table 1. The vaccination schedule of broiler chicks.

Age (d)	Vaccine	Route
7	IBD	Drinking water
14	IB/ND	Eye drops
21	HPS	S/C inoculation

Table 2. Schedule of feed deprivation and NDV vaccination of broiler chicks.

Treatment	No. of birds	Age (d)	Group A	Group B	Group C	Group D
NDV Vaccination	All birds	5 and 21	+	+	+	+
Feed deprivation 6:00 a.m.–12:00 p.m.	20	21 to 35	+	-	-	-
Feed deprivation 6:00 p.m.–6:00 a.m.	20	21 to 35	-	+	-	-
Feed deprivation 6:00 p.m.–6:00 a.m.	20	21 to 35	-	-	+	-
Feed provided ad libitum	20	21 to 35	-	-	-	+
50% birds (NDV inoculated)	50% chicks	21 to 35	+	+	+	-

2.3 Influence of Feed Deprivation on Broiler Chicks

On the 21st day of age, the chicks were randomly assigned to four groups. Group (A) was 6 h (6 a.m. to 12 p.m.), group (B) for 12 h (6 a.m. to 6 p.m.), group (C) for 24 h (6 a.m. to 6 a.m.), and the control group (D) was given feed ad libitum (Table 2). Water was available ad libitum to all groups throughout the experimental period. The body weight and feed intake of stressed birds were recorded weekly and compared with those of the control group. The feed conversion ratio was calculated by equation (1) (Dosu et al., 2023; Wang et al., 2020). Here, ā means average consumed feed (g), and ā represents the average increase in weight (g).

2.4 Hematological Assessment

The virulent NDV was used to inoculate 50% of the chicks in the experimental group on the 36th day. Blood samples were collected on the 37th day from non-inoculated and inoculated chicks for several parameters, such as Differential Leukocyte Count (DLC), including Heterophil/lymphocyte ratio, and Total Leukocyte Count (TLC) (Thiam et al., 2022). The Heterophil-to-Lymphocyte Ratio (H/L) was calculated by Eq. 2 (Farghly et al., 2019).

2.5 Serum Analysis for NDV Antibody

NDV Hemagglutination inhibition (HI) antibody titers were measured on the 56th day post-infection using a standard protocol (Abdi et al., 2016). The serum sample was serially diluted in PBS buffer; 4 HA units of ND virus were added to each dilution. 0.5% Chicks CRBC suspension was added, and the test plates were re-incubated at room temperature for 20-30 min. HI titers were expressed as the reciprocal of the highest serum dilution inhibiting hemagglutination. Geometric Mean Titers (GMT) were calculated for each group (Abdi et al., 2016).

2.6 Morphometry of the Lymphoid Organs

At the 50th day of age, 5 birds were randomly selected and humanely euthanized. The lymphoid organs (thymus, spleen, and bursa of Fabricius) were aseptically removed, examined for pathological lesions, and weighed (Islam et al., 2023). On day 56 of age, all remaining birds in each group (approximately 15 per group after losses) were euthanized. Lymphoid organs were

collected, weighed, and examined. Organ weights were recorded and expressed as absolute weight (g) and relative weight (% of body weight).

2.7 Hypersensitivity Reaction (Delayed-type)

On day 56, cellular immune response was assessed via delayed-type hypersensitivity reaction using phytohemagglutinin-P (PHA-P). Pre-injection wattle thickness (left wattle, measured ≤1 mm) was recorded using a digital caliper. Each bird received an intradermal injection of 100 µL of PHA-P solution (2 mg/mL in sterile PBS) into the left wattle. Post-injection wattle thickness was measured at 24 hours using the same caliper. DTH response was expressed as the difference between post- and pre-injection measurements (in mm) (Yadav et al., 2021).

2.8 Machine Learning Modeling

This research focused on finding the impact of varying feed restrictions on animal physiology. The feed restriction durations are 0, 6, 12, and 24 hours, and the goal is to predict the animal's body weight. Some major parameters being assessed are weights, blood profiles, immune responses, and mortality rates, and body weight in grams (g) is used as the target prediction.

Hence, the initial sample size was small; to overcome this, the synthetic minority oversampling technique (SMOTE) was used. To increase model robustness, Gaussian noise with a level of 0.02 is added to numerical features (Sağlam & Cengiz, 2022). To increase the dataset size by twofold, bootstrap resampling is used, and for data normalization, the RobustScaler method is used (Ahsan et al., 2021).

A variety of machine learning models were used to predict body weight, including Linear, Ridge, and Lasso Regression, as well as Decision Tree, Random Forest, Gradient Boosting, AdaBoost, XGBoost Regressors, and a Deep Neural Network (DNN) (Bansal et al., 2022). The Deep Neural Network (DNN) architecture consists of three layers: an input layer with 64 neurons employing ReLU activation, a hidden layer with 32 neurons employing ReLU activation, and an output layer with a single neuron (Singh et al., 2023). A dropout rate of 0.2 was used to reduce overfitting, and the model was compiled with the Adam optimizer and mean squared error as the loss function (Anh et al., 2023). Early stopping was implemented after 10 epochs, allowing the model to revert to the best weights based on the lowest validation loss (Razali et al., 2025). Models were evaluated using metrics such as R-squared (R^2), Mean Absolute Error (MAE), Root Mean Squared Error (RMSE), Mean Absolute Percentage Error (MAPE), Explained Variance Score (EVS), and Accuracy. The models were trained on the augmented, scaled dataset, and the predictions were compared with the actual body weight measurements (Pal & Dutta, 2024).

2.9 Analysis of Experimental Data

Biological data were analyzed using SPSS Statistics v27 (IBM Corp., Armonk, NY, USA). Differences among treatment groups were compared using a one-way ANOVA followed by Tukey's post hoc test. Effect sizes for the ANOVA were determined using partial eta-squared, and 95% confidence intervals (CIs) were generated for mean differences. All results are expressed as mean ± standard deviation (SD). Differences among treatment groups (A, B, C, D) were compared using a one-way ANOVA followed by Tukey's honest significant difference (HSD) post hoc test for pairwise comparisons. Significance was set at $P < 0.05$ throughout (Ogbu, 2020). Machine learning model performance was evaluated on the test set using Python (v3.10) with scikit-learn and TensorFlow libraries; no statistical significance testing was performed on ML metrics (R^2, MAE, etc.), as these represent

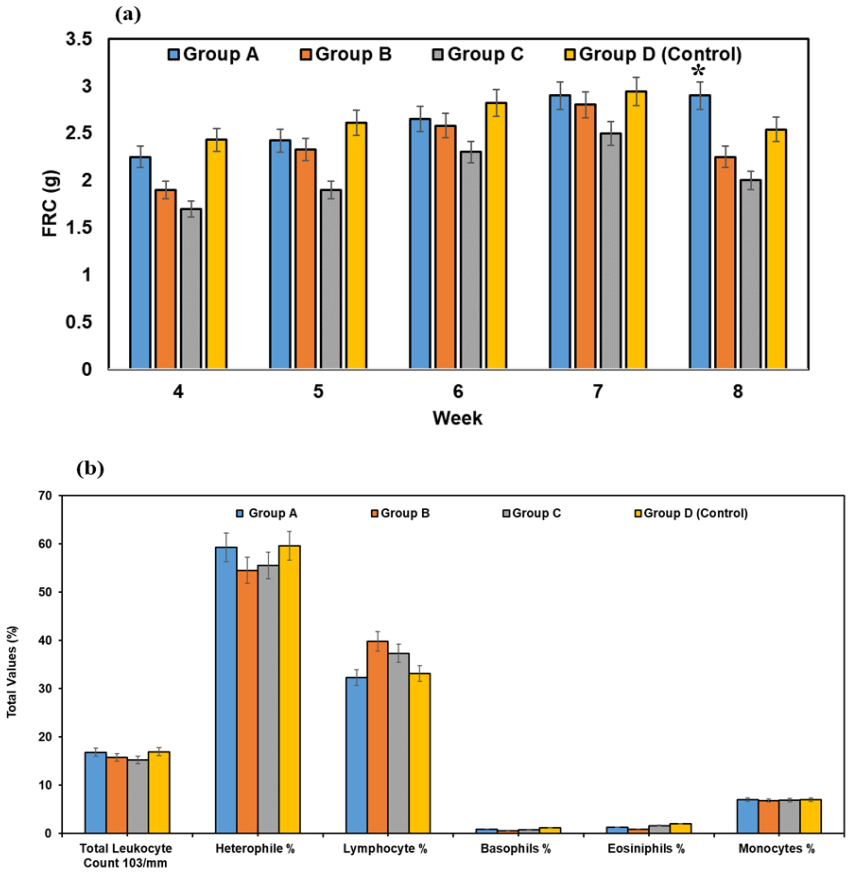

Figure 1. FCR of broiler chicks of feed restriction, Stressed and unstressed Groups in different Weeks (a). Heterophil to Lymphocyte Ratio (b) and comparison of Total Leukocyte count (TLC) Stressed and Unstressed Broiler Groups (c).

deterministic predictions on a fixed test set.

3. Results and Discussion

This research aimed to determine the extent to which feed restriction-induced stress was responsible for humoral and cellular immune responses and growth performance in broiler chicks. The primary purpose of this research was to investigate the influence of these stressors on the humoral and cellular immune responses of chicks in response to NDV vaccination.

3.1 Feed Restriction Effects on Feed Conversion Ratio of Broiler Chicks

Feed conversion ratios were recorded before and after stress in all groups. The FCR values recorded at the 4th, 5th, 6th, 7th, and 8th week of all groups as group A (2.25, 2.42, 2.65, 2.9, and 2.4), B (1.9, 2.33, 2.58, 2.8 and 2.25), C (1.7, 1.9, 2.3, 2.5 and 2.00) and D (2.43, 2.16, 2.82, 2.94 and 2.54). During the active stress period (weeks 4 to 6), the feed conversion ratio (FCR) of the restricted groups (A, B, and C) was generally lower (i.e., more efficient) than that of the control group (D), reflecting a compensatory metabolic adaptation to limited feed availability. However, during the post-restriction and viral challenge phase (week 8), FCR values fluctuated; group A exhibited an increased FCR compared to the unstressed control. Overall, the data indicate that

while short-term restriction may lower FCR, severe restriction followed by immune challenge disrupts this efficiency (Figure 1a). These results agree with the study that reported feeding groups had a lower feed conversion ratio than the control group fed ad libitum (Lu et al., 2022). The present study found that FCR values decreased in feed-restricted groups compared with the control group and concluded that feed restriction did not affect FCR in stressed chicks.

3.2 Feed Restriction Effects on Hematological Values of Broiler Chicks

Hematological profiling revealed a non-linear relationship between feed restriction severity and hematological parameters. In Group A (6 h restriction), standard stress responses were observed, marked by a significant decrease in lymphocytes (32.30 ± 1.15%) and an elevated H/L ratio (1.84 ± 0.29) compared to the control. Conversely, in the more severely restricted groups B (12 h) and C (24 h), lymphocyte percentages unexpectedly increased (39.8 ± 0.2% and 37.33 ± 1.33%, respectively), resulting in lower H/L ratios (1.37 ± 0.38 and 1.49 ± 0.26). This suggests that severe feed deprivation may trigger different hematological survival mechanisms than mild restriction. These findings contrast with typical stress models, which typically report an enhanced H/L ratio under feed restriction. Basophil counts were 0.9 ± 0.2, 0.5 ± 0.2, 0.7 ± 0.1, and 1.2 ± 0.057; these results showed that basophils decreased in all sets compared with the control group. The count of Eosinophils was 1.30 ± 0.3, 0.9 ± 0.0577, 1.62 ± 0.12, and 2 ± 0.5; a significant difference was observed in all groups. Similarly, Monocyte percentages were recorded at 6.99 ± 0.51, 0.82 ± 0.2886, 6.91 ± 0.36, and 07.00 ± 1, respectively, and H/L Ratio (Heterophile and Lymphocyte) was observed as 1.84 ± 0.29, 1.37 ± 0.38, 1.49 ± 0.26, and 1.80 ± 0.46, respectively. Similar values of monocytes, 6.99 ± 0.51, 6.91 ± 0.36, and 07.00 ± 1, were observed in all experimental groups A, C, and D. There was no significant difference, but it was lower in group B by 6.82 ± 0.29. The values of eosinophils were lessened in all experimental sets compared to set D (control). The H/L Ratio was observed to be greater in Group A (1.84 ± 0.29), while decreased in Group B (1.37 ± 0.38) and C (1.49 ± 0.26) than in control Group D (1.80 ± 0.46), which showed the impact of feed restriction as a stress factor on the broiler chicks (Figure 1b). A similar report showed that the H/L ratio was significantly higher on the 42nd day in feed-restricted groups than in the control group D (Kalia et al., 2017). The present study agrees with the study who reported earlier that H/L was significantly decreased by feed restriction in broiler chicks (Bhadauria & Bhanja, 2017).

3.3 Feed Restriction Effects on Humoral Immune Response

At the 36th day of age, GMT was recorded for all NDV-vaccinated groups A, B, C, and D as 7.5 ± 0.5, 7 ± 1.00, 6.2 ± 0.26, and 8.5 ± 1.26, respectively. These values showed that GMT was significantly ($p<0.01$) higher in group D (control) nourished ad libitum during the experimental tenure than in all other groups.

At the 56th day, GMT was again recorded in all groups after the viral challenge. GMT values recorded for all groups A, B, C, and D were 5.6 ± 0.1, 5.8 ± 0.26, 5.43 ± 0.38, and 8.75 ± 0.25, respectively. GMT values were significantly lower ($p<0.01$) in all stressed and virus-inoculated sets than in group D (control). A significant difference ($p<0.01$) in GMT values was observed before virus injection and post-challenge in all groups compared with the control group (Figure 2a). The current research indicated that feed restriction influenced the cellular response of broiler chicks. A higher thickness was observed in Group D. These findings were consistent with those

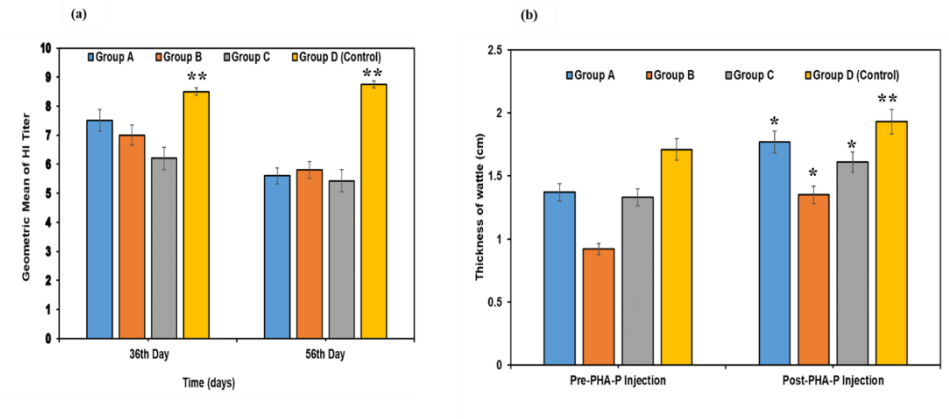

Figure 2. Feed restriction affects the NDV HI titer of NDV-vaccinated broiler chicks on the 36th and 56th day (a). Wattle thickness Pre- and Post-PHA-P injection in broiler chicks (b).

showing that feed restriction significantly reduces the cellular response in broiler chicks (Jang et al., 2009; Orso et al., 2019).

3.4 Feed Restriction Effects on the Cellular Immune Response of Broiler Chicks

The wattle width recorded before injection of PHA-P in all Groups, as Group A (1.37 ± 0.11), B (0.92 ± 0.02), C (1.33 ± 0.03), and D (1.71 ± 0.19), showed a significant sharp difference between the control set D and all experimental sets A, B, and C. The cellular immune response was recorded at the 56th day of age; post-PHA-P injection thickness of the wattle was measured (centimeter) in groups A (1.77 ± 0.27), B (1.35 ± 0.15), C (1.61 ± 0.09), and D (1.93 ± 0.07). Their differences were indicated. A significant difference ($p<0.01$) in the thickness of Wattle pre- and post-PHA-P injection was observed (Figure 2b).

3.5 Feed Restriction Effects on the Overall Mortality

All the chicks were NDV-vaccinated and exposed to the restricted feed stress factor. Mortality was significantly higher ($p<0.05$) in the feed-restricted groups than in the control group D, peaking sharply post-NDV challenge (Figure 3a). These data indicate that while the chicks could barely survive the metabolic stress of starvation, the compounded stress of a live viral challenge overwhelmed their already depleted physiological reserves, leading to systemic failure. A high metabolic rate during fasting increased the mortality rate of broiler chicks (Sahraei, 2014). However, feed restriction did not affect mortality in broiler chicks (R. Mohammadalipour et al., 2017).

3.6 Feed Restriction Effects on the Lymphoid Organs of Broiler Chicks

Feed deprivation effects were observed in lymphoid organs, which consist of the spleen, the bursa of Fabricius, and the thymus of broiler chicks, with the help of morphometry. The morphometric values have been recorded. The mean weight of the spleen in different stressed groups A, B, C, and unstressed group D was noted at 1.85 ± 0.1, 1.61 ± 0.03, 1.33 ± 0.03, and 2.90 ± 0.1, respectively. The mean weight of the spleen in group D (2.90 ± 0.1 g) was significantly greater than in the experimental groups ($p < 0.01$, $\eta^2 = 0.65$, 95% CI [2.50, 3.30]) (Figure 3b). These results are consistent with those of Hangalapura et al. (2005), who reported that the masses of the bursa and spleen were notably lower in feed-restricted broiler chicks.

The mean weight value of the Bursa of Fabricius in Group A was 1.63 ± 0.13, Group B 1.13 ± 0.02, Group C 0.72 ± 0.07, and Group D 1.92 ± 0.07 was observed at 56th day of age. The mean bursa weight

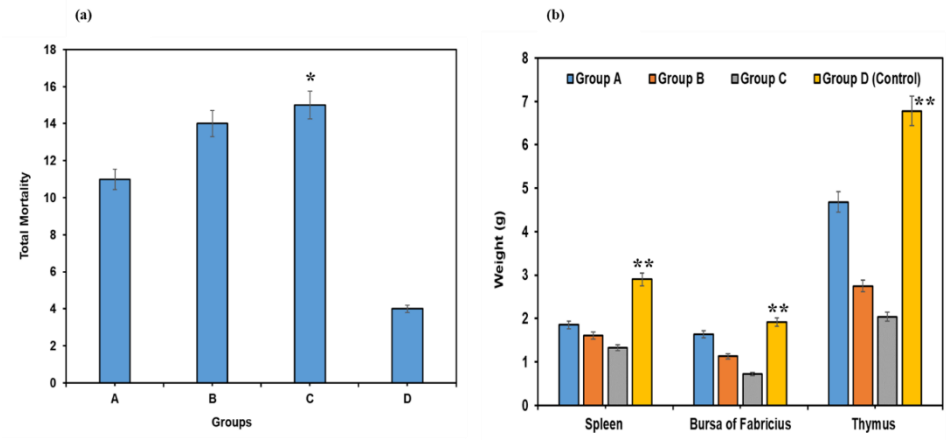

Figure 3. Total mortality in all groups (a). Morphometry of Lymphoid Organs of Feed Restricted Unstressed and Stressed Broiler Groups (b).

was significantly lower in all feed-restricted groups (A, B, and C) compared with the control group fed ad libitum (Figure 3b). These outcomes are in total agreement with Azis and Afriani (2023), who documented a reduction in the weights of the spleen and Fabricius bursa in feed-restricted broiler chick groups. The lymphoid organs (bursa of Fabricius, spleen, and thymus) are considered vital organs for producing B and T lymphocytes. These lymphoid organs weighed less due to feed restriction than in the control group (Rahimi et al., 2015).

The mean weight value of the thymus gland in Group A (feed restricted for 6 hours), B (feed restricted for 12 hours), C (feed restricted for 24 hours), and D (feed offered ad libitum) is 4.68 ± 0.34, 2.75 ± 0.25, 2.04 ± 0.09, and 6.78 ± 0.28, respectively. All feed-restricted groups showed significantly lower thymus weights than the control group D fed ad libitum (Figure 3b) (Ahmadibonakdar et al., 2024).

3.7 Machine Learning Modeling

XGBoost and Gradient Boosting yielded the best results among all models tested, followed closely by Ridge Regression. XGBoost was able to achieve an R^2 of 0.9412, an RMSE of 55.40 g, and an MAE of 42.10 g. Therefore, it appears that tree-based ensembles and Ridge regression were able to successfully reduce multicollinearity in the data but retain all of the original predictors. Ridge regression has shown itself to be very robust when used on a properly preprocessed and augmented version of the full dataset (Arkorful, 2023; Mubasher et al., 2024).

Gradient boosting, random forest, AdaBoost, and XGBoost have been demonstrated to be extremely effective at predicting physiological responses to feed restriction. All four of these algorithms were found to produce R^2 values greater than .9 with biologically meaningful error rates. All four of these algorithms are well known for being capable of modeling a wide variety of nonlinear relationships between features. Because of the large amount of data augmentation, the algorithms were able to learn a great deal about the relationships between the predictors and the response variable. And because the data were kept separate during training and testing, there was no opportunity for data leakage. Compared to ridge regression and the four tree-based ensemble models, linear regression had a significantly lower R^2 value (.8215). Although this may indicate that linear

Table 3. Performance metrics of machine learning models for body weight prediction.

Algorithm	R^2	MAE (g)	RMSE (g)	MAPE	Explained Variance	Accuracy (±10%)
Linear Regression	0.8215	85.60	108.40	0.0520	0.8220	0.84
Ridge Regression	0.9241	48.30	62.50	0.0310	0.9245	0.94
Lasso Regression	0.7850	95.20	119.50	0.0610	0.7865	0.81
Decision Tree	0.8520	72.40	95.30	0.0480	0.8525	0.87
Random Forest	0.9305	45.60	59.20	0.0290	0.9310	0.95
Gradient Boosting	0.9388	43.50	56.80	0.0280	0.9390	0.95
AdaBoost	0.9150	51.20	65.70	0.0330	0.9155	0.92
XGBoost	0.9412	42.10	55.40	0.0270	0.9415	0.96
Deep Neural Network	0.4520	185.40	245.60	0.1250	0.4600	0.55

Regression can pick up on certain basic patterns within the data; the much higher error rates associated with linear regression demonstrate that this type of

model will fail miserably when attempting to predict complex nonlinear biological relationships (Abbas et al., 2024; Ahmad et al., 2022).

Lasso regression performed poorly compared to the other three models tested. An R^2 of .7850 was calculated for lasso regression. This represents poor generalizability. It is generally accepted that lasso performs poorly when there are multiple collinear or redundant features in a dataset. Additionally, if there are too many samples available and/or if there are too many important features facing penalties, then lasso will likely remove important features (Ma et al., 2022; Schmidiger, 2017).

Deep neural networks have performed the worst among all of the models tested. Deep neural networks have generated an R^2 of .4520, an MAE of 185.40 g, and an RMSE of 245.60 g. The lower quality results from using deep neural networks are attributed to both overfitting and a lack of sufficient training data. Overfitting occurs when the model is trained too long or on too little data. Both issues are common problems when using deep learning models on small datasets. This illustrates the importance of choosing models that are appropriately sized and suited for use on datasets that contain limited amounts of information (Goodfellow et al., 2016; Guo et al., 2022).

Table 3 shows the performance results for all the machine learning models tested. Table 3 demonstrates that different levels of accuracy exist across the models tested, and that some models have provided exceptional results when they were applied to the properly separated dataset.

XGBoost has demonstrated exceptional performance, producing an R^2 of .9412 and having very low error rates (MAE: 42.10 g, RMSE: 55.40 g, and MAPE: 0.0270) that reflect excellent predictive capabilities (Mustafa et al., 2025). Likewise, gradient boosting,

random forest, adaboost, and ridge regression also performed exceptionally well, each obtaining R^2 values > .91 and small error metrics that indicated very good predictive abilities on unknown data. A moderate level of acceptable performance was obtained by linear regression (R^2 = .8215). However, lasso regression was found to be less successful than the other three models tested; an R^2 of .7850 was reported. This suggests that lasso regression did not generalize well due to extreme regularization. As expected, the deep neural network yielded poor results; an extremely low R^2 (.4520) and notably high MAE (185.40 g) and RMSE (245.60 g) values indicate overfitting and inefficient training in relation to the small dataset (Table 3).

The strong performance of most models (especially XGBoost, Gradient Boosting, AdaBoost and Ridge Regression) implies that the augmented data sufficiently captured the critical relationships between feed restriction and physiological traits that affect body weight prediction. On the contrary, DNNs' poor performance clearly demonstrates the difficulties involved in using deep neural networks with small datasets despite using data augmentation. The results presented here illustrate that ensemble methods like Gradient Boosting and XGBoost would be ideal candidates for this biological prediction task.

4. Conclusion

Feed restriction, as a stress factor, adversely affected both cellular and humoral immune responses to Newcastle disease virus. Most hematological parameters decreased in the stressed groups compared with the unstressed group. Antibody titers were lowered in all experimental groups, making chicks susceptible to Newcastle disease virus. Ensemble models such as Gradient Boosting and XGBoost achieved high accuracy in predicting body weight under these stress conditions (R^2 > 0.93), with Ridge Regression also demonstrating strong predictive capability (R^2 = 0.9241). In contrast, the Deep Neural Network and Lasso Regression performed poorly, highlighting the limitations of complex or overly regularized models on small, augmented datasets. Furthermore, the lymphoid organs showed less growth in all experimental groups than in the control group. A high mortality rate was observed in stressed groups. Similarly, feed conversion efficiency was disrupted during the restriction and challenge phases. Ultimately, severe mid-growth feed restriction severely stunted broiler body weight and compromised immunity, effects that can be reliably forecasted using properly validated ensemble machine learning models.

Financial Support Statement

This study was supported by the Basic Research Laboratory (No. RS-2023-00219983) through the National Research Foundation (NRF) of the Ministry of Education, Science, and Technology (MEST) of the South Korean government.

References

Abbas, F., Cai, Z., Shoaib, M., Iqbal, J., Ismail, M., Ullah, A., Alrefaei, A. F., & Albeshr, M. F. (2024). Ensemble machine learning algorithms for prediction and classification of animal body weight from non-intrusive parameters. Scientific Reports, 14(1), 5478.

Abdi, R. D., Amsalu, K., Merera, O., Asfaw, Y., Gelaye, E., Yami, M., & Sori, T. (2016). Serological survey of Newcastle disease virus antibodies in village chickens (Gallus gallus domesticus) in Ethiopia. Poultry Science Journal, 4(1), 29-36.

Abou-Elnaga, M., & Selim, S. (2018). Influence of early feeding with different diet composition on performance and immune response of broiler chicks.

Journal of Animal & Poultry Production, 9(3), 119-126.

Ahmad, M., Al-Mansob, R. A., Kashyzadeh, K. R., Keawsawasvong, S., Sabri, M. M. S., Jamil, I., & Algannam, M. M. (2022). Prediction of California bearing ratio of construction waste containing soils using multi-expression programming. Journal of Marine Science and Engineering, 10(11), 1697.

Ahmadibonakdar, Y., Vakili, A., Javadmanesh, A., & Rajaei-Sharifabadi, H. (2024). Effect of thymol on thymic development and gene expression in broilers under heat stress. Poultry Science, 103(3), 103406.

Ahsan, M. M., Mahmud, M. P., Saha, P. K., Gupta, K. D., & Siddique, Z. (2021). Effect of data scaling methods on machine learning algorithms and model performance. Technologies, 9(3), 52.

Al-Abdullatif, A. A., Azzam, M. M., Samara, E. M., Al-Badwi, M. A., Dong, X., & Abdel-Moneim, A.-M. (2024). Immunological response of laying hens fed diets containing lauric acid-enriched fat under high ambient temperature. Poultry Science, 103(1), 103131.

Anh, D. T., Thanh, D. V., Le, H. M., Sy, B. T., Tanim, A. H., Pham, Q. B., Dang, T. D., Mai, S. T., Bui, D. T., & Petpongpan, C. (2023). Evaluating the effectiveness of machine learning methods in predicting COVID-19 mortality: a systematic review and meta-analysis. Geomatics, Natural Hazards and Risk, 14(1), 2199615.

Arkorful, B. (2023). Regularized and robust regression methods of linear model with multicollinear predictors. American Journal of Theoretical and Applied Statistics, 12(5), 126-137.

Azis, A., & Afriani, A. (2023). The effects of feeding time restriction on carcass yield characteristics and lymphoid organs in broiler. Chalaza Journal of Animal Husbandry, 8(2), 73-79.

Bansal, M., Goyal, A., & Choudhary, A. (2022). A comparative analysis of K-nearest neighbor, genetic, support vector machine, decision tree, and long short-term memory algorithms in machine learning. Decision Analytics Journal, 3, 100071.

Bhadauria, P., & Bhanja, S. (2017). Collection, analysis and interpretation of welfare-related data. Collection, Analysis and Interpretation of Welfare Related Data in Poultry, 47.

Bortoluzzi, C., Fernandes, J. I. M., Contini, J. P., Gurski, T. J., Esser, A. F. G., & Prokoski, K. (2013). Effect of qualitative and quantitative feed restriction in the starter period over the performance and carcass characteristics of broilers. Revista Brasileira de Ciência Avícola, 15, 213-220.

Dosu, G., Obanla, T. O., Zhang, S., Sang, S., Adetunji, A. O., Fahrenholz, A. C., Ferket, P. R., Nagle, T. A., & Oviedo-Rondón, E. O. (2023). Effects of short-term feed withdrawal on the intestinal microbiome and the performance of broiler chickens. Poultry Science, 102(10), 102931.

Evaluation of different changes in diurnal feed restriction for broilers. (2021). Research, Society and Development, 10(16), e339101623677.

Farghly, M. F., Mahrose, K. M., Ahmad, E. A., Rehman, Z. U., & Yu, S. (2019). Implementation of different lighting programs in bobwhite quail management. Poultry Science, 98(9), 3843-3849.

Gaweł, A., Madej, J. P., Kozak, B., & Bobrek, K. (2022). Early post-hatch nutrition influences performance and development of immune organs and gut morphology of broiler chickens. Animals, 12(23), 3360.

Gholami, M., Chamani, M., Seidavi, A., Sadeghi, A. A., & Aminafschar, M. (2020). Effects of stocking density and feeding program on the immunity, blood biochemistry, and antioxidant status of broiler chickens. Arquivo Brasileiro de Medicina Veterinária e Zootecnia, 72, 983-992.

Ghosh, P., Azam, S., Jonkman, M., Karim, A., Shamrat, F. J. M., Ignatious, E., Shultana, S., Beeravolu, A. R., & De Boer, F. (2021). Efficient prediction of cardiovascular disease using machine learning algorithms with relief and LASSO feature selection techniques. IEEE Access, 9, 19304-19326.

Goodfellow, I., Bengio, Y., Courville, A., & Bengio, Y. (2016). Deep learning (Vol. 1). MIT Press, Cambridge.

Guo, X., Mo, Y., & Yan, K. (2022). Short-term photovoltaic power forecasting based on historical information and deep learning methods. Mathematical Problems in Engineering, 2022(1), 6083963.

Hollemans, M., De Vries, S., Lammers, A., & Clouard, C. (2018). Effects of early nutrition and transportation duration on chicken welfare and performance. Poultry Science, 97(1), 112-122.

Islam, R., Sultana, N., Haque, Z., & Rafiqul Islam, M. (2023). Effect of dietary dexamethasone on the lymphoid organs of broiler chickens. Veterinary and Animal Science, 22, 100318.

Jacobs, L., Delezie, E., Duchateau, L., Goethals, K., Ampe, B., Lambrecht, E., Gellynck, X., & Tuyttens, F. A. (2016). Impact of the feed withdrawal period and the lairage duration on broiler chicken welfare and meat quality. Poultry Science, 95(6), 1301-1308.

Jang, I., Kang, S., Ko, Y., Moon, Y., & Sohn, S. (2009). Effect of qualitative and quantitative feed restriction of broiler breeder hens during the rearing period on their immune response. Asian-Australasian Journal of Animal Sciences, 22(3), 385-391.

Jawad, H. (2023). The effect of early feeding and transporting time from hatcher to farm on the production performance of broilers. Iraqi Journal of Agricultural Sciences, 54(2), 393-402.

Kalia, S., Bharti, V. K., Giri, A., & Kumar, B. (2017). Effect of hydro-alcoholic extract of Rhodiola imbricata on broiler chicks raised at high altitude. Veterinary World, 10(7), 781.

Kang, H., Bang, H. T., Kim, C. H., Jeon, J. J., Kim, H. S., Suh, S. W., Hong, E. C., Kim, S. H., & Park, S. B. (2018). Effects of different holding times after hatch on growth performance, intestinal development, and blood biochemical parameters of broiler chicks. Animals, 8(10), 174.

Kouki, C., Bergaoui, R., Ouerghi, F., Rhouma, A., Aloui, S., Rassaa, N., Hennachi, I., & Nasraoui, B. (2016). Effect of a quantitative feed restriction applied at different ages on productive and reproductive performances of broiler breeders. Agriculture, 6(3), 37.

Kuhle, S., Maguire, B., Zhang, H., Hamilton, D., Allen, A. C., Joseph, K., & Allen, V. M. (2018). A comparison of logistic regression, classification tree analysis, and random forests to identify effective interventions in a vaccine study with binary outcomes. PLoS One, 13(8), e0203598.

Liu, K., Jia, M., & Wong, E. A. (2020). Delayed access to feed affects broiler small intestinal morphology and muscle development at hatch. Poultry Science, 99(12), 6640-6647.

Lu, S., Taethaisong, N., Meethip, W., Surakhunthod, J., Sinpru, B., Sroichak, T., Archa, P., Thongpea, S., Paengkoum, S., Moonmanee, T., & Paengkoum, P. (2022). Effects of black soldier fly larvae (Hermetia illucens L.) meal on growth performance, carcass characteristics, and small intestinal morphology of broilers. Frontiers in Veterinary Science, 9, 890158.

Ma, X., Chen, T., Ge, R., Cui, C., Xu, F., & Lv, Q. (2022). Time series-based PM2. 5 concentration prediction and its uncertainty quantification using a simple deep learning approach. Urban Climate, 44, 101186.

Madej, J. P., Graczyk, S., Bobrek, K., Bajzert, J., & Gaweł, A. (2024). Impact

of early posthatch feeding on the development of lymphoid organs, intestinal structure, performance, and immunity of meat-type chickens. Animals, 14(2), 299.

Mohammadalipour, R., Rahmani, H., Jahanian, R., Riasi, A., Mohammadalipour, M., & Nili, N. (2017). Effect of early feed restriction on physiological responses, performance and ascites incidence in broiler chickens raised under high altitude. Animal, 11(2), 219-226.

Mohammadalipour, R., Rahmani, H. R., Jahanian, R., Riasi, A., Mohammadalipour, M., & Nili, N. (2017). Effect of early feed restriction on physiological responses, performance and ascites incidence in broiler chickens raised under high altitude. Animal, 11(2), 219-226.

Mubasher, S., Zakria, M., Shahzad, A., & Ali, N. (2024). Dynamic Ridge Regression vs. Lasso Regression for predictive modeling in supervised learning: a comparative study. Pakistan Journal of Statistics, 40(3).

Mustafa, G., Younas, A., Zahid, M. T., Kim, D.-W., Jamil, I., Yadav, N., Kurade, M. B., Saha, S., Yang, W., & Jeon, B.-H. (2025). From farm to forecast: machine learning in broiler production optimization under varying feed restriction regimes. Poultry Science, 106281.

Ogbu, O. (2020). Premix Graded Level in Broiler Starter Diet and Their Effect on Broiler Performance and Blood Profile. Nigerian Journal of Animal Science, 22(1), 18-27.

Orso, C., Moraes, M. L., Aristimunha, P. C., Della, M. P., Butzen, M. F., Krás, R. V., Ledur, V. S., Costa, P. T., Coldebella, A., & Galli, G. M. (2019). Feed restriction in broiler breeders: effects on production performance, egg quality and hatchability. Poultry Science, 98(12), 6497-6506.

Oviedo-Rondon, E. O., Leandro, N., Ali, R., Koci, M., Moraes, V., & Brake, J. (2013). Broiler breeder and layer production under high ambient temperatures: a review. The Journal of Applied Poultry Research, 22(4), 921-934.

Pal, S. K., & Dutta, D. (2024). Transfer Learning in Weather Prediction: Why, How, and What Should We Transfer? Authorea Preprints.

Panda, A., Bhanja, S., & Sunder, G. S. (2015). Early post-hatch nutrition on immune system development and function in poultry. World's Poultry Science Journal, 71(3), 487-500.

Pirompud, P., Sivapirunthep, P., Punyapornwithaya, V., & Chaosap, C. (2024). Machine learning predictions of poultry carcass composition and ham quality traits in crossbred chickens. Journal of Animal Science, 102, skae107.

Rahimi, S., Seidavi, A., Sahraei, M., Blanco, F. P., Schiavone, A., & Martínez Marín, A. L. (2015). Effects of feed restriction and diet nutrient density during and after restriction on the performance, carcass traits, organ weights, blood parameters and caecal microflora of broilers. Italian Journal of Animal Science, 14(2), 3734.

Razali, M. N., Arbaiy, N., Lin, P.-C., & Ismail, S. (2025). Optimizing Multiclass Classification Using a Combined One-vs-Rest SVM and Genetic Algorithm for Credit Risk Prediction. IEEE Access.

Saber, S. N., Maheri-Sis, N., Shaddel-Telli, A., Hatefinezhad, K., Gorbani, A., & Yousefi, J. (2011). Effect of feed restriction on growth performance of broiler chickens. Annals of Biological Research, 2(6), 247-252.

Sağlam, F., & Cengiz, M. A. (2022). A novel SMOTE-based resampling technique through noise detection and the boosting procedure. Expert Systems with Applications, 200, 117023.

Sahraei, M. (2014). Effects of feed restriction on metabolic disorders in broiler chickens: a review. European

Online Journal of Natural and Social Sciences, 3(4), 912.

Schmidiger, C. (2017). All Style Hedge Fund Analysis with Constant-and Time-Varying Factor Loading Models (Doctoral dissertation, University of Zurich).

Selim, S., Abdel-Megeid, N. S., Abou-Elnaga, M. K., & Mahmoud, S. F. (2021). Early nutrition with different dietary levels of energy and protein affects performance and immune response of broilers. Tropical Animal Health and Production, 53, 1-10.

Shinde Tamboli, A., Goel, A., Mehra, M., Rokade, J., Bhadauria, P., Yadav, A., Majumdar, S., & Bhanja, S. (2018). Early posthatch feeding of chicks: an update. World's Poultry Science Journal, 74(1), 137-151.

Singh, P., Borgohain, S. K., Sarkar, A. K., Kumar, J., & Sharma, L. D. (2023). Feed-Forward Deep Neural Network (FFDNN) and Hybrid Deep Learning Methods for Classification-Based Kidney Disorder Prediction. Bioengineering, 10(9), 1097.

Thiam, M., Wang, Q., Barreto Sánchez, A. L., Zhang, J., Ding, J., Wang, H., Zhang, Q., Zhang, N., Wang, H., & Jiang, S. (2022). The hematological responses of broilers to heat stress, immunity, and thermal manipulation: A review. Journal of Thermal Biology, 108, 103305.

Wang, J. S., Hu, H. J., Xu, Y. B., Wang, D. C., Jiang, L., Li, K. X., Wang, Y. Y., & Zhan, X. A. (2020). Fatty acid composition and lipid metabolism-related gene expression in broilers with different 18C polyunsaturated to saturated fatty acid ratios in diets. Poultry Science, 99(12), 6636-6644.

Wijnen, H. J., van der Pol, C. W., van Roovert-Reijrink, I. A., De Smet, J., Lammers, A., Kemp, B., & van den Brand, H. (2021). Effects of delayed feed access on post-hatch metabolic and gastrointestinal tract development in broiler chicks. Poultry Science, 100(12), 101491.

Yadav, M., Rastogi, S. K., Huozha, R., Patel, M., Kumar, S., Verma, M., Maiti, A., Das, A. K., & Gangwar, S. (2021). Immunomodulatory potential of different dietary plant extracts in broilers. Veterinary World, 14(11), 2895.

UCP Journal of Science and Technology
Vol. 3, Issue 2 (January - June 2026)
Journal website: http://ojs.ucp.edu.pk/index.php/ucpjst/index

Formulation and Characterization of Nanoemulsion Containing Terbinafine HCl against Candida albicans Fungal Infections

Ayesha Rauf[1], Aqsa Maimoona Malik[*2], Nadeem Reyaz[*3], Ling Shing Wong[2,4], Jureerat Kijsomporn[4], Tooba Malik[5]

Abstract

Background: Transdermal drug delivery of antifungal drugs has always remained very challenging due to poor penetration and retainability of the formulation at the site of infection. Objective: The main objective was to enhance the permeation and bioavailability of Terbinafine HCl-loaded nanoemulsion for better penetration potential and efficacy in treating superficial infections. Method: A Terbinafine HCl-loaded nanoemulsion was formulated using the high-speed homogenization technique and subsequently evaluated through UV spectrophotometric analysis for drug solubility, FTIR spectroscopy for drug compatibility and content confirmation, and HPLC analysis for characterization of the optimized formulation. Furthermore, formulation variables were optimized using Design-Expert software by applying a Central Composite Rotatable Design (CCRD). The zeta sizer measured the particle size, and the heterogeneity index was assessed, while the Malvern Zetasizer was used for the zeta potential assessment. Droplet size was assessed via SEM, and in vitro penetration was studied via the Franz diffusion cell. For in vivo and histopathological examination, albino rabbits were used. Results: The formulation prepared was subjected to various characterization parameters. The average drug content was found to be 98.57%, and the average particle size of the optimized formulation was 57.81 nm with good homogeneity as indicated by a low Heterogeneity index, i.e., 0.08. In vivo and microbiological studies showed that the Terbinafine HCl nanoemulsion significantly reduced the Candida albicans infection in animals; moreover, the microbiological assessment also showed decreased growth of Candida albicans. Conclusion: The present study presents a novel nanoemulsion of Terbinafine HCl, which could be further explored in human subjects for a better understanding of its efficacy and the toxicity effects on human health.

Keywords: Terbinafine HCl-loaded Nanoemulsion, Skin Yeast Infections, Candida Albicans, Heterogeneity.

1. Introduction

The skin, the largest and outermost organ of the human body, functions as a highly specialized protective interface that safeguards underlying tissues from external insults including mechanical trauma, microbial invasion, ultraviolet

[1] VetCure Pharma, Plot 191, 4th Street, Cavalry Ground, Lahore.
[2] Faculty of Health and Life Sciences, INTI International University, Putra Nilai, Negeri Sembilan, Malaysia.
[3] Department of Pathology, Al-Aleem Medical College, Lahore, Pakistan.
[4] School of Nursing, Shinawatra University, Samkhok, Pathum Thani, Thailand.
[5] Services Institute of Medical Sciences, Lahore, Pakistan.
*Corresponding author's E-mail: drnadeemreyaz@yahoo.com; aqmm.rph@gmail.com
Received: 25 October 2025; Received in revised form: 04 May 2026; Accepted: 30 May 2026.
Available online: 13 July 2026.

DOI: https://doi.org/10.24312/ucp-jst.03.02.716

(UV) radiation, and various environmental stressors. Structurally, the skin is composed of three distinct layers: the epidermis, dermis, and hypodermis. Among these, the stratum corneum, the outermost region of the epidermis, constitutes the principal barrier to percutaneous drug permeation. This layer comprises densely packed, keratinized corneocytes embedded within an organized extracellular lipid matrix referred to as lipid lamellae, which collectively restrict the penetration of exogenous substances (Iman, Nadia, & Ebtsam, 2010; Nastiti et al., 2017; Nikam et al., 2018). Transdermal permeation of therapeutic agents occurs predominantly through three pathways: intercellular diffusion across the lipid domains, intracellular (transcellular) transport through corneocytes, and appendageal transport via hair follicles and sweat glands. Advanced drug delivery strategies have been extensively explored, among which transdermal drug delivery systems have emerged as a promising alternative owing to their ability to enhance therapeutic efficacy, improve bioavailability, provide sustained drug release, and facilitate patient compliance while circumventing first-pass hepatic metabolism (Ng, Lau, & effects, 2015; Barakat, Fouad, & Elmedany, 2011) (Figure 1).

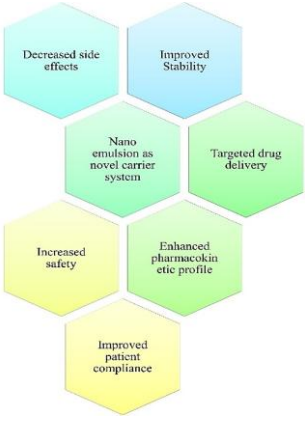

Figure 1. Nanoemulsion as a novel drug carrier

Nanoemulsions are advanced colloidal drug delivery systems composed of two immiscible phases, oil and water, stabilized by optimized concentrations of surfactants and co-surfactants, with droplet sizes typically ranging between 20 and 200 nm. Owing to their enhanced drug solubilization capacity, superior thermodynamic stability, ease of large-scale manufacturing, and remarkable kinetic stability, nanoemulsions have emerged as highly promising carriers for controlled and targeted drug delivery applications. Compared with conventional emulsions, nanoemulsions exhibit several advantageous properties, including improved drug encapsulation efficiency, enhanced dispersibility, greater physicochemical stability, absence of flocculation, prolonged drug release, and increased transdermal permeation (Abolmaali et al., 2011; Shah, Bhalodia, & Shelat, 2010; Suyal & Bhatt, 2017). Terbinafine hydrochloride (TBH), a synthetic allylamine derivative, is a broad-spectrum antifungal agent extensively utilized in the treatment of superficial fungal infections such as tinea corporis, tinea pedis, and tinea cruris. Its antifungal activity is primarily attributed to the selective inhibition of squalene epoxidase, disrupting fungal cell membrane integrity. Despite its potent antifungal efficacy, TBH exhibits poor aqueous solubility, which limits its therapeutic performance. Moreover, oral administration of TBH is associated with approximately 40% drug loss due to extensive first-pass hepatic metabolism, in addition to dose-related systemic adverse effects. Incorporation of TBH into nanoemulsion systems offers a promising strategy to overcome these limitations by enhancing drug solubility, improving physicochemical stability, and promoting efficient transdermal permeation (Elmataeeshy, Sokar, Bahey-El-Din, & Shaker, 2018) (Figure 2).

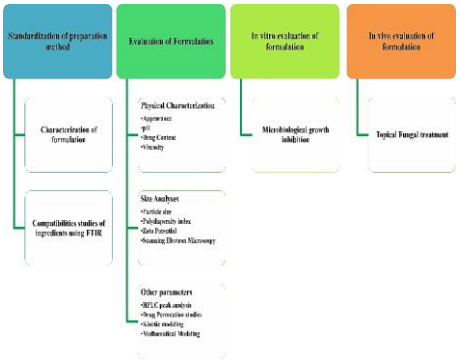

Figure 2. Method of preparation and characterization parameters of Terbinafine HCl nanoemulsion

In the early phase of formulation development, compatibility study of both active ingredient and excipients is essential. Excipients are primarily used to facilitate the administration of a drug substance and enhance the stability of the formulation. They can also improve the drug's taste or appearance and aid in controlling the release or absorption of the active ingredient. In the oil phase, the drug was dissolved using a vortex mixer, then in a separate beaker surfactant was added to water and was homogenized; afterwards, the oily mixture was added to the water phase slowly and mixed at the speed of 15,000 rpm initially, then gradually raised to 20,000 rpm to make Terbinafine HCl nanoemulsion.

2. Materials and Methods

Active drug Terbinafine HCl (Willshire Laboratories, Pakistan), Eucalyptus oil (Flavchem royal, China), Tween 80 (SIGMA-ALDRICH, Germany), Ethanol (Merck KGaA Darmstadt, Germany), and distilled water. Analytical grade chemicals were used for the study.

2.1 Physicochemical Characterization

2.1.1 Suitable Oil Selection

To determine the solubility of Terbinafine HCl in different oils, an excess amount of the drug was introduced into 10 mL of each selected oil, then the mixtures were thoroughly agitated using a vortex mixer and subsequently maintained in an isothermal shaker at 25 ± 1 °C until equilibrium was attained.

2.1.2 Selection of Surfactant

The choice of a suitable surfactant is a key factor in the development of nanoemulsion systems and is largely determined by the hydrophilic-lipophilic balance (HLB) value. In the case of oil-in-water nanoemulsions, surfactants with higher HLB values and pronounced hydrophilic properties are generally preferred. Accordingly, based on an HLB requirement of 15, the non-ionic surfactant Tween 80 was selected for formulation development (Azeem et al., 2009).

2.2 Solubility

The solubility of Terbinafine HCl in water (3 mg/mL) is relatively low compared to organic solvents. In contrast, its estimated solubility in ethanol is 45 mg/mL. Therefore, ethanol is used as a suitable solvent (Shi & Xie, 2017).

2.3 Compatibility Studies

In the initial phase of formulation development, evaluating the compatibility between the active pharmaceutical ingredient and selected excipients is crucial. Although excipients are incorporated to facilitate drug delivery and improve the stability of the formulation, they can sometimes interact with the drug substance, leading to instability, chemical degradation, or altered therapeutic performance. Hence, achieving a safe, effective, and stable formulation depends on the judicious selection of appropriate excipients, which is confirmed through comprehensive compatibility studies (Rojek & Wesolowski, 2019).

2.4 Fourier Transform Infrared (FTIR) Spectroscopy

A non-destructive technique of analysis, namely FTIR spectroscopy, is used to identify the specific chemical characteristics of a substance. It is commonly applied to analyze drugs either alone or in combination with excipients.

Each liquid or powdered sample is placed on the sample port for detection. Liquid material can be analyzed simply by placing it on the sample port, while for powdered material, the material on the sample port is pressed with the tip of the analyzer, characterizing it against an FTIR library, producing a spectrum of the sample (Franca & Oliveira, 2011).

2.5 UV Spectrophotometric Analysis

A standard stock solution of Terbinafine HCl was prepared by accurately dissolving 10 mg of the drug in 10 mL of ethanol, yielding a primary concentration of 1 mg/mL. An aliquot of 1 mL from this solution was diluted to 10 mL with phosphate buffer (pH 6.8), producing a working solution of 0.1 mg/mL (100 µg/mL). Subsequently, 1 mL of this working solution was diluted up to 10 mL using the same phosphate buffer, resulting in a final diluted stock concentration of 0.01 mg/mL (10 µg/mL).

2.6 Calibration Curve

From the stock solution, 2, 4, 6, 8, and 10 mL aliquots were accurately measured into separate test tubes and individually diluted to a final volume of 10 mL with phosphate buffer (pH 6.8), resulting in solutions with concentrations of 2, 4, 6, 8, and 10 µg/mL, respectively. The absorbance of each prepared dilution was recorded at 283 nm, then a calibration curve was constructed by plotting absorbance against concentration, and the slope, intercept, and correlation coefficient (r^2) were obtained through linear regression analysis.

2.7 HPLC Analysis

High-performance liquid chromatography (HPLC) was applied for both identification and quantification of the analyte. The standard and test samples were prepared at an equal concentration of 2 mg/mL, and 10 µL of each solution was injected into the chromatographic system for analysis. Detection was performed at 225 nm. The mobile phase consisted of acetonitrile, methanol, and phosphate buffer in the proportion of 40:30:30 (v/v/v), with the buffer pH adjusted to 3.5 using orthophosphoric acid. Before use, the mobile phase was passed through a 0.45 µm membrane filter and degassed to ensure system suitability, then separation was carried out on a 25 cm L1 column with an internal diameter of 4.5 mm, operating at a flow rate of 1.0 mL/min, while UV detection was maintained at 225 nm. Retention time is used for identification, while the area of the peak is used for quantitative analysis. Assay values or the percentage quantity of the sample can be determined by:

$$\% \, age = Ru/Rs \times Wst/Dst \times Ds/Ws \times potency$$

Where, Ru = Average area of standard, Rs = Average area of sample, Wst = weight of standard, Dst = density of standard, Ds = density of sample, and Ws = weight of sample.

2.8 Method of Formulating TBH Nanoemulsion

To design and optimize the formulation of nanoemulsion containing Terbinafine HCl, Design Expert software using Central Composite Rotatable Design (CCRD) was used. By varying the composition of oil and surfactant, trial formulations were designed. Nanoemulsions using various compositions were prepared using high-speed homogenization. For the optimized formulation, eucalyptus oil, ethanol, and drug (Terbinafine HCl) were added to a glass test tube and placed on a vortex mixer (VELP Scientifica, Italy) for 2–4 min in order to dissolve the drug. In a separate vessel, Tween 80 was dissolved in distilled water to constitute the aqueous phase, followed by homogenization using a high-speed homogenizer (Heidolph Silent Crusher M, Germany). The oil phase was then incorporated slowly in a dropwise manner into the continuously agitated aqueous phase. Homogenization

was initiated at 5,000 rpm and progressively increased to 20,000 rpm, continuing for ten to fifteen minutes to ensure uniform emulsification. The resulting nanoemulsion was subsequently subjected to a range of physical and chemical characterization studies (Karri et al., 2015).

3. Experimental

3.1 Characterization of TBH Nanoemulsion

3.1.1 Appearance

Nanoemulsions containing very fine droplets are transparent and more homogeneous. Turbidity may increase with the increase in droplet concentration.

3.1.2 Particle Size Analysis

Nanoemulsion containing Terbinafine HCl was prepared and analyzed for droplet size using a ZetaSizer (Malvern ZS90). Size was determined at 25°C after mixing 0.1 mL of the formulation in 10 mL of distilled water (Elsheikh, Elnaggar, Gohar, & Abdallah, 2012).

3.1.3 Polydispersity Index

The polydispersity index (PDI) of the prepared optimized formulation indicates a homogeneous system. PDI (size distribution) was established by Zetasizer (Malvern, ZEN90), dispersing 1 mL of the formulation in 100 mL of distilled water. Results should lie within the desired range of PDI; ideally, PDI should be less than 0.7.

3.1.4 Zeta Potential

Zeta potential is a key physicochemical parameter used in nanoparticle characterization because it reflects the electrical charge present at the particle surface and serves as an indicator of colloidal stability. In this study, it was determined using a Malvern Zetasizer ZEN3600. Higher absolute zeta potential values indicate greater electrostatic repulsion between particles and, thus, improved formulation stability.

3.1.5 Scanning Electron Microscopy

Scanning electron microscopy (SEM) is a powerful analytical technique used for ultrastructural evaluation because it provides high-resolution, three-dimensional visualization of the surface morphology of both dry and hydrated samples. In this study, SEM (JSM5600LV, JEOL, Japan) was utilized to confirm the nano-sized droplets of the formulation.

3.1.6 pH Measurement

In the literature, variable skin pH values are recorded, all in the slightly acidic range of 4.5–6.5. pH values within this range are considered safe to be applied topically; thus, the formulation pH was then determined (Schott Gerate, CG-820, Germany).

3.1.7 Viscosity

The viscosity of the nanoemulsion formulation was assessed during the consistency study using a Brookfield viscometer maintained at 25 °C, with measurements taken using spindle 1 and spindle 2 at speeds of 30 rpm and 60 rpm, respectively (Qian, Cui, Wang, Wang, & Zhou, 2011).

3.1.8 Drug Content

The amount of drug present in each formulation was determined by UV-visible spectrophotometry through measurement of absorbance at 283 nm, followed by calculation of the concentration using the standard formula:

$$\% \text{ Drug content} = \frac{\text{Absorbance of sample}}{\text{Absorbance of standard}} \times 100$$

3.2 Drug Permeation Studies

The permeation behavior of the formulation was evaluated using a Franz diffusion cell to determine its drug permeation rate. A cellulose acetate artificial membrane with an approximate pore size of 0.45 µm (Millipore) was used as the diffusion barrier, following established in vitro permeation protocols. The study involved recording and plotting the cumulative amount of terbinafine hydrochloride that permeated through the

membrane over time to compare the release profiles of different nanoemulsion formulations. The optimized nanoemulsion was anticipated to release more than 60% of the drug within the initial 5 hours; furthermore, cumulative drug permeation was calculated for the optimized formulation and expressed as a function of time.

3.3 Kinetic Modelling of Permeation Data

Mathematical modelling contributes to the determination of drug release during formulation development. Nanoemulsions are liquid topical preparations, and within the first 5 hours, 60% of the drug must permeate through the membrane.

3.4 In Vivo Studies of Prepared Formulation

The formulated product in vivo assessment was conducted in accordance with established national ethical and regulatory guidelines for the care and use of laboratory animals, after obtaining ethical approval for the study from the Ethical Committee of the Faculty of Health and Life Sciences, Al Aleem Medical College. Albino rabbits (800–950 g) were randomly assigned to three groups and housed under standard laboratory conditions, including a light/dark cycle of 12 hr, with a temperature controlled at 25 ± 2 °C.

3.4.1 Test Organism and Preparation of Fungal Inoculums

Candida albicans culture was obtained from the Department of Pathology, Al Aleem Medical College. The parent strain was subsequently subcultured in 3% Sabouraud dextrose broth and incubated at 28 °C for three to five days to ensure ideal growth and viability prior to its use in the experiment.

3.4.2 Induction of Cutaneous Candida Infection

All animals were rendered immunosuppressed via intraperitoneal injections of cyclophosphamide at a dose of 33.5 mg/kg body weight, administered in three separate doses on days 5, 3, and 1 before infection induction. The hair on a 4 cm^2 area of the rabbit skin was carefully shaved, after which the site was disinfected using ethyl alcohol. A cotton swab impregnated with 0.1 mL of fungal suspension was then placed onto the prepared skin surface, covered with adhesive tape, and left in place for 3 days to facilitate infection establishment. The successful induction of fungal infection was verified by the development of erythema and visible inflammation at the application site. Animals were allocated into three groups: Group I acted as the untreated control, Group II received a commercially available antifungal cream as the standard reference treatment, and Group III was administered the TBH nanoemulsion formulation. All treatments were applied topically once daily at an equivalent dose of 2 mg of drug per day for five consecutive days (AbdelSamie, Kamel, Sammour, & Ibrahim, 2016).

3.4.3 Ethical Considerations in the Use of Laboratory Animals

All the animal studies were conducted at Al Aleem Medical College. The ethics committee of the institute approved the animal experiment design (MPCH23422).

3.5 Statistics

Data were expressed as mean ± standard error of the mean. Differences between two groups were analyzed using a two-tailed Student's t-test, whereas comparisons among three or more groups were assessed using two-way analysis of variance (ANOVA) followed by Bonferroni's post hoc test. Statistical significance was defined as a p-value <0.05.

4. Results

4.1 Compatibility Study using Fourier Transformed Infrared Spectroscopy (FTIR)

4.1.1 FTIR Spectrum of Terbinafine Hydrochloride

The major peaks of pure Terbinafine hydrochloride present in Figure 3A were well supported by functional groups present in the spectrum available in the literature.

4.1.2 FTIR Spectrum of Eucalyptus Oil

In 2014, Sudhakar and co-workers analyzed the FTIR spectrum of eucalyptus oil to evaluate its purity and reported characteristic peaks similar to those presented in Figure 3B. Likewise, Pant et al. (2014) investigated the FTIR spectrum of eucalyptus oil and identified absorption peaks comparable to those observed in the present study.

4.1.3 FTIR Spectrum of Tween 80

In 2009, Zheng and co-workers prepared a nanoemulsion using Tween 80 as the surfactant and performed FTIR analysis to evaluate its purity, reporting spectral bands similar to those shown in Figure 3C. A strong absorption band observed at 1121.58 cm^{-1} was attributed to C-O stretching vibrations of secondary alcohols.

4.1.4 FTIR Spectrum of Formulation

Drug-excipient interaction was investigated by FTIR analysis. Kuminek et al. (2013) studied the pure Terbinafine HCl spectrum, which showed the same wide peak alkane C-H stretching bands from 2966.89 cm^{-1} to 3305.43 cm^{-1} as present in Figure 3D, indicating the presence of pure TBH in the formulation (Kuminek et al., 2013).

4.2 Physicochemical Evaluation of Formulation

4.2.1 Appearance

Nanoemulsions composed of extremely fine droplets tend to exhibit a transparent appearance, although increasing droplet concentration may lead to a gradual rise in turbidity. Nanoemulsions prepared in this study are shown in Figure 3E.

4.2.2 pH

The negative logarithm (base ten) is defined as pH or the free hydrogen ion concentration in an aqueous solution. As per earlier published literature, variable skin pH values have been recorded, suggesting all variations within the slightly acidic range of pH 4.5–6.5. Table 1 shows pH values of various formulations that agree with those reported in the literature for skin preparations.

Table 1. pH values of different formulations

Formulations	pH values	Formulations	pH values
F1	5.23	F9	5.85
F2	5.65	F10	5.49
F3	5.38	F11	5.56
F4	5.29	F12	5.84
F5	5.26	F13	5.50
F6	5.92	F14	5.63
F7	5.48	F15	5.24
F8	5.13	F16	5.47
OF	5.68		

4.2.3 Drug Content

Drug content of each formulation (Table 2) was interpreted after measuring absorbance at 283 nm, by using the formula:

% Drug content = Absorbance of sample / Absorbance of standard × 100

Table 2. Drug content of various formulations at 283 nm

Formulations	Drug content	Formulations	Drug content
F1	108.32	F9	104.33
F2	104.91	F10	102.59
F3	104.73	F11	105.01
F4	86.71	F12	109.47
F5	105.21	F13	109.97
F6	106.96	F14	106.56
F7	109.30	F15	101.04
F8	102.10	F16	105.69

OF	100.29

4.2.4 Viscosity

Consistency study for Terbinafine HCl nanoemulsion was plotted as graphs (Figure 3F and 3G) that showed viscosity measurements using spindles 1 and 2 at 30 rpm and 60 rpm, respectively. The average viscosity of nanoemulsion with different compositions came out to be 13.2 mPaS to 51.4 mPaS. The terbinafine HCl-loaded nanoemulsion was evaluated using a Brookfield viscometer with temp. set at 25 °C, and the viscosity of the optimized formulation was 17.8–58.7 mPa·s, which is consistent with the results reported in previous studies (Qian et al., 2011).

4.2.5 Size Analysis Results

Nanoemulsion containing Terbinafine HCl was prepared and analyzed for particle size using a ZetaSizer. The results of the optimized formulation showed an average diameter of 57.81 nm, which was comparable with the range stated in the literature. The heterogeneity index of the prepared optimized formulation (Figure 3H) was 0.080, indicating a homogeneous system. The optimized formulation (Figure 3I) showed a zeta potential of −59.1 mV, indicating enough electro-repulsive forces to prevent instability.

4.2.6 Scanning Electron Microscopy

Scanning electron microscopy (SEM) is a powerful analytical technique for ultrastructural analysis. Figure 3J shows particle size distribution within the nanoparticle range. The SEM results of the nanoemulsion showed droplet size in the nanometer range, with no evidence of burst release, indicating efficient drug entrapment within the emulsion droplets.

4.2.7 HPLC Analysis

An injection volume of approximately 10 µL was administered for both standard and sample solutions, and detector responses for the main peaks were monitored at a wavelength of 225 nm. The mobile phase comprised a mixture of acetonitrile, methanol, and phosphate buffer. Both standard and sample preparations were formulated at an equal concentration of 0.2 mg/mL. The reference standard of Terbinafine HCl exhibited a retention time of 21.729 minutes with a corresponding peak area of 14,029,592.6 at 225 nm, as presented in Figure 3K. The retention time of sample preparation was 21.736 with the peak area of 13,841,864.5 at 225 nm, as shown in Figure 3L. The results of both the reference standard and sample preparation were comparable and calculated as:

% age = 13841864.5/14029592.6 × 0.2/0.9873 × 0.983/50.5 × 100 = 98.57%

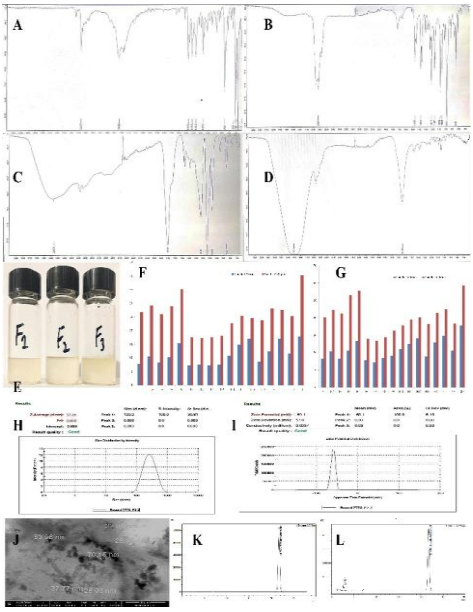

Figure 3. Compatibility study using FTIR and characterization of formulation**.** A, FTIR of Terbinafine HCl; B, FTIR of Eucalyptus oil; C, FTIR of Tween 80; D, FTIR of Formulation; E, Nanoemulsion appearance; F–G, Viscosity graphs; H, Heterogeneity index; I, Zeta potential; J, SEM; K–L, HPLC chromatograms of standard and sample.

Table 3. Permeation study of Terbinafine HCl nanoemulsion

Parameters	1	2	3	4	5	6	7	8	9	10	11	12	13	14	15	16
k0	0.26	0.26	0.15	0.30	0.45	0.13	0.39	0.13	0.24	0.30	0.19	0.301	0.28	0.26	0.38	0.35
Rsqr	0.76	0.89	0.89	0.94	0.84	0.81	0.73	0.84	0.62	0.10	0.51	0.82	0.88	0.56	-0.40	-0.49
k1	0.006	0.006	0.002	0.007	0.01	0.001	0.02	0.01	0.006	0.02	0.003	0.009	0.005	0.008	0.07	0.07
Rsqr	0.90	0.87	0.941	0.80	0.55	0.89	0.53	0.89	0.92	0.72	0.73	0.95	0.68	0.94	0.56	0.606
kH	4.86	4.85	2.84	5.44	8.42	2.53	7.21	2.51	4.56	5.82	3.69	5.56	5.006	4.93	7.29	6.86
Rsqr	0.98	0.93	0.96	0.91	0.96	0.97	0.90	0.96	0.97	0.80	0.92	0.98	0.76	0.95	0.58	0.52
kKP	5.62	2.19	1.57	1.06	5.57	2.23	8.08	1.98	7.17	19.4	7.77	4.6	0.056	8.61	33.7	33.5
Rsqr	0.98	0.95	0.97	0.90	0.96	0.97	0.90	0.96	0.98	0.96	0.97	0.98	0.89	0.98	0.94	0.93

4.3 Drug Permeation Studies

The skin permeation study was carried out using a Franz diffusion cell system. The cumulative quantity of Terbinafine HCl that passed through the diffusion membrane was plotted against time (Figure 4). The optimized nanoemulsion formulation was expected to deliver more than 60% of the drug across the membrane within the first 5 hours. The permeation curve demonstrated a steady, time-dependent rise in drug diffusion with increasing time.

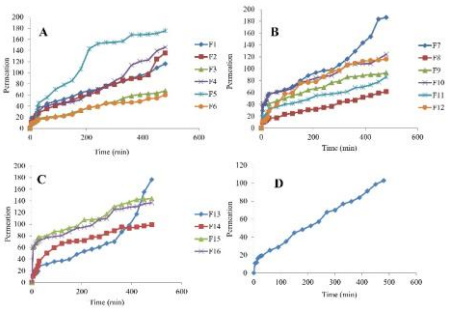

Figure 4. Drug permeation studies (µg/cm²/h) using a Franz diffusion cell**.** A, B, C, and D: Permeation profiles versus time plots showed an increase in drug permeation with increased time.

4.3.1 Kinetic Modeling of Permeation Data

Mathematical modeling contributes to the determination of the drug release from the formulation. Nanoemulsions are liquid topical preparations, and within the first 5 hours 60% of the drug must permeate through the membrane; the kinetic models and the drug content permeation are presented in Table 3. It is pertinent to note that there were 16 formulations that were tested through kinetic modeling.

The release kinetics of Terbinafine HCl from the nanoemulsion showed the best fit with the Korsmeyer Peppas model, exhibiting strong linear correlation and indicating a uniform and controlled drug release behavior.

4.3.2 Mathematical Modeling

Mathematical modeling generated by a design expert for the calculated response and variables:

$$DP = A_0 + AX_1 + BX_2 - CX_3 + ABX_1X_2 + ACX_2X_3 + BCX_1X_3 + A^2X_1^2 + B^2X_2^2 + C^2X_3^2 \quad ....Eq.\ 4.1$$

$$DP = 94.28 + 1.84X_1 + 2.89X_2 - 6.42X_3 + 3.07X_1X_2 + 1.07X_2X_3 + 1.02X_1X_3 + 3.14X_1^2 + 4.04X_2^2 + 0.84X_3^2 \quad ....Eq.\ 4.2$$

Where DP is the response function (Drug permeation), A_0 is a constant; coefficients in Eq. 4.1 are linear (A, B, and C), interaction (AB, AC, and BC), and quadratic (A^2, B^2, and C^2) coefficients, respectively. Response surface analysis of drug permeation data, considering two variables to be compared, showed enhanced permeation of the drug.

4.4 2D and 3D Contour Plots

The contour plots and 3-D response surface plots (Figure 5) demonstrated that both oil and surfactant concentrations positively influenced drug permeation. However, the effect of surfactant concentration on permeation was more significant than that of the oil phase. Surfactants possessing intermediate

hydrophilic-lipophilic balance (HLB) values were found to decrease particle size, which in turn enhanced drug permeation through the skin barrier. Stratum corneum consists of lipophilic membranes; thus, with an increase in solvent, permeation decreases. On the contrary, increased surfactant concentration leads to increased permeation.

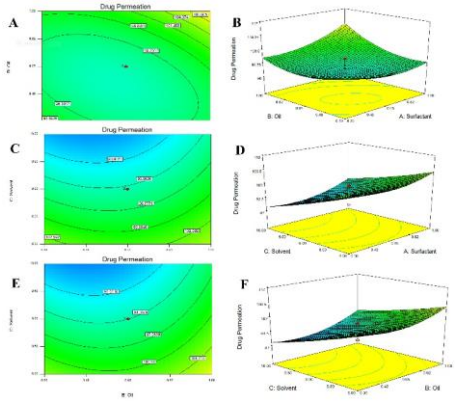

Figure 5. Mathematical modeling was created by a design expert, using 2D contour plots and 3D response surface **plots.** A and B: The 2-D contour plots and 3-D response surface plots graphically illustrate the regression equation and demonstrate the influence of each independent variable on the response.

4.5 Histopathological and Micro-biological Studies

To evaluate the efficacy of the TBH nanoemulsion formulation, its anti-infective potential was further investigated through in vivo animal studies (Figure 6). All experimental groups developed infection before treatment. The untreated control group exhibited more pronounced infection compared to the established brand and TBH-treated groups (Figure 6C). Histopathological assessment was performed on tissue samples collected from the infected sites. The observations indicated improved tissue condition and reduced Candida albicans infection in both the positive control (marketed formulation) and TBH-treated groups compared to the untreated control group (Figure 6F).

Microbiological evaluation was carried out using colony observation and counting. The untreated group showed higher numbers and larger-sized colonies (thirteen small colonies with one large colony), whereas the established brand group demonstrated a reduction in colony number and size (seven small colonies with one large colony). In contrast, the TBH nanoemulsion group exhibited fewer and smaller colonies, with no large colonies observed (Figure 6G).

Overall, the results indicate that terbinafine is effective against Candida albicans, and its antifungal activity appears to be enhanced in the nanoemulsion formulation. Nevertheless, further studies incorporating quantitative CFU determination and appropriate statistical analysis are required to substantiate these findings.

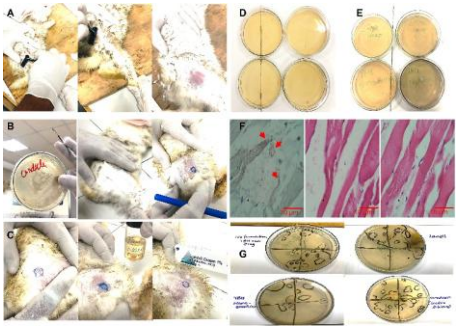

Figure 6. Terbinafine HCl nanoemulsion improves the Candida albicans skin infection in vivo. A: Immunocompromised conditions induced via Cyclophosphamide. B: Hair removal from dorsal skin. C: Untreated infection site. D–F: Histopathological sections. G: Microbiological colony assessment.

Discussion

A transparent TBH Nanoemulsion was prepared, which indicates that the developed formulation has greater stability and homogeneity. According to Zhang and McClements (2018), as nanoemulsions consist of very small droplets (20–200 nm), they are optically transparent products. In the present formulation, Tween 80 was employed as the surfactant.

Use of a surfactant with an intermediate HLB value leads to a clear nanoemulsion. Tween 80 ensured the formation of a clear and homogeneous nanoemulsion with a small droplet size. The prepared TBH nanoemulsion exhibited a PDI value of 0.08, representing a highly even particle size distribution. The pH of the developed TBH formulation was 5.68, which ranges within the normal physiological skin pH range of 4.1–6.5, indicating its suitability for topical application (Proksch, 2018; Das, Nayak, & Nanda, 2013).

Determination of percentage drug content is essential to ensure that each unit dose contains the required amount of active pharmaceutical ingredient for accurate delivery to the infection region (Amichai et al., 2010). The prepared terbinafine hydrochloride nanoemulsion exhibited a drug content of 100.29%, indicating that the formulation falls within acceptable limits. The viscosity of the developed nanoemulsion ranged from 17.8 mPaS to 58.7 mPaS, consistent with findings reported by Qian et al. (2011). The optimized formulation showed a 57.81 nm droplet size, confirming that the nanoemulsion falls within the nanoscale range (<200 nm) (Aqil, Kamran, Ahad, & Imam, 2016). The developed TBH nanoemulsion exhibited a zeta potential of −59.01 mV, indicating excellent stability; generally, zeta potential values >±30 mV are considered desirable as they generate sufficient electrostatic repulsive forces to prevent particle aggregation (Lowry et al., 2016).

Drug release from nanoemulsions is greatly influenced by their surface morphology. SEM analysis of the developed nanoemulsion revealed nanosized particles (<100 nm) with no evidence of burst release, indicating efficient drug entrapment within the emulsion droplets (Divsalar et al., 2012; Saupe, Gordon, & Rades, 2006). The permeation data of the Terbinafine HCl nanoemulsion were analyzed by fitting to multiple kinetic models, including 0-order, 1st-order, Higuchi, and Korsmeyer-Peppas models. The data revealed the Korsmeyer-Peppas model as the best-fitting model. For all data, the correlation coefficient (R^2) was >0.9, indicating good correlation with experimental data (Shah et al., 2010).

Response Surface Methodology (RSM) using a Central Composite Rotatable Design (CCRD) was applied to assess the combined influence of oil, surfactant, and water on drug permeation. The results demonstrated a reduction in drug permeation with increasing solvent concentration, while increased surfactant concentration led to increased permeation (Li & Chiang, 2012; Sood, Jain, & Gowthamarajan, 2014). In vivo studies confirmed the effectiveness of the TBH-loaded nanoemulsion when compared with both the control group and the marketed reference product. While the current study demonstrates the TBH nanoemulsion's effectiveness against fungal infection caused by Candida albicans, the findings also highlighted certain limitations, including the use of animal models that may not fully replicate human skin physiology, predominantly short-term efficacy evaluation, and absence of ex vivo skin permeation studies. Comprehensive long-term stability evaluation and quantitative microbiological analysis with statistical validation will be addressed in future work.

Conclusion

Conclusively, a comprehensive characterization of the Terbinafine HCl nanoemulsion was performed through the systematic evaluation of key physicochemical parameters, including drug content, viscosity, particle size, zeta potential, and surface morphology. The developed nanoemulsion demonstrated favorable physicochemical characteristics, such as high drug loading, optimal viscosity, nanoscale particle distribution, and an appropriate zeta potential, collectively indicating enhanced formulation stability and suitability for

transdermal drug delivery. Scanning electron microscopy confirmed the presence of nano-sized droplets without aggregation, indicating successful drug encapsulation. Permeation studies revealed efficient transdermal delivery of Terbinafine HCl through the nanoemulsion, supported by mathematical modeling showing significant effects of surfactant and aqueous phase on drug permeation. Comparative studies against established brands and controls, including histopathological and microbiological assessments, highlighted the efficacy of the Terbinafine HCl nanoemulsion. In conclusion, the developed Terbinafine HCl nanoemulsion offers a promising platform for topical drug delivery, exhibiting superior characteristics such as stability, permeation enhancement, and efficacy against fungal infections. Further studies may elucidate its clinical applicability and potential for commercialization.

. Ethics Approval and Consent to Participate

In vivo animal experiments were conducted at Al Aleem Medical College. The experimental protocol and study design received approval from the Institutional Ethics Committee under approval number MPH23422.

. Human and Animal Rights

All animal experiments were conducted at Al Aleem Medical College. The study protocol and experimental design were approved by the Institutional Ethics Committee in accordance with the NC3Rs ARRIVE guidelines. Furthermore, all experimental procedures were carried out in strict compliance with the principles described in the "Guide for the Care and Use of Laboratory Animals." No human experimentation was carried out in this study.

. Availability of Data and Material

The present study is original research, and all the relevant data will be made available upon request.

. Funding Declaration

No external funding was obtained for this study.

. Conflict of Interest

All the authors declare no conflict of interest.

. Acknowledgments and Authors' Contributions

Ayesha Rauf conceptualized and designed the study and conducted the experimental work. Nadeem Reyaz performed the histopathological analyses, served as the corresponding author, and prepared the initial manuscript draft. Jureerat Kijsomporn critically revised and corrected the draft, while Tooba Malik finalized the manuscript preparation. Ling Shing Wong reviewed and evaluated the final version of the manuscript. Aqsa Maimoona Malik also served as the corresponding author and contributed to the final editing and refinement of the manuscript. All authors accept responsibility for the integrity, accuracy, and authenticity of the work.

. References

AbdelSamie, S. M., Kamel, A. O., Sammour, O. A., & Ibrahim, S. M. (2016). Terbinafine hydrochloride nanovesicular gel: In vitro characterization, ex vivo permeation and clinical investigation. European Journal of Pharmaceutics and Biopharmaceutics, 108, 82–92.

Abolmaali, S. S., Tamaddon, A. M., Farvadi, F. S., Daneshamuz, S., & Moghimi, H. (2011). Pharmaceutical nanoemulsions and their potential topical and transdermal applications.

Amichai, B., Mosckovitz, R., Trau, H., Sholto, O., Ben-Yaakov, S., Royz, M., . . . Shemer, A. (2010). Iontophoretic terbinafine HCL 1.0% delivery across porcine and human nails. Mycopathologia, 169(5), 323–329.

Aqil, M., Kamran, M., Ahad, A., & Imam, S. S. (2016). Development of clove oil-based nanoemulsion of olmesartan for transdermal delivery: Box-Behnken design optimization and pharmacokinetic evaluation. Journal of Molecular Liquids, 214, 238–248.

Azeem, A., Rizwan, M., Ahmad, F. J., Iqbal, Z., Khar, R. K., Aqil, M., & Talegaonkar, S. (2009). Nanoemulsion components screening and selection: a technical note. Aaps Pharmscitech, 10(1), 69–76.

Barakat, N., Fouad, E., & Elmedany, A. J. P. A. A. (2011). Formulation design of indomethacin-loaded nanoemulsion for transdermal delivery. 2, 1–8.

Campos, F. F., Campmany, A. C. C., Delgado, G. R., Serrano, O. L., & Naveros, B. C. (2012). Development and characterization of a novel nystatin-loaded nanoemulsion for the buccal treatment of candidosis. Journal of Pharmaceutical Sciences, 101(11), 4300–4315.

Chang, Y., & McClements, D. J. (2014). Optimization of orange oil nanoemulsion formation by isothermal low-energy methods. Journal of Agricultural and Food Chemistry, 62(10), 2306–2312.

Chauhan, L., Muzaffar, F., & Lohia, S. (2013). Design, development and evaluation of topical microemulsion. International Journal of Pharmacy and Pharmaceutical Sciences, 5(2), 605–610.

Chiesa, M., Garg, J., Kang, Y. T., & Chen, G. (2008). Thermal conductivity and viscosity of water-in-oil nanoemulsions. Colloids and Surfaces A, 326(1–2), 67–72.

Das, B., Nayak, A. K., & Nanda, U. (2013). Topical gels of lidocaine HCl using cashew gum and Carbopol 940. International Journal of Biological Macromolecules, 62, 514–517.

de Oca-Ávalos, J. M. M., Candal, R. J., & Herrera, M. L. (2017). Nanoemulsions: stability and physical properties. Current Opinion in Food Science, 16, 1–6.

Divsalar, A., Saboury, A. A., Nabiuni, M., Zare, Z., Kefayati, M. E., & Seyedarabi, A. (2012). Characterization and side effect analysis of a newly designed nanoemulsion targeting human serum albumin for drug delivery. Colloids and Surfaces B, 98, 80–84.

Ebrahimi, A. A., & Ghazvini, S. F. (2018). Experimental attrition study of FCC catalysts through 2D/3D contour plots and response surface models. Powder Technology, 336, 80–84.

Elmataeeshy, M. E., Sokar, M. S., Bahey-El-Din, M., & Shaker, D. S. (2018). Enhanced transdermal permeability of Terbinafine through novel nanoemulgel formulation; Development, in vitro and in vivo characterization. Future Journal of Pharmaceutical Sciences, 4(1), 18–28.

Elsheikh, M. A., Elnaggar, Y. S., Gohar, E. Y., & Abdallah, O. Y. (2012). Nanoemulsion liquid preconcentrates for raloxifene hydrochloride: optimization and in vivo appraisal. International Journal of Nanomedicine, 3787–3802.

Franca, A. S., & Oliveira, L. S. (2011). Potential uses of Fourier transform infrared spectroscopy (FTIR) in food processing and engineering. Food Engineering, 211–257.

Hatziantoniou, S., Deli, G., Nikas, Y., Demetzos, C., & Papaioannou, G. T. (2007). Scanning electron microscopy study on nanoemulsions and solid lipid nanoparticles containing high amounts of ceramides. Micron, 38(8), 819–823.

Hildebrand, A., Schaedlich, A., Rothe, U., & Neubert, R. H. (2002). Sensing specific adhesion of liposomal and micellar systems with attached carbohydrate recognition structures. Journal of Colloid and Interface Science, 249(2), 274–281.

Hillgren, A., Lindgren, J., & Aldén, M. (2002). Protection mechanism of Tween 80 during freeze-thawing of a model protein, LDH. International Journal of Pharmaceutics, 237(1–2), 57–69.

Iman, I., Nadia, A., & Ebtsam, M. A. (2010). Formulation and stability study of chlorpheniramine maleate transdermal patch. African Journal of Pharmacy, 4(1).

Karri, V. N. R., Raman, S. K., Kuppusamy, G., Mulukutla, S., Ramaswamy, S., & Malayandi, R. (2015). Terbinafine hydrochloride-loaded nanoemulsion-based gel for topical application. Journal of Pharmaceutical Investigation, 45(1), 79–89.

Khopade, A., Nandakumar, K., & Jainb, N. (1998). Lectin-functionalized multiple emulsions for improved cancer therapy. Journal of Drug Targeting, 6(4), 285–292.

Kim, B. S., Won, M., Yang, Lee, K. M., & Kim, C. S. (2008). In vitro permeation studies of nanoemulsions containing ketoprofen as a model drug. Drug Delivery, 15(7), 465–469.

Kuminek, G., Rauber, G. S., Riekes, M. K., de Campos, C. E. M., Monti, G. A., Bortoluzzi, A. J., . . . Cardoso, S. G. (2013). Single crystal structure, solid state characterization and dissolution rate of terbinafine hydrochloride. Journal of Pharmaceutical and Biomedical Analysis, 78, 105–111.

Li, P.-H., & Chiang, B.-H. (2012). Process optimization and stability of D-limonene-in-water nanoemulsions prepared by ultrasonic emulsification using response surface methodology. Ultrasonics Sonochemistry, 19(1), 192–197.

Lovelyn, C., & Attama, A. A. (2011). Current state of nanoemulsions in drug delivery. Journal of Biomaterials and Nanobiotechnology, 2(05), 626.

Lowry, G. V., Hill, R. J., Harper, S., Rawle, A. F., Hendren, C. O., Klaessig, F., . . . Rumble, J. (2016). Guidance to improve the scientific value of zeta-potential measurements in nanoEHS. Environmental Science: Nano, 3(5), 953–965.

Mostafa, D. M., Kassem, A. A., Asfour, M. H., Al Okbi, S. Y., Mohamed, D. A., & Hamed, T. E.-S. (2015). Transdermal cumin essential oil nanoemulsions with potent antioxidant and hepatoprotective activities. Journal of Molecular Liquids, 212, 6–15.

Nastiti, C. M., Ponto, T., Abd, E., Grice, J. E., Benson, H. A., & Roberts, M. S. (2017). Topical nano and microemulsions for skin delivery. Pharmaceutics, 9(4), 37.

Ng, K. W., & Lau, W. M. (2015). Skin deep: the basics of human skin structure and drug penetration. Percutaneous Penetration Enhancers, 3–11.

Nikam, T. H., Patil, M. P., Patil, S. S., Vadnere, G. P., & Lodhi, S. (2018). Nanoemulsion: A brief review on development and application in Parenteral Drug Delivery. Advanced Pharmaceutical Journal, 3(2), 43–54.

Oliveira, G., Beezer, A. E., Hadgraft, J., & Lane, M. E. (2010). Alcohol enhanced permeation in model membranes. International Journal of Pharmaceutics, 393(1–2), 61–67.

Pant, M., Dubey, S., Patanjali, P., Naik, S., & Sharma, S. (2014). Insecticidal activity of eucalyptus oil nanoemulsion with karanja and jatropha aqueous filtrates. International Biodeterioration & Biodegradation, 91, 119–127.

Proksch, E. (2018). pH in nature, humans and skin. The Journal of Dermatology, 45(9), 1044–1052.

Qian, H., Cui, S., Wang, Q., Wang, C., & Zhou, H. (2011). Fractionation and physicochemical characterization of peach gum polysaccharides. Food Hydrocolloids, 25(5), 1285–1290.

Reza, K. H. (2011). Nanoemulsion as a novel transdermal drug delivery system. International Journal of Pharmaceutical Sciences and Research, 2(8), 1938.

Rojek, B., & Wesolowski, M. (2019). FTIR and TG analyses coupled with factor analysis in a compatibility study of acetazolamide with excipients. Spectrochimica Acta Part A, 209, 280–289.

Saupe, A., Gordon, K. C., & Rades, T. (2006). Structural investigations on nanoemulsions, solid lipid nanoparticles and nanostructured lipid carriers by cryo-field emission scanning electron microscopy. International Journal of Pharmaceutics, 314(2), 56–62.

Shah, P., Bhalodia, D., & Shelat, P. (2010). Nanoemulsion: A pharmaceutical review. Systematic Reviews in Pharmacy, 1(1).

Shi, H., & Xie, Y. (2017). Solubility and thermodynamics of terbinafine hydrochloride in different neat and binary solvents. Journal of Molecular Liquids, 232, 326–333.

Sood, S., Jain, K., & Gowthamarajan, K. (2014). Optimization of curcumin nanoemulsion for intranasal delivery using design of experiment. Colloids and Surfaces B, 113, 330–337.

Sudhakar, B., Ravi Varma, J., & Ramana Murthy, K. (2014). Formulation, characterization and ex vivo studies of terbinafine HCl liposomes for cutaneous delivery. Current Drug Delivery, 11(4), 521–530.

Suyal, J., & Bhatt, G. (2017). An introductory review article on nanoemulsion. Journal of Pharmacognosy and Phytochemistry, 2, 35–40.

Tanyildizi, M. S., Özer, D., & Elibol, M. (2005). Optimization of α-amylase production by Bacillus sp. using response surface methodology. Process Biochemistry, 40(7), 2291–2296.

Tsai, M.-J., Fu, Y.-S., Lin, Y.-H., Huang, Y.-B., & Wu, P.-C. (2014). The effect of nanoemulsion as a carrier of hydrophilic compound for transdermal delivery. PloS One, 9(7), e102850.

Zhang, Z., & McClements, D. J. (2018). Overview of nanoemulsion properties: stability, rheology, and appearance. In Nanoemulsions (pp. 21–49). Elsevier.

Zheng, Y., Eli, W., & Li, G. (2009). FTIR study of Tween80/1-butyl-3-methylimidazolium hexafluorophosphate/toluene microemulsions. Colloid and Polymer Science, 287(7), 871–876.

Zhou, H., Yue, Y., Liu, G., Li, Y., Zhang, J., Gong, Q., . . . Duan, M. (2010). Preparation and characterization of a lecithin nanoemulsion as a topical delivery system. Nanoscale Research Letters, 5(1), 224–230.

UCP Journal of Science and Technology
Vol. 3, Issue 2 (January - June 2026)
Journal website: http://ojs.ucp.edu.pk/index.php/ucpjst/index

In Silico Insights into the Impact of Deleterious SNPs on the Functioning and Dynamics of TP53 and Its Targeted Therapy by COTI-2 and PRIMA1 in Breast Cancer Patients

Ambreen[1]*, Iltamaa Khurram[1], Tooba Khan[1], Heera Batool[1]

Abstract

Breast cancer is the most frequent malignancy in women globally and has a high death rate. In Pakistan, one in every nine women is at risk. Tumor protein 53 (TP53) is a transcription factor that suppresses tumors by regulating gene expression in response to stress. In 40-60% of breast tumors, mutations in TP53 contribute to tumor growth, medication resistance, and a poor prognosis. This study uses an in silico approach to find deleterious missense SNPs in TP53 and assess their effects on protein dynamics. Deleterious TP53 variants were screened through SNP prediction tools. Four of the 25 detected deleterious variants (Q16K, L130Q, P223R, and R273I) were chosen based on two criteria: pathogenicity threshold (>80%) and their presence in functionally significant domains. Structural stability studies using I-Mutant2.0 and MUPro revealed that L130Q is the most destabilizing variant, showing consistently lower stability across both tools. By contrast, R273I is predicted to be stabilizing in MUPro and Dynamut, whereas I-Mutant considers it destabilizing. Molecular docking analysis was performed using CB-dock to explore mutant TP53 interactions with small-molecule inhibitors COTI-2 and PRIMA. This study reveals the structural instability caused by *TP53* mutations and their impact on drug interactions. To restore TP53 activity and improve the effectiveness of TP53-targeted inhibitors in breast cancer treatment, future research should investigate targeted therapeutic approaches.

Keywords: Breast Cancer, Tumor Suppressor Gene, Missense Variant, TP53, Protein Dynamics, Molecular Docking.

1 Introduction

Breast cancer (BC) is currently regarded as a serious public health concern (Lundberg & Phoosuwan, 2022) since it is the most common type of cancer among women globally (Siegel, Miller, & Jemal, 2018). Breast cancer is the fifth leading cause of death from cancer. Around 7.8 million women were diagnosed with breast cancer in the last five years worldwide. Moreover, breast cancer is predicted to become more common in Pakistan, where one in nine women is at risk of getting the disease, which is said to be the highest rate in Asia. (Sohail & Alam, 2007)Hereditary factors and genetic abnormalities that may result in abnormal cell proliferation,

[1]Informatix Biolabs, Lahore, Pakistan
*Corresponding author's E-mail: ambreenhussain2002@gmail.com
Received: 26 April 2025; Received in revised form: 16 June 2026; Accepted: 18 June 2026.
Available online: 13 July 2026.

DOI: https://doi.org/10.24312/ucp-jst.03.02.523

suppression of apoptosis, and an increase in angiogenesis and metastasis have been the subject of much recent discussion (Lukong, 2017). According to an estimation, 20% of individuals have a family history of breast cancer, while 5–10% have hereditary BCs, which are brought on by germline mutations in tumor suppressor genes such as TP53, PTEN, BRCA1, and BRCA2 (Economopoulou, Dimitriadis, & Psyrri, 2015). Although the primary treatments for breast cancer are radiotherapy, chemotherapy, and surgery, patients with advanced-stage tumors have a poor prognosis with serious adverse consequences. Therefore, alternative screening methods are required in developing and underdeveloped countries (Nounou et al., 2015).

For many years, the main goal of genetics has been to identify genetic variations that might contribute to the onset and course of complex diseases like cancer. It could be useful to identify risk variables for both prognosis and disease prevention. However, this is costly and time-consuming (Singh et al., 2021). Fortunately, bioinformatics advancements have made it easier to screen for single-nucleotide polymorphisms (SNPs) in the genome that may be linked to diseases (Khan et al., 2022). These tools can assess SNPs from a variety of categories, including frameshift, nonsense, untranslated regions (UTRs), promoter regions, splice sites, and missense/non-synonymous. Of these mutations, non-synonymous SNPs (nsSNPs) and nonsense SNPs are considered coding variants because they directly affect a protein's folding and function. (Mooney, 2005) In silico tools for analysing the harmful effects of SNPs often use information gathered from sequences, protein structural properties, mutant and wild-type residue properties, and the evolutionary conservation of nucleotides or amino acids. (Selga, Koc, Chawade, & Ortiz, 2020) The use of functional bioinformatics has aided researchers in identifying possible disease-causing variations that may be confirmed by genotyping or sequencing-based experiments (Emadi, Akhoundi, Kalantar, & Emadi-Baygi, 2020).

Previous studies have shown that P53 codes for a transcription factor known as tumor protein 53, which contributes to the development of BC (Ahmad et al., 2023; Li et al., 2020). It is a tumor suppressor that regulates the cell-cycle checkpoint, senescence, DNA repair, apoptosis, and other processes. About 40–60% of BC cases have somatic TP53 mutations, which are prevalent in many cancer types (Pollock et al., 2022). Their TP53 status greatly influences cancer patients' dependence on a wide range of anticancer therapies that are highly associated with a poor prognosis in breast cancer (O'Connor et al., 1997) because they can potentially cause medication resistance, relapse, and disease failure. About 80% of triple-negative breast cancers have TP53 mutations because they frequently accompany clinically aggressive tumors. (Cheng, Ding, Xu, Zhu, & Jia, 2020). In addition to having a high risk of metastasis and recurrence in clinical settings, triple-negative breast cancer has significant resistance to chemotherapy and radiation therapies (Bai, Ni, Beretov, Graham, & Li, 2021). TP53 is activated through various receptors and activates the main downstream signalling pathways, which can ultimately lead to the development of cancer (Wang, Guo, Wei, & Chen, 2023). Inhibiting TP53 mutations and restoring mutant p53 function are two possible therapy approaches for p53 mutations (Liu et al., 2019). Based on the distinct functional limitations and varied structure of mutant p53, several techniques are being explored to restore p53 function (Bykov, Eriksson, Bianchi, & Wiman, 2018). Drugs like PRIMA-1 and COTI-2

have promising therapeutic strategies for cancer treatment because they reactivate P53 mutants by restoring its tumor-suppressing power and inducing cancer cell death (Lu et al., 2016). Therefore, this study aims to filter the most deleterious missense SNPS of TP53, observe the impact of variations in the DNA-binding domain and transactivation domain on protein dynamics and stability, and unravel the impact of targeted inhibition by COTI-2 and PRIMA1.

The novelty of the study stems from the fact that, while many studies have investigated TP53 mutations in cancer, the majority have either focused on the structural consequences of a small number of alterations or on the prevalence and clinical significance of frequently occurring mutations. The present study, on the other hand, employs a comprehensive in silico approach that includes pathogenicity identification, structural and functional analysis, protein stability and flexibility evaluations, gene ontology annotation, and therapeutic assessment of mutant TP53. Furthermore, this analysis goes beyond the well-known hotspot mutations and investigates four well-established and less-studied detrimental TP53 variants (Q16K, L130Q, P223R, and R273I) with the goal of expanding the knowledge about these mutations. Another unique aspect of this investigation is the comparison of two mutant p53-targeting drugs, COTI-2 and PRIMA-1, against both wild-type and mutant TP53 proteins. This study offers a more comprehensive knowledge of how particular TP53 variations may affect protein behavior and therapeutic response in breast cancer by integrating mutation prioritization with structural and pharmacological investigations.

2 Methodology

2.1 Sequence Retrieval

The nucleotide and amino acid sequences of the human cellular tumor antigen p53 (TP53) with accession number P04637 were downloaded in FASTA format from the National Center for Biotechnology Information (NCBI) (https://www.ncbi.nlm.nih.gov/).

2.2 Retrieval of Mutational Hotspots Data

SNP information for the human TP53 gene, having accession ID ENSG00000141510, genome assembly GRCh38:CM000679.2, and transcript ID ENST00000269305.9, was retrieved on February 21, 2025, using the Ensemble Genome Browser version 113 (https://asia.ensembl.org/index.html). Different types of variations were observed throughout the length of the TP53 protein**.** In this study, nonsynonymous variants, specifically missense variants of TP53, were retrieved from the database.

2.3 Selection of Deleterious Missense Variants

The pathogenicity of missense SNPs was predicted using 5 dbSNP consensus tools such as SIFT (Sim et al., 2012), PolyPhen (Adzhubei, Jordan, & Sunyaev, 2013), CADD (Rentzsch, Witten, Cooper, Shendure, & Kircher, 2019), MetaLR, and MutationAssessor (Reva, Antipin, & Sander, 2011). Data from these tools are also integrated into the Ensembl genome browser. Chromosomal coordinates, altered base and amino acid information of SNPs, and the transcript ID are among the data that the dbSNP tool offers. Based on the criteria outlined in Table 1, the pathogenicity scores of the above-mentioned SNP tools were subsequently acquired to filter the most deleterious missense SNPs of the TP53 gene (Supplementary File**).** The highly anticipated pathogenicity of the SNPs led

Table 1. Tools used to identify deleterious SNPs of the TP53 gene.

SNP Tool	Score	Interpretation	Reference
SIFT	0 or 1	Tolerated or Deleterious	(Sim et al., 2012)
PolyPhen	0 or 0.5 or 1	Benign or Possibly Damaging or Probably Damaging	(Adzhubei et al., 2013)
CADD	0 or 1	Likely Benign or Likely Deleterious	(Rentzsch et al., 2019)
MetaLR	0 or 1	Tolerated or Damaging	-
Mutation Assessor	0 or 0.5 or 1	Low, Medium, or High	(Reva et al., 2011)

to their selection. Since mutations in different TP53 domains have varied functional effects, further filtration was also carried out based on the location of the 25 most harmful variations. L130Q had an 80% pathogenicity score, whereas Q16K, P223R, and R273I all had a 90% pathogenicity score. While L130Q, P223R, and R273I were discovered from TP53's DNA-binding core domain, which is crucial for TP53's tumor suppressor activity, Q16K was detected from the transactivation domain. These variations were picked because they may impact the structure, function, and DNA interaction of TP53, which could result in cancer.

All nsSNPs in the TP53 gene were collected from publicly available databases and subjected to a rigorous filtering process to identify high-confidence detrimental alterations. Entries with inadequate annotation and synonymous variations were removed during the initial screening stage. The remaining missense variations were ranked using a consensus of many in silico functional prediction methods, including SIFT, PolyPhen-2, and PROVEAN. Variants that were reliably predicted to be detrimental or harmful across most of these networks were retained for further examination. To further refine the criteria, evolutionary conservation of affected residues was assessed; highly conserved sites were assumed to be more likely to be functionally important. Protein stability changes following mutation were evaluated using the available prediction techniques, and variants anticipated to severely destabilize the TP53 protein were given priority. Furthermore, variants were cross-referenced with the ClinVar and dbSNP databases to include clinical significance comments, and known benign polymorphisms were eliminated from the dataset. Where allele frequency information was provided, frequent variants (minor allele frequency > 0.01) were removed to focus on rare, potentially disease-associated mutations. Our multi-step integrative approach ensured that only high-confidence detrimental TP53 SNPs were selected for further structural and functional analyses.

2.4 Physicochemical Properties Analysis

The physicochemical characteristics of the TP53 protein were calculated using the ExPaSy ProtParam tool (https://web.expasy.org/protparam/), which computed metrics such as molecular weight, atomic and amino acid composition, theoretical pI, extinction coefficient, instability index, estimated half-life, aliphatic index, and the grand average of hydrophobicity (GRAVY).

2.5 Evolutionary Conservation and Phylogenetic Analysis

The progressive alignment of amino acid sequences of TP53 gene isoforms (P53α, P53β, and P53γ) was carried out using Clustal Omega (https://www.ebi.ac.uk/jdispatcher/msa/clustalo). The analysis revealed information on conserved domains among the variants, demarcating structurally and functionally important areas. As different TP53 isoforms play differential roles in tumor suppression, knowing their sequence conservation aids in the evaluation of how mutations could affect TP53 differently in breast cancer. To gain a better understanding of evolutionary conservation, phylogenetic analysis of all the TP53 protein isoforms was carried out using MEGA11, employing 1000 bootstrap replicates and the Maximum Likelihood methodology. The analysis identified the evolutionary divergence of TP53 isoforms along with conserved regions that would be more functionally essential. Through the identification of mutations within these conserved domains, we can better grasp their possible role in TP53 dysfunction and in the development of breast cancer.

2.6 Domain Analysis

The domain analysis of TP53 was carried out using InterPro (https://www.ebi.ac.uk/interpro/search/text/), a program that groups proteins into families and forecasts domains and significant areas to offer functional analysis of the target protein. The transactivation domain (TAD), proline-rich region, DNA binding domain, tetramerization domain, and regulatory region were among the TP53 domains. A particular range of amino acid sequences defined these locations. The tertiary structure of individual domains was then obtained using these sequences in PYMOL (https://www.pymol.org/), which was subsequently utilized to depict the TP53 exploded view. As the identified variants are in disparate domains of TP53, the exploded view representation in PyMOL was utilized to give structural insights into the respective domains containing these SNPs. This view emphasizes the spatial arrangement of the mutations in the protein structure.

2.7 Primary and Secondary Structure Prediction

Ensembl genome browser (https://www.ensembl.org/) was used for the retrieval of the TP53 gene sequence having Ensembl ID: ENSG00000141510**.** The genomic sequence was translated into protein using the ExPaSy Translate tool (https://www.expasy.org/), and the longest open reading frame was located and used for further analysis. Secondary structure prediction of TP53 helps identify functional domains (e.g., DNA-binding regions) and structural vulnerabilities linked to mutations in cancer. PSIPRED (https://bioinf.cs.ucl.ac.uk/psipred/) was used for secondary structure prediction and functional analysis. The PSIPRED Workbench is a computational platform offering diverse tools for predicting protein structural and functional features. By analyzing amino acid sequences, it facilitates predictions such as secondary structure elements (e.g., alpha-helices, beta-strands), identification of disordered segments, and arrangement of transmembrane helices in the TP53 protein.

2.8 Tertiary Structure Prediction

The online protein modeling database AlphaFold (https://alphafold.ebi.ac.uk/), which is based on the ab initio technique, was used to predict the tertiary structure of TP53. PyMOL (https://www.pymol.org/), a molecular visualization tool, was used to visualize the 3-D structure of the 393 amino acid long TP53 protein with UniProt ID "P04637," which was retrieved in PDB format from AlphaFold.

Table 2. Physicochemical attributes of COTI-2 and PRIMA1 retrieved from the PubChem Database.

Compound Name	COTI-2	PRIMA1
Pubchem CID	74334923	322968
Molecular Weight (g/mol)	366.5	185.22
Molecular Formula	$C_{19}H_{22}N_6S$	$C_9H_{15}NO_3$
SMILES	C1CC2=C(C(=NNC(=S)N3CCN(CC3)C4=CC=CC=N4)C1)N=CC=C2	C1CN2CCC1C(=O)C2(CO)CO
Structure	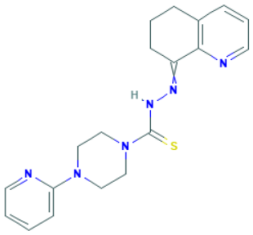	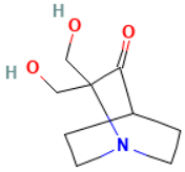

2.9 Validation and Refinement of Predicted Structure

UCLA-DOE LAB—SAVES v6.0 (https://saves.mbi.ucla.edu/) was used to validate the quality of the predicted TP53 structure. Protein structures were verified using the ERRAT server, where the error function is derived from the reported structure's non-bonded atom-to-atom interaction data. The "stereochemical quality" of the target protein structure was evaluated using PROCHECK's Ramachandran plot. Through the Galaxy web server (https://galaxy.seoklab.org/index.html), the TP53 structure was further refined.

2.10 Structural Homology Assessment

The structure of 1AIE (deep teal), which is the crystal structure of the tetramerization domain of TP53, was obtained in PDB format from the Protein Data Bank (https://www.rcsb.org/), and its superimposition with complete wild-type TP53 (blue) was carried out via PYMOL. The overlapping regions between the two sequences illustrated the structural alignment. This allowed for the validation of the structural homology of the AlphaFold-predicted TP53 structure (model).

2.11 Prediction of Subcellular Location

The subcellular location of the human TP53 protein was predicted using DeepLoc-1.0 (https://services.healthtech.dtu.dk/services/DeepLoc-2.0/), which predicts localization based on the likelihood score for each organelle. The likelihood that a protein will be found in a specific organelle increases with a higher value, and vice versa. A server called SecretomeP 1.0f (https://services.healthtech.dtu.dk/services/SecretomeP-1.0/), which generates ab initio predictions of non-classical protein secretion in eukaryotes, further validated the location and nature of the TP53 protein.

2.12 In-situ Mutagenesis

In situ mutagenesis was induced in wild-type TP53 at amino acid coordinates Q16K (rs2151047550), L130Q (rs2151033511), P223R (rs138983188), and R273I (rs121912660) via PyMOL (https://www.pymol.org/), and the structures were saved in PDB format.

2.13 Stability and Flexibility Analysis

Online tools such as MUPro (https://mupro.proteomics.ics.uci.edu/) and I-Mutant (https://folding.biofold.org/cgi-bin/i-mutant2.0.cgi) were used to study and illustrate the effect of the

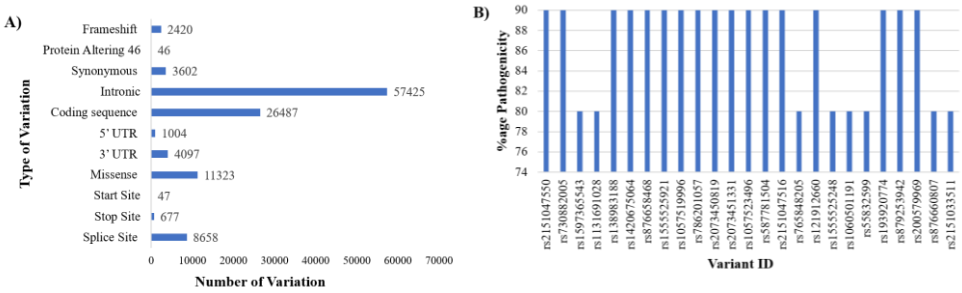

Figure 1. The distribution and pathogenicity of TP53 gene-associated SNPs retrieved from the ENSEMBLE genome browser. **(A)** The bar graph classifies many types of variations found in the TP53 gene, such as intronic, coding sequence, missense, synonymous, frameshift, and splice site variations, and their corresponding frequencies. **(B)** The histogram depicts the estimated pathogenicity of chosen deleterious variants in TP53, with the 80% and above the pathogenicity threshold, as assessed by SNP tools.

mutations on the stability of the protein. In the I-Mutant server, DDG values less than 0 indicate destabilization, while values greater than 0 indicate higher stability. In MUPro, the protein stability indicator was the Delta G value, where a decrease in the Delta G value indicates increased protein stability and vice versa. Whereas the DynaMut server (https://biosig.lab.uq.edu.au/dynamut/) was used to observe the effect of mutations on protein flexibility and stability. The results were represented in the form of vibrational entropy change (DDG) and free energy. This analysis is important because it defines the pattern of interaction of mutant proteins with others.

2.14 Gene Ontology Analysis

GO annotations of the TP53 protein are typically derived from experimental evidence, literature, and computational methods and taken from PSIPRED (https://bioinf.cs.ucl.ac.uk/psipred/). The Gene Ontology encompasses three primary domains: molecular functions, biological processes, and cellular components.

2.15 Ligand Structures Retrieval

The structural and functional characteristics of compounds, namely COTI-2 and PRIMA1, with IDs 74334923 and 322968, respectively, were obtained using the PubChem database (https://pubchem.ncbi.nlm.nih.gov/) on February 26, 2025. To carry out molecular docking, ligands' three-dimensional structures were retrieved in SDF format. Table 2 shows the general attributes of the compounds selected for docking with wild-type and mutant TP53 proteins.

2.16 Pharmacokinetic Analysis

The pharmacokinetics of the chosen inhibitors were investigated using SwissAdme (http://www.swissadme.ch/). The filtration parameters were determined to be: Molecular mass (Mw) < 500 Daltons; hydrogen bond donor (HBD) and acceptor (HBA) parameters < 5; number of rotatable bonds < 10; and log P (octanol-water partition coefficient) parameter < 5. (Supplementary File).

2.17 Molecular Docking

The wild-type TP53 and its variations (Q16K, L130Q, P223R, and R273I) were molecularly docked with inhibitors such as COTI-2 and PRIMA1 using CBDock 2 (https://cadd.labshare.cn/cb-dock2/). The 3D complexes were then visualized in PyMol, and the 2D interactions were visualized in Ligplot. The docking tool produced five different poses for every protein-ligand combination. The best pose was picked based on the Vina score, and the complex with the lowest scoring

Table 3. TP53 deleterious variants with 80% and above percentage pathogenicity threshold.

Sr. No.	Variant ID	Percentage Pathogenicity	Residue	Residue Coordinates
1	**rs2151047550**	**90**	**Q/K**	**16**
2	rs730882005	90	C/F	238
3	rs1597365543	80	G/S	226
4	rs1131691028	80	E/V	224
5	**rs138983188**	**90**	**P/R**	**223**
6	rs1420675064	90	P/R	219
7	rs876658468	90	H/D	193
8	rs1555525921	90	A/S	189
9	rs1057519996	90	K/R	132
10	rs786201057	90	T/M	125
11	rs2073450819	90	K/R	120
12	rs2073451331	90	A/G	119
13	rs1057523496	90	F/I	109
14	rs587781504	90	G/V	105
15	rs2151047516	90	E/V	17
16	rs765848205	80	M/R	230
17	**rs121912660**	**90**	**R/I**	**273**
18	rs1555525248	80	G/R	272
19	rs1060501191	80	E/Q	264
20	rs55832599	80	R/W	260
21	rs193920774	90	G/V	259
22	rs879253942	90	L/Q	258
23	rs200579969	90	G/S	255
24	rs876660807	80	N/Y	232
25	**rs2151033511**	**80**	**L/Q**	**130**

function was selected for further analysis. The wild-type and mutant proteins were docked with PRIMA-1 using the following grid box parameters: (8, -9, and 5) along the x, y, and z axes, respectively. The grid box coordinates for the x, y, and z axes in COTI-2 were (-8, 16, 26), respectively. The interaction between residues was further validated through Ligplot.

3. Results

3.1 Variant Selection and Filtration of Deleterious Missense SNPs

115786 variants were identified in TP53 SNP data, including coding regions (e.g., start and end codons, synonymous and nonsynonymous variations) and regulatory regions (e.g., splice sites, intronic regions, and UTR regions) along the length of the TP53 protein (Figure 1A). Specifically, the impact of missense

Table 4. Analysis of physicochemical properties of TP53 Protein.

Properties	WILD TYPE	Q16K	P223R	R273I	L130Q
Amino Acids	393	393	393	393	393
Molecular Weight (Da)	43653.18	43653.22	43712.25	43610.15	43668.15
pI	6.33	6.47	6.47	6.20	6.33
GRAVY	-0.756 (slightly hydrophilic)	-0.757	-0.764	-0.733	-0.775
Instability index	73.59 (unstable)	72.61 (unstable)	72.47 (unstable)	73.38 (unstable)	73.59 (unstable)
Aliphatic index	59.08	59.08	59.08	60.08	58.09
Estimated coefficient value	36,035	36035	36035	36035	36035

variations (11323 in total) on the structure and function of the TP53 protein was observed in this study (Supplementary file). Five different consensus tools, namely SIFT, PolyPhen, CADD, MutationAssessor, and MetaLR, were utilized to filter out deleterious variants and estimate % pathogenicity. 25 missense variations were estimated to be deleterious by 80% of the aforementioned tools, based on the cumulative study of the SNP effect (Figure 1B**).** The tools evaluate the pathogenicity of variants by assigning scores. SIFT assigns scores from 0 (tolerated) to 1 (deleterious). PolyPhen

A)

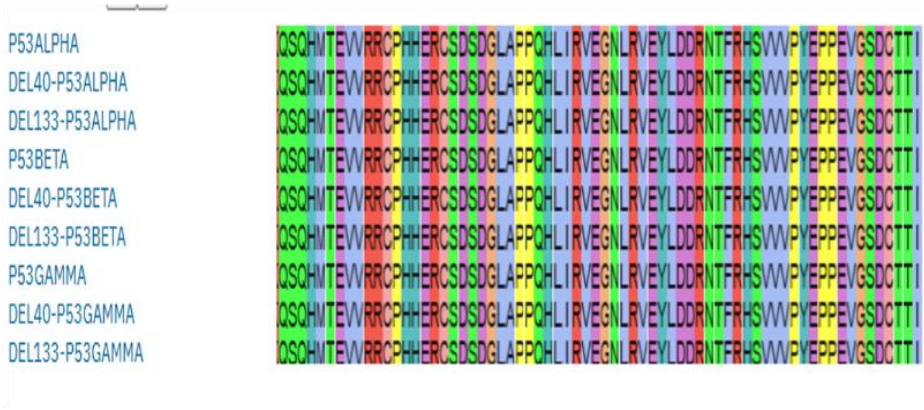

Figure 2. Evolutionary conservation and phylogenetic analysis of isoforms of TP53. **(A)** Multiple sequence alignment among highly related sequences of TP53 isoforms. The image employs the Clustal2 color scheme, with red representing positively charged residues, green polar, magenta negatively charged, yellow polar, cyan nonpolar, and blue hydrophobic residues**.**

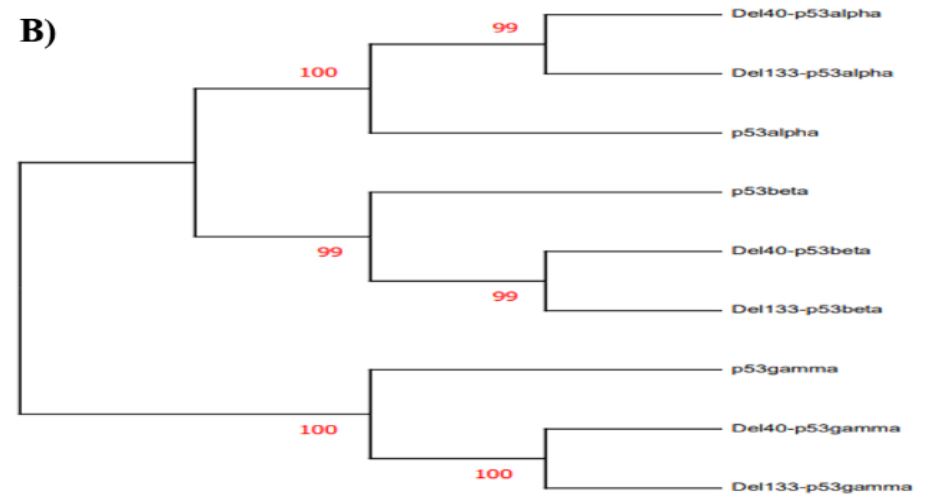

Figure 2. Evolutionary conservation and phylogenetic analysis of isoforms of TP53. **(B)** Phylogram of TP53 isoforms depicting evolutionary relationship.

classifies them as 0 (benign), 0.5 (possibly damaged), and 1 (probably damaged); CADD categorizes them as 0 (likely benign) or 1 (likely deleterious). Furthermore, MetaLR differentiated between tolerated (0) or damaging (1), and Mutation Accessor graded variants into low (0), medium (0.5), and high (1). Out of 25 filtered variants, 4 variants, namely Q16K, L130Q, P223R, and R273I, were randomly picked from the TAD and DNA-binding domain of TP53 **(Table 3).** The distribution of deleterious variants was observed to be significantly higher in the DNA-binding domain of TP53 than in the TAD or any other domain.

3.2 Physicochemical Properties Analysis

The structural and functional differences between human TP53 and its variants were assessed by analyzing their physicochemical properties. There were minor differences in the molecular weight, with R273I having the lowest (43610.15 Da) and P223R having the highest (43712.25 Da) molecular weight. The pI increased in Q16K and P223R (6.47) but decreased in R273I (6.20), suggesting potential charge variations. The change in GRAVY value is also seen, from slightly hydrophilic (-0.756) to most hydrophilic (-0.775). Across all the variants, the instability index remained unstable with minimal stability gains in Q16K and P223R. The aliphatic index changed slightly, with the most thermostable being R273I (60.08). These results indicate that TP53 stability, solubility, and expression level may be indirectly affected by mutations. (Table 4).

3.3 Evolutionary Conservation and Phylogenetic Analysis

The alignment represents amino acids of the isoforms of TP53 with differentiated colors to show conservation and functional similarity. Specific deletions were indicated in Del40-P53α and Del133-P53β variants. Most of the residues were found to be conserved in all isoforms of TP53. Figure 2A displays the sections of amino acids that are well conserved and also the level of conservation status. On the other hand, the color scheme depicts the characteristics of the amino acid residues. The Maximum Likelihood phylogenetic tree was constructed with the help of

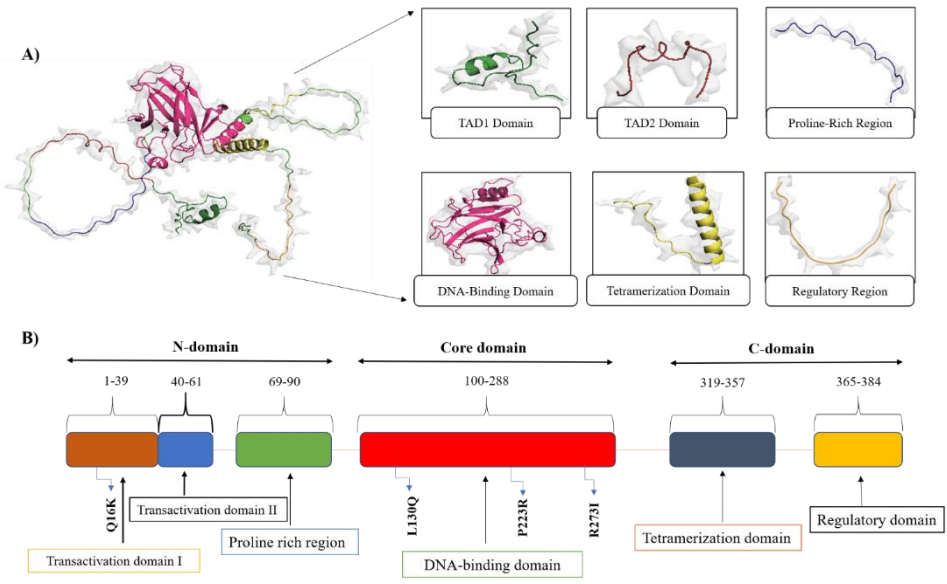

Figure 3. Domain Analysis of TP53. **(A)** Exploded view of all the domains of the predicted 3D structure of TP53. (Green color: TAD1 domain (1-39aa), red: TAD2 domain (40-61aa), blue color: Proline-rich region (69-90aa), pink color: DNA binding domain (100-288aa), yellow color: Tetramerization domain (319-357aa), orange color: Regulatory region (365-384aa)). **(B)** Sequential display of all the domains of the TP53 protein.

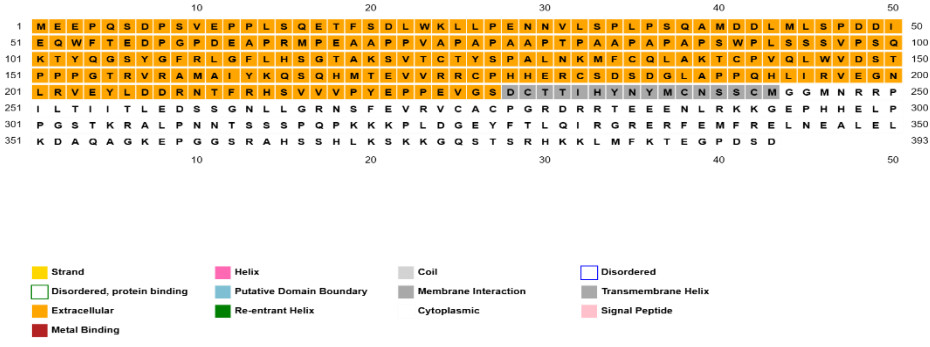

Figure 4. (A) The N-terminal region (residues 1-200) is rich in β-strands (yellow), while the C-**terminal** (251-393) appears largely unstructured. Additional features include metal-binding sites, helices, and disordered regions, indicating possible functional roles in protein stability and interactions.

MEGA11 software to depict the evolutionary relationship of the nine isoforms of P53 (P53α, P53β, P53γ, and their deletion variants). The P53 alpha, beta, and gamma form distinct clades with their deleted variant, i.e., Del40 and Del133. The bootstrap value was represented by numbers (99, 100), which depict the statistical measurement of confidence of each group. A value of 100 indicates very high confidence in the grouping, while 99 value numbers are considered highly reliable (Figure 2 B).

3.4 Domain Analysis

The transactivation domain, proline-rich area, DNA binding domain, tetramerization domain, and regulatory region are the five primary domains that

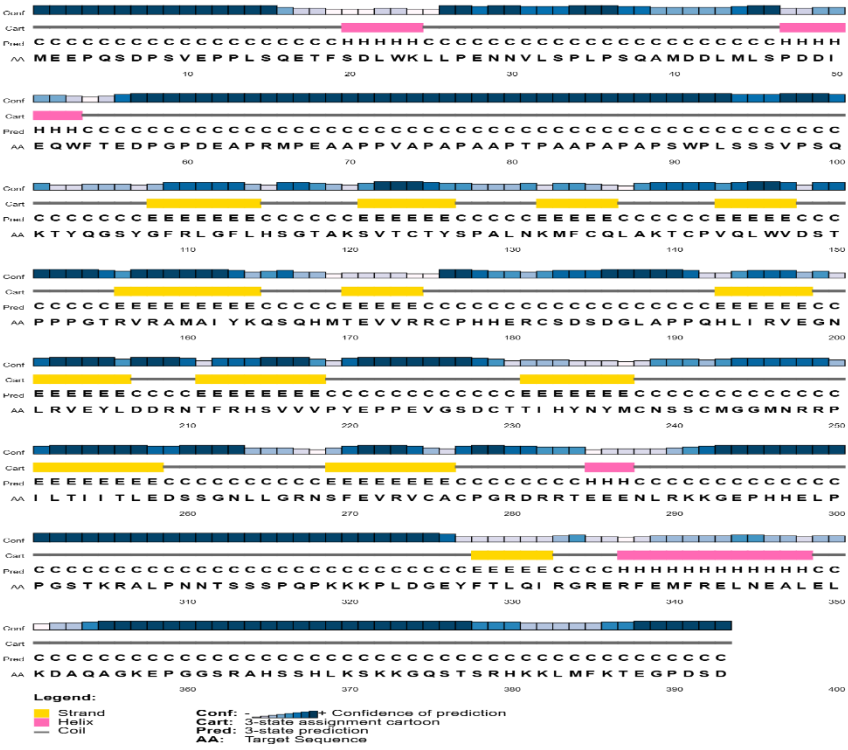

Figure 4. (B) The sequence depicts secondary structure prediction of the TP53 protein, highlighting helices (pink), β-strands (yellow), and coils (white). Confidence scores (blue bars) indicate prediction reliability.

have been identified in TP53. With a length of 1-61 residues, the transactivation domain (TAD) was separated into two domains: TAD1 (1-39 residues) and TAD2 (40-61 residues). The DNA-binding domain ranges from 100 to 288 residues, the tetramerization domain ranges from 319 to 357 residues, the regulatory area spans from 365 to 384 residues, and the proline-rich region extends from 69 to 90 residues (Figure 3B). Using PyMOL, each domain designated by a specific range of amino acids was highlighted in a different color (Figure 3A). The TAD domain of TP53 regulates gene transcription through interaction with coactivators such as p300; in contrast, the DNA-binding domain stabilizes the attachment of the target gene to TP53. Alterations in these domains affect TP53's tumor suppressor function, leading to cancer progression.

3.5 Primary and Secondary Structure Prediction

The genomic sequence of TP53 was successfully obtained from the Ensembl genome browser with the ID ENSG00000141510 and was precisely translated into a protein sequence through the ExPASy Translate tool. The longest open reading frame was selected for further structural and functional study to analyze the mutation correlated with breast cancer. The predicted secondary structure of TP53 demonstrated a composition of β-strands (yellow), α-helices (pink), and extensive coil regions (blue/gray), as determined by PSIPRED. These coil regions suggest structural flexibility or

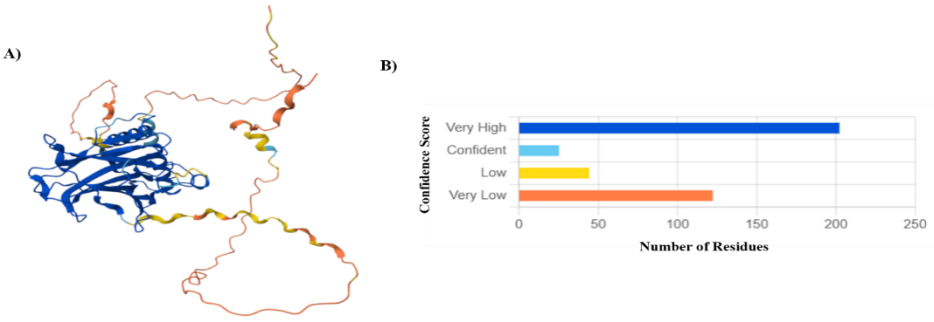

Figure 5. 3-D structural prediction of TP53. **(A)** AlphaFold predicted the tertiary structure of TP53. **(B)** Model confidence of each of the amino acid residues of TP53.

disorder, while the β-strands and α-helices likely stabilize functional domains critical for its activity. Sequence analysis further underscored extracellular motifs and potential membrane-binding sites, offering insights into TP53's structural architecture and biologically relevant regions. (Jones, 1999)

3.6 Tertiary Structure Prediction

The 3-D structure of the human TP53 protein was predicted and retrieved in PDB format from AlphaFold and was then visualized in PyMOL (Figure 5A). In addition, AlphaFold generates a per-residue confidence score (plDDT) ranging from 0 to 100 to determine the expected precision of a protein's overall 3-D structure. The more certain the tool is in the accuracy of the anticipated structure, the higher the score (Figure 5B). In terms of plDDT (global), the TP53 model confidence was 75.13.

AlphaFold showed a high confidence score for most of the amino acid residues, i.e., 227 out of 393, affirming the high accuracy of the predicted 3-D protein structure of TP53 (Table 5).

3.7 Validation and Refinement of Predicted Structure

The accuracy of the predicted protein structure is mostly dependent on the bond angles (phi and psi) of amino acids, which affect a model's quality estimate. According to the Ramachandran plot, phi and psi bond angles were present in the most favored region for 78.3% of amino acid residues (253), the additionally allowed region for 15.2% (49), the generously allowed region for 4.6% (15), and the disordered region for 1.9% (6) of amino acid residues. The predicted protein model of TP53 was verified to be accurate since the majority of amino acid residues (98.1%) are located in the quadrants that represent stable secondary structures (Figure 6A**).** Furthermore, by highlighting areas with high error values, the ERRAT plot evaluated the accuracy of the predicted TP53 structure. An ERRAT

Table 5. Confidence score per amino acid residue of TP53 based on piDDT score.

Color	Model Confidence	plDDT Score	Number of amino acids
	Very high	>90	202
	Confident	>70 but <90	25
	Low	>50 but <70	44
	Very Low	<50	122

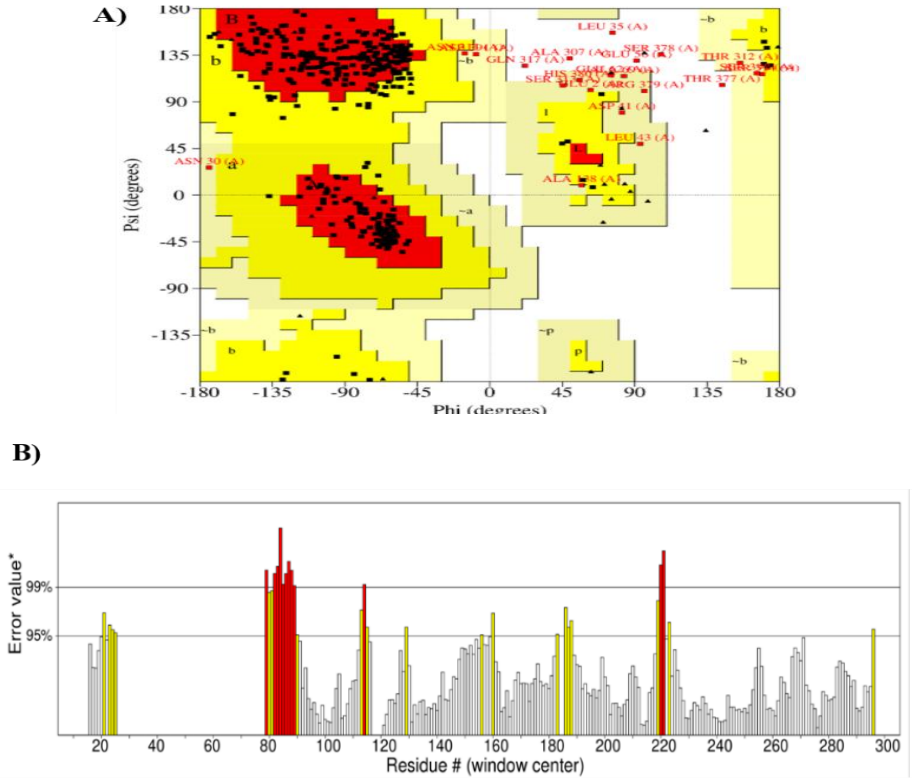

Figure 6. Validation of the predicted structure of TP53. **(A)** The Ramachandran plot is used to identify secondary structures in the TP53 protein. The Ramachandran plot's four quadrants are used to categorize amino acid residues according to the dihedral angles' (phi and psi) permitted and prohibited values. The amino acid residues with left-handed alpha-helical conformation were found in the first quadrant (Q1), those with beta-sheets were found in the second quadrant (Q2), and those with right-handed alpha-helices were found in the third quadrant. On the other hand, outliers in the disordered areas were found in the fourth quadrant. **B)** Quality estimate of TP53 by ERRAT. The x-axis refers to residue positions, and the y-axis shows the error value. The ERRAT server's Quality assessment of TP53 confirmed that the anticipated structure is correct.

score around 80% or higher suggested a well-predicted model, and TP53 attained an 86% score, indicating high accuracy. Reliable locations are typically indicated by error levels less than 95%, while problematic areas are suggested by values greater than 99%. Significant variations (red bars) are shown in some areas of this plot, especially those surrounding residues 70–90 and 220–240, which may indicate structural errors or poorly modeled areas. On the other hand, gray and yellow sections, respectively, denote places that are generally acceptable or fairly dependable. We may conclude that the model is dependable because a significant amount of protein is covered in grey and yellow regions, and the total quality factor is 86.40 (Figure 6B).

Better stereochemical precision was ensured by refining the predicted TP53 structure using the Galaxy web server. This analysis showed a large decrease in bad rotamers and an increase in Ramachandran-favored residues (up to 99%). The MolProbity and collision scores

Table 6. Refinement of the 3D structure of TP53 using Galaxy web server.

Model	GDT-HA	RMSD	MolProbity	Clash score	Poor rotamers	Rama favored
Initial	1.0000	0.000	1.793	1.0	2.6	83.6
MODEL 1	0.9109	0.608	1.307	5.7	0.3	98.7
MODEL 2	0.8957	0.650	1.337	6.1	0.6	99.0
MODEL 3	0.9065	0.632	1.275	5.2	0.0	98.7
MODEL 4	0.9008	0.623	1.240	4.7	0.3	98.5
MODEL 5	0.9052	0.639	1.416	7.6	0.9	98.5

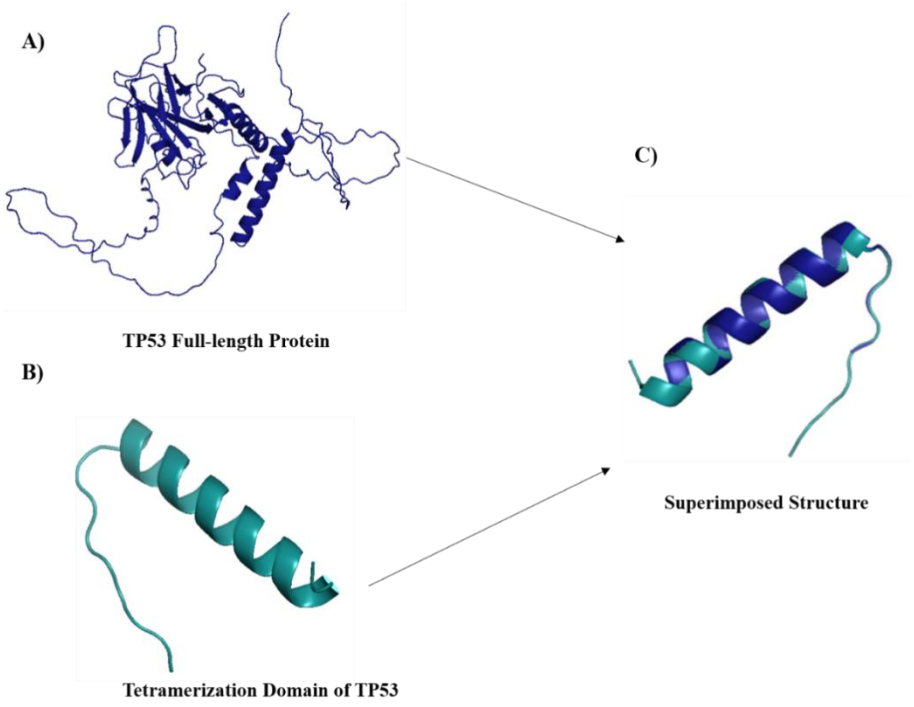

Figure 7. Illustration of structural homology of the predicted structure of TP53 (blue) by superimposing it with template 1AIE (deep teal). The common area depicts sequences shared by both proteins.

Increased slightly, suggesting small steric trade-offs, despite the RMSD values (0.608–0.650), suggesting considerable structural modifications. The improved models maintained their resemblance to the original structure, as seen by the GDT-HA values staying near 0.90. With its greatest Ramachandran favored percentage (99%) and balanced structural quality, MODEL 2 seems to be the best option overall (Table 6).

3.8 Structural Homology Assessment

To find out the structural similarities and differences between TP53 (the

Table 7. Prediction of subcellular localization of TP53 via DeepLoc.

Localization	Probability Score
Cytoplasm	0.3601
Nucleus	**0.909**
Extracellular	0.0452
Cell Membrane	0.1394
Mitochondrion	0.0802
Plastid	0.0038
Endoplasmic Reticulum	0.0539
Lysosome/Vacuole	0.0575
Golgi Apparatus	0.0401
Peroxisome	0.0037

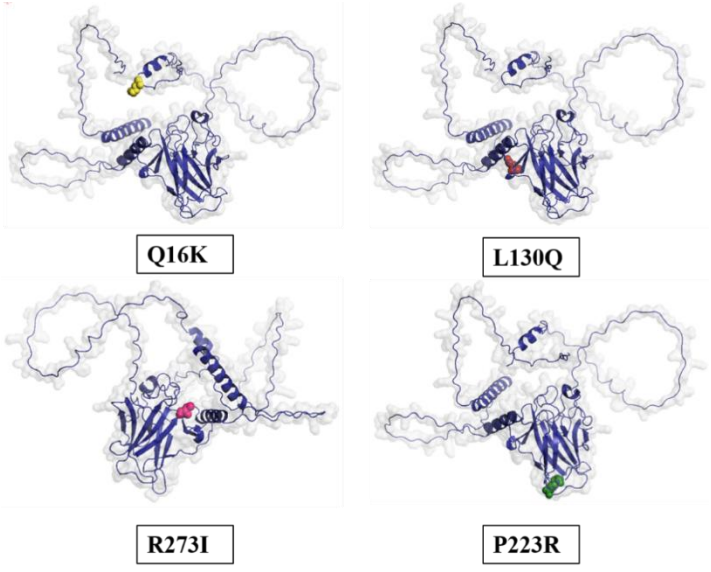

Figure 8. Mutagenesis induced in the selected variants of TP53.

predicted model) and 1AIE (the template), the 2 structures were visualized in PyMOL, and the structural homology between the 2 proteins was depicted by the superimposition of the model (blue) with the template (deep teal) (Figure 7). The superimposed areas depict the structural homology and thereby validate that the predicted structure is accurate.

3.9 Prediction of Subcellular Location

Various pathways and signals followed by all the possible subcellular compartments imply the probability or likelihood of the presence of the target protein in that compartment. The probability score for each possible location is shown in Table 7. The higher the score, the more likely a protein is present in that

Table 8. Nature of TP53 protein predicted by the Secretome server.

Name of Protein	NN-Score	Odds	Weighted
TP53	0.860	4.595	0.009

Table 9. Stability analysis of Q16K, L130Q, P223R, and R273I variants of TP53 using I-Mutant.

Position	Wild Type Residue	Mutant Residue	Stability	DDG	Reliability Index
16	Q	K	Decrease	-0.05	4
130	L	Q	Decrease	-1.45	9
223	P	R	Decrease	-1.51	8
273	R	I	Decrease	-0.22	8

Table 10. Stability analysis of Q16K, L130Q, P223R, and R273I variants of TP53 using MUPro

Position	Wild Type Residue	Mutant Residue	Stability	DDG
16	Q	K	Decreased	-0.58052438
130	L	Q	Decreased	-2.0673338
223	P	R	Decreased	-0.50987904
273	R	I	Increased	0.12806487

specific compartment. The highest score (0.909) observed in the case of the nucleus showed that TP53 is localized in the nucleus.

The nature of the protein (secretory or non-secretory) determined through the SecretomeP1.0 server is shown in Table 8. The first score is the neural network output score. For non-classically secreted proteins, the NN score should exceed the threshold of 0.6 (in the case of mammalian sequences) to indicate possible secretion. The 0.860 NN score for TP53 confirmed that it is a secretory protein.

3.10 In-situ Mutagenesis

The in situ mutagenesis was induced in wild-type TP53 at amino acid coordinates Q16K (rs2151047550), L130Q (rs2151033511), P223R (rs138983188), and R273I (rs121912660) via PYMOL (DeLano, 2002), and the structures were saved in PDB format (Figure 8).

3.11 Molecular Stability Analysis

To examine the effects of particular missense mutations (Q16K, L130Q, R273I, and P223R) on the structural stability of proteins, stability analysis was performed using I-Mutant2.0. All of the TP53 variations reduced stability as compared to the wild-type structure, according to I-Mutant v2.0 analysis. Variants Q16K, L130Q, R273I, and P223R were predicted to have free energy change (DDG) values of -0.05, -1.45, -1.51, and -0.22 Kcal/mol, respectively. The wild-type complex was destabilized following mutation, as indicated by the

Table 11. Stability and flexibility analysis of Q16K, L130Q, P223R, and R273I variants of TP53 using Dynamut.

Position	DDG (Kcal/mol)	Impact on Stability	DDS (Kcal/mol)	Impact on Flexibility
Q16K	0.020	Increased	-0.029	Decreased
L130Q	-1.513	Decreased	0.449	Increased
P223R	0.739	Increased	-1.070	Decreased
R273I	0.079	Increased	0.130	Increased

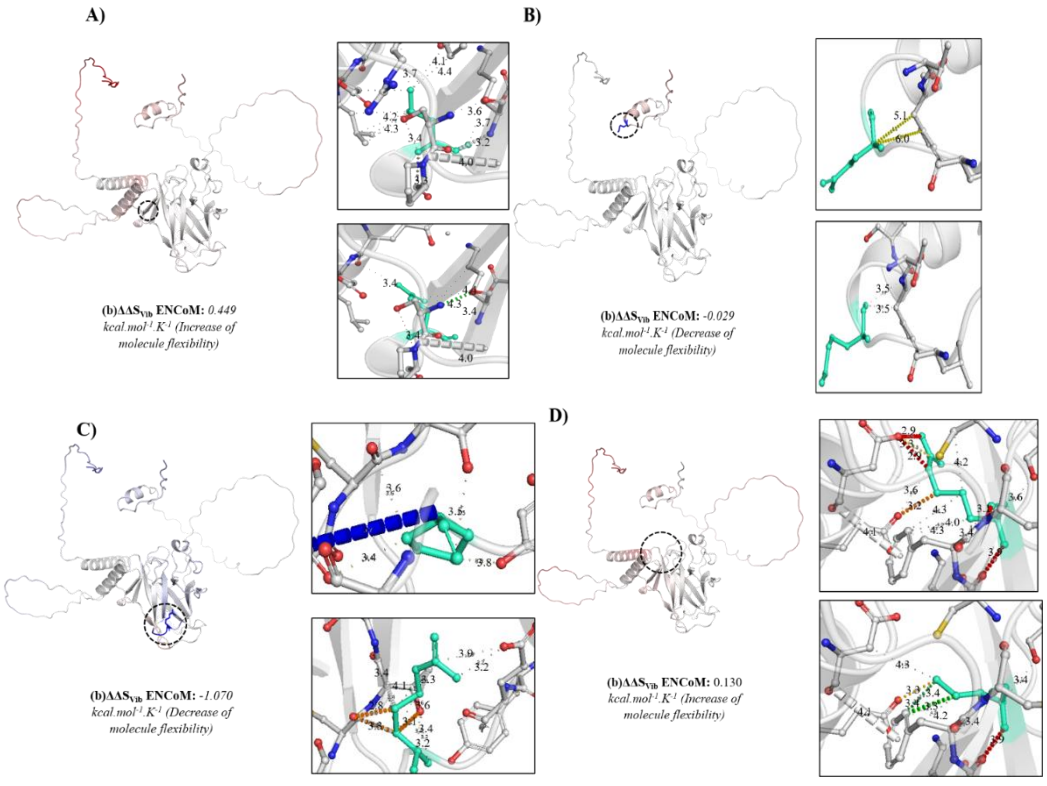

Figure 9. Flexibility analysis of (A) L130Q, (B) Q16K, (C) P223R, and (D) R2731 using Dynamut.

DDG value for each variant being less than 0 (Table 9).

However, MUPro analysis revealed that all of the TP53 variations reduced stability as compared to the wild-type structure, except R273I. Variants Q16K, L130Q, and R273I had DDG values of -0.58052438, -2.0673338, and 0.50987904Kcal/mol, respectively, which indicates that the wild-type complex was destabilized following mutation, as indicated by the DDG value being less than 0 (Table 10).

3.12 Molecular Flexibility Analysis

Additionally, Dynamut evaluated the impact of missense variants on the flexibility and stability of protein structure using vibrational entropy change (DDS) and DDG, respectively. Except for L130Q, every version had a stabilizing effect. Furthermore, protein flexibility was increased by L130Q and R273I and decreased by Q16K and P223 (Table 11 and Figure 9).

3.13 Gene Ontology Analysis

3.13.1 Biological Process Predictions

TP53 is associated with the regulation of metabolic processes, gene expression, RNA processing, and transcription (with statistical confidence exceeding 0.7). These associations underscore TP53's essential function in maintaining cellular equilibrium, directing transcriptional programs, and coordinating biosynthetic processes.

Table 12. Biological processes are summarized in the given table.

GO Term	Name	Prob	SVM Reliability
GO:0019222	regulation of metabolic process	0.943	H
GO:0010468	regulation of gene expression	0.908	H
GO:0034645	cellular macromolecule biosynthetic process	0.880	H
GO:0008380	RNA splicing	0.870	H
GO:2001141	regulation of the RNA biosynthetic process	0.862	H
GO:1903506	regulation of nucleic acid-templated transcription	0.834	H
GO:0051171	regulation of nitrogen compound metabolic process	0.822	H
GO:0009059	macromolecule biosynthetic process	0.769	H
GO:0051252	regulation of the RNA metabolic process	0.763	H
GO:0006355	regulation of transcription, DNA-templated	0.761	H
GO:0006397	mRNA processing	0.742	H
GO:0006351	transcription, DNA-templated	0.737	H
GO:0010629	negative regulation of gene expression	0.701	H
GO:0000375	RNA splicing, via transesterification reactions	0.670	H
GO:0006810	transport	0.647	H
GO:0000398	mRNA splicing, via the spliceosome	0.612	H
GO:0006396	RNA processing	0.587	H
GO:0006357	regulation of transcription from the RNA polymerase II promoter	0.584	H
GO:0009890	negative regulation of biosynthetic process	0.545	H
GO:0006366	transcription from the RNA polymerase II promoter	0.543	H
GO:0031328	positive regulation of cellular biosynthetic process	0.505	H
GO:0002376	immune system process	0.504	H

Table 13. TP53 molecular function predictions as a transcriptional regulator are summarized in the table.

GO Term	Name	Prob	SVM Reliability
GO:0003676	nucleic acid binding	0.967	H
GO:0000166	nucleotide binding	0.922	H
GO:0030554	adenyl nucleotide binding	0.906	H
GO:0001228	RNA polymerase II transcription regulatory region sequence-specific DNA binding transcription factor activity involved in positive regulation of transcription	0.889	H
GO:0003677	DNA binding	0.868	H
GO:0046914	transition metal ion binding	0.795	H
GO:0003723	RNA binding	0.727	H

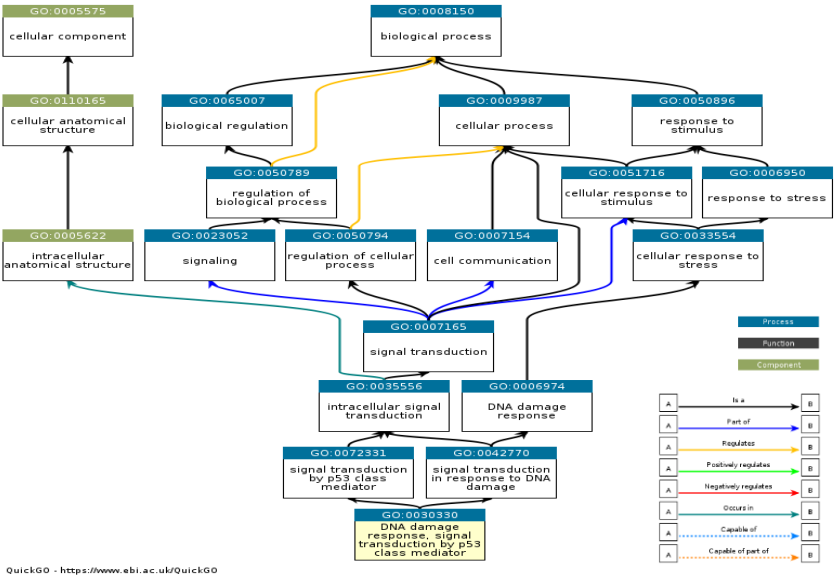

Figure 10. Blue boxes indicate Biological Processes of Tp53, Green boxes indicate Cellular components of Tp53

3.13.2 Molecular Function Predictions

TP53 exhibits associations with nucleic acid interaction, transcription factor activity, and RNA binding (probabilities surpassing 0.8), solidifying its identity as a transcriptional regulator. These capabilities enable TP53 to directly engage with DNA/RNA, influencing gene activation and safeguarding genomic integrity.

3.13.3 Cellular Component Predictions

TP53 localizes primarily within nuclear substructures, notably the nucleolus (0.819) and nuclear bodies (0.547), which are critical hubs for transcriptional control and stress-responsive signaling. This spatial distribution aligns with its role in mediating DNA damage responses and modulating transcriptional networks.

3.13.4 Ancestor Chart

TP53 governs diverse biological mechanisms, including cellular regulation and responses to environmental or internal stimuli. It is a central player in signal transduction pathways, particularly those involving intracellular communication and DNA damage recognition. TP53 predominantly also operates within subcellular compartments, particularly nuclear structures such as the nucleolus and nuclear bodies. The functions are summarized in the table. The hierarchical organization of Gene Ontology (GO) terms associated with TP53 is represented by the given chart. (https://www.ebi.ac.uk

Table 14. Cellular component predictions are given in the table.

GO Term	Name	Prob	SVM Reliability
GO:0005730	nucleolus	0.819	H
GO:0016604	nuclear body	0.547	H

(Cozzetto, Minneci, Currant, & Jones, 2016)

Table 15. Selection of the best inhibitor for protein based on physicochemical properties of compounds

Sr. No.	pdbqt	Compounds	Molecular Weight (g/mol)	HBD	HBA	logP	nRot	RO5 (Violations)
1	74334923	COTI-2	366.5	1	3	2.84	4	0
2	322968	PRIMA1	185.22	2	4	1.51	2	0

/QuickGO/GTerm?id=GO:0030330#term=history)

3.14 Virtual Screening of Best Inhibitors

The compounds' structures were obtained from PubChem and virtually screened according to their physicochemical characteristics. The COTI-2 and PRIMA1 compounds for targeted inhibition of TP53 were chosen; further information is available in **supplementary files.** The chosen chemicals underwent a pharmacokinetics analysis. **Table 15** lists the targeted proteins' chosen inhibitors. Both the

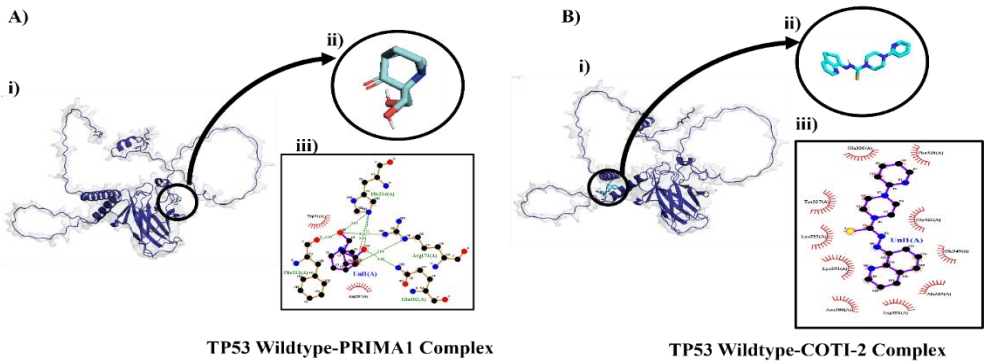

Figure 11. Molecular Docking Analysis. **(A)** Wild-type TP53-PRIMA1 Docked Complex. **(i)** The 3D structure of molecular docking. **(ii)** The 3D structure of ligand (PRIMA1) docked with protein. **(iii)** The 2D residue-wise interaction between ligand and protein. **(B)** Wild-type TP53-COTI2 Docked Complex. **(i)** The 3D structure of molecular docking. **(ii)** The 3D structure of ligand (COTI2) docked with protein. **(iii)** The 2D residue-wise interaction between ligand and protein.

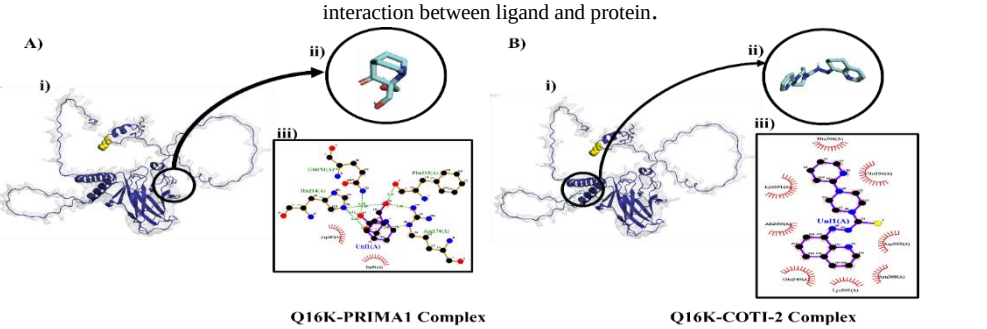

Figure 12. Molecular Docking Analysis. **(A)** Q16K variant-PRIMA1 Docked Complex. **(i)** The 3D structure of molecular docking. **(ii)** The 3D structure of ligand (PRIMA1) docked with protein. **(iii)** The 2D residue-wise interaction between ligand and protein. **(B)** Q16K mutant TP53-COTI2 Docked Complex. **(i)** The 3D structure of molecular docking. **(ii)** The 3D structure of ligand (COTI2) docked with protein. **(iii)** The 2D residue-wise interaction between ligand and protein

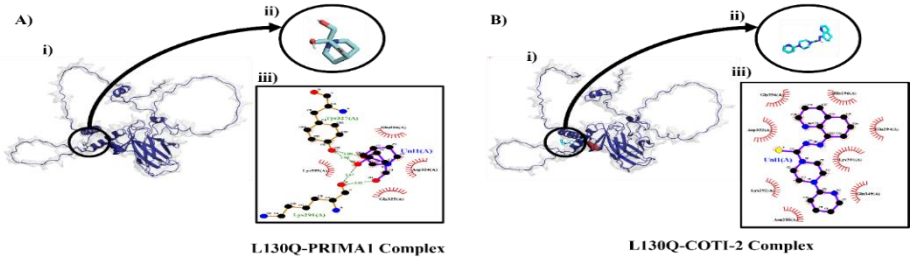

Figure 13. Molecular Docking Analysis. **(A)** L130Q variant-PRIMA1 Docked Complex. **(i)** The 3D structure of molecular docking. **(ii)** The 3D structure of ligand (PRIMA1) docked with protein. **(iii)** The 2D residue-wise interaction between ligand and protein. **(B)** L130Q mutant TP53-COTI2 Docked Complex. **(i)** The 3D structure of molecular docking. **(ii)** The 3D structure of ligand (COTI2) docked with protein. **(iii)** The 2D residue-wise interaction between ligand and protein

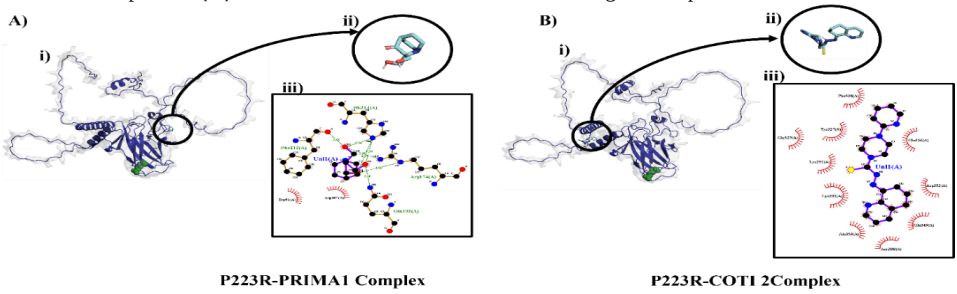

Figure 14. Molecular Docking Analysis. **(A)** P223R variant-PRIMA1 Docked Complex. **(i)** The 3D structure of molecular docking. (**ii**) The 3D structure of ligand (PRIMA1) docked with protein. **(iii)** The 2D residue-wise interaction between ligand and protein. **(B)** P223R mutant TP53-COTI2 Docked Complex. **(i)** The 3D structure of molecular docking. **(ii)** The 3D structure of ligand (COTI2) docked with protein. **(iii)** The 2D residue-wise interaction between ligand and protein

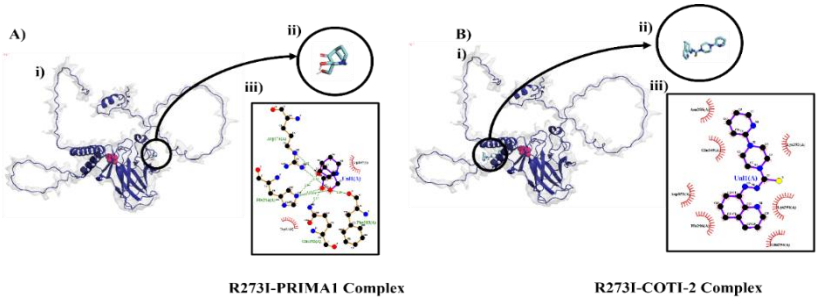

Figure 15. Molecular Docking Analysis. **(A)** R273I variant-PRIMA1 Docked Complex. **(i)** The 3D structure of molecular docking. (**ii**) The 3D structure of ligand (PRIMA1) docked with protein. **(iii)** The 2D residue-wise interaction between ligand and protein. **(B)** R273I mutant TP53-COTI2 Docked Complex. **(i)** The 3D structure of molecular docking. **(ii)** The 3D structure of ligand (COTI2) docked with protein. **(iii)** The 2D residue-wise interaction between ligand and protein

compounds showed 0 Lipinski's rule of violation.

3.15 Molecular Docking

CB Dock2 was used to perform protein-ligand docking, and the 3D structure of the docked complex and the interactions between the docked molecules, residue by residue, were then shown using DiscoveryStudio. Following docking, the model with the lowest Vina

score value was selected as the best model (Table 16).

Figure 11-15 shows the 3D and 2D interaction of wild type TP53 and mutant TP53 (Q16K, L130Q, P223R, and R273I) with PRIMA1 and COTI2.

The type of interactions between the protein and ligand is summarized in Table 17.

4. Discussion

The most prevalent disease in women worldwide is breast cancer (BC) (Siegel et al., 2018), which is caused by risk factors like genetic abnormalities that trigger many cancer hallmarks (Lukong, 2017). 20% of patients have a family history of BC, according to statistical research, and 5–10% have hereditary BCs, which are brought on by germline mutations in tumor suppressor genes such as TP53 (Economopoulou et al., 2015). To find genetic variants that lead to cancer, computational biology technologies are being applied. These findings align with the studies of Andrew C.R.Martin, Angelo M.Facchiano, et al. about the Integration of mutation data and structural analysis of the TP53 tumor-suppressor protein(Martin et al., 2002). An important part of the prognosis of the disease may be the in-silico identification of SNPs and investigation of their effects on protein dynamics and stability. TP53 mutations are often seen in clinically aggressive cancers. One potential therapeutic strategy for p53 mutations is to inhibit TP53 mutations and restore mutant p53 function (Liu et al., 2019). A pathogenicity threshold of 80% or above was applied to the TP53 missense variations that were obtained from ENSEMBL to filter out the 25 most harmful SNPs that were predicted by the majority of SNP tools, including SIFT, PolyPhen, CADD, MetaLR, and MutationAssessor. Of these twenty-five variations, four variants Q16K, L130Q, P223R, and R273I were selected for additional examination. Numerous studies have examined the impact of mutations in tumor suppressor genes and proto-oncogenes to ascertain the overall impact on the structure, function, flexibility, and interaction patterns of these proteins in patients with breast cancer (Deng, Zhou, Fan, & Yuan, 2017; Lilyquist, Ruddy, Vachon, & Couch, 2018). The domain

Table 17. Types of Interactions between Ligand-Protein Complexes.

Protein	Ligand	Hydrogen Bonds	Hydrophobic Interactions
Wild Type TP53	PRIMA1	7	2
	COTI-2	0	10
Q16K	PRIMA1	7	2
	COTI2	0	8
L130Q	PRIMA1	4	4
	COTI2	0	8
P223R	PRIMA1	7	2
	COTI2	0	10
R273I	PRIMA1	7	2
	COTI2	0	7

analysis showed that L130Q, P223R, and R273I are located in the core DNA-binding domain of TP53, while the Q16K variation is located in the TAD domain. Our findings aligned with the results of Young et al.'s domain study of TP53. This study identifies TP53 mutations, particularly in DNA-binding domains (e.g., His158, Ser245), as independent predictors of poor overall survival in DLBCL patients, with Loop-L2 mutations showing no impact, and highlights their prognostic stratification in germinal center B-cell subtypes, validated alongside the International Prognostic Index (Young et al., 2008). The secondary structure prediction was done through PSIPRED to identify the structural expressions linked to cancer mutations and find functional domains. The DNA-binding domain of TP53 (residues 102–292) relies on a beta-sandwich scaffold and alpha-helical motifs to recognize specific DNA sequences. Any disruption in these structures can weaken TP53's ability to activate genes that suppress tumors. These alpha-helices and beta-sheets are essential for TP53's role as a transcription factor (GO:0003700), helping it regulate important genes like CDKN1A (p21) and BAX. Our findings align with research by Joerger and Fersht, who demonstrated that TP53's ability to regulate gene expression and to bind DNA could be disrupted due to the structural instability in the beta-sandwich domain. Also, cancer development often involves compromised p53 tumor suppressor function through genetic or regulatory disruptions, driving therapeutic innovations like structural correction agents for mutant p53 and MDM2/MDMX antagonists for cancers retaining functional p53, with these approaches now in clinical development and highlighting the pathway's evolutionary conservation while advancing personalized oncology(Joerger & Fersht, 2007). Following AlphaFold's 3D structure prediction of TP53, ERRAT and the Ramachandran plot were used to confirm it. The accuracy of the protein structure was confirmed by an overall quality score of 98.1 and 86.40 by the Ramachandran plot and errat. Our findings are consistent with earlier research that found that over 99 percent of the residues were found in the quadrants that correspond to stable secondary structures (Kasilingam & Elengoe, 2018).

To further refine the criteria, evolutionary conservation of affected residues was assessed; highly conserved sites were assumed to be more likely to be functionally important. Protein stability changes following mutation were evaluated using the available prediction techniques, and variants anticipated to severely destabilise the TP53 protein were given priority. Furthermore, variants were cross-referenced with the ClinVar and dbSNP databases to include clinical significance comments, and known benign polymorphisms were eliminated from the dataset. Where allele frequency information was provided, frequent variants (minor allele frequency > 0.01) were removed to focus on rare, potentially disease-associated mutations. Our multi-step integrative approach ensured that only high-confidence detrimental TP53 SNPs were selected for further structural and functional analyses. Since Q16K's unique location in the N-terminal transactivation domain, where somatic TP53 mutations are uncommon in patient samples, its functional influence is more likely to be caused by altered protein turnover or disrupted co-activator interactions rather than direct interference with DNA binding. By narrowing the gap between well-defined hotspot biology and less-defined mutation positions, these four variants strengthen the findings' translational significance and broaden the analytical focus of this study beyond the DNA-

binding domain, which has predominated previous TP53 structural research.

Considering their well-known and mechanistically significant functions in restoring p53 activity, COTI-2 and PRIMA-1 were identified as possible therapeutic targets. This selection is consistent with the functional impact of the TP53 mutations studied in this work. PRIMA-1 and its methylated derivative APR-246 are tiny compounds that have been extensively investigated due to their unusual ability to refold mutant p53 into a conformation comparable to wild-type p53. This step restores sequence-specific DNA-binding activity and activates apoptotic pathways that rely on p53. It is the gold standard for mutant p53 reactivation approaches because it is successful across a wide range of tumour types and TP53 mutations. Because of its dual action mechanism—reactivating mutant p53 and blocking important carcinogenic signalling pathways like AMPK regulation and PI3K/AKT/mTOR—COTI-2 was selected. COTI-2 has demonstrated anti-proliferative and pro-apoptotic effects in preclinical cancer models, including those resistant to conventional therapy, and it has demonstrated efficacy against a wider range of TP53 mutations than previous p53-targeting medications. Its ability to specifically target tumour cells while avoiding healthy cells is another therapeutic advantage [40]. We can assess the therapeutic restoration of TP53 function over a broader spectrum of detrimental mutations, both in terms of structure and function, by combining PRIMA-1 and COTI-2, two mutant p53-reactivating agents with distinct but complementary methods.

It is crucial to recognise the inherent limits of purely in silico techniques, even while the molecular docking and molecular dynamics simulation results offer insightful information about the binding affinity, stability, and interaction patterns of the chosen drugs with mutant TP53. The quality of the structural models, force fields, and scoring functions used in computational forecasts may not adequately represent the dynamic complexity of biological systems under physiological settings. Furthermore, docking algorithms offer an estimate of binding poses and energies that might not necessarily correspond with functional biological activity or actual binding affinities. In a similar vein, molecular dynamics simulations are constrained by simulation time scales and might not capture rare event dynamics or long-term conformational changes. Therefore, experimental validation through in vitro and in vivo research is necessary to demonstrate their therapeutic significance, even though the current findings provide a solid theoretical foundation for the potential efficacy of COTI-2 and PRIMA-1 against harmful TP53 mutations.

The detected harmful TP53 SNPs were compared with clinically reported TP53 mutations in breast cancer patients recorded in public variant databases and prior literature to increase the findings' translational applicability. The DNA-binding domain, which is known to contain a significant percentage of pathogenic variants linked to loss of tumour suppressor function, is one of the hotspot regions of TP53 that are commonly reported in breast cancer. Several of the high-confidence mutations found in this study correspond to these regions. However, in breast cancer cohorts, mutations at conserved residues within this domain have been linked to poor clinical outcomes, increased genomic instability, and decreased transcriptional activity. This overlap implies that the chosen SNPs may reflect functionally significant mutations contributing to the

pathophysiology of breast cancer and validates the clinical significance of the computationally prioritised variations. A portion of the discovered variations, however, have little to no direct clinical annotation in breast cancer databases, suggesting that they may be new or poorly characterised possibilities that need more research.

Because the work is solely based on in silico analysis without experimental confirmation, the therapeutic implications of the current findings should be regarded cautiously. Although favorable binding affinity and stable interactions of COTI-2 and PRIMA-1 with specific harmful TP53 mutations are suggested by the docking and molecular dynamics data, these findings are prediction computational results rather than verified biological impacts. As a result, any conclusions about direct therapeutic potential or clinical efficacy are yet conjectural. The findings mainly offer a theoretical framework for ranking potential drugs and locating structurally significant TP53 alterations that might react to reactivation techniques. To validate these anticipated interactions and ascertain their actual therapeutic significance in a biological setting, experimental research is necessary, including in vitro functional tests and in vivo validation models.

5. Conclusion

This study focused on deleterious SNPs' effect on the functioning of TP53. It includes the protein's evolutionary data and phylogenetic analysis. The AlphaFold predicted tertiary structure was validated and refined to perform further analysis. TP53 is localized in the nucleus and is secretory in nature, which supports its role in DNA damage response and transcriptional regulation. To study the impact of mutation on TP53's stability and functioning, in-situ mutagenesis was performed on TP53 at coordinates Q16K, L130Q, P223R, and R273I. Furthermore, stability analysis revealed that most of the variations result in reduced stability of the protein. GO analysis revealed that TP53's biological roles include regulating metabolism, gene expression, RNA processing, and transcription with high confidence. Functionally, it interacts with nucleic acids, acts as a transcription factor, and binds RNA (probability >0.8). For virtual screening, COTI-2 and PRIMA1 were identified as potential TP53 inhibitors based on pharmacokinetics and Lipinski's rule compliance. The molecular docking analysis of wild-type and mutated TP53 was carried out to point out the differences in the interaction pattern of the mutated protein with COTI-2 and PRIMA1 as compared to wild-type TP53.

Additional Information and Declaration

Funding

The authors received no funding for this work.

Competing Interests

The authors declare there are no competing interests.

Data Availability

The following information was supplied regarding data availability:
Raw data are available in the Supplementary Files.

References

Adzhubei, I., Jordan, D. M., & Sunyaev, S. R. (2013). Predicting functional effect of human missense mutations using PolyPhen-2. *Current protocols in human genetics*, *76*(1), 7-20.

Ahmad, H., Ali, A., Ali, R., Khalil, A. T., Khan, I., Khan, M. M., & Alorini, M. (2023). Mutational landscape and in-silico analysis of TP53, PIK3CA, and PTEN in patients with breast cancer from khyber Pakhtunkhwa. *ACS omega*, *8*(45), 43318-43331.

Bai, X., Ni, J., Beretov, J., Graham, P., & Li, Y. (2021). Triple-negative breast cancer therapeutic resistance: Where is the Achilles' heel? *Cancer letters*, *497*, 100-111.

Bykov, V. J. N., Eriksson, S. E., Bianchi, J., & Wiman, K. G. (2018). Targeting mutant p53 for efficient cancer therapy. *Nature Reviews Cancer*, *18*(2), 89-102.

Cheng, J. n., Ding, X., Xu, S., Zhu, B., & Jia, Q. (2020). Gene expression profiling identified TP53MutPIK3CAWild as a potential biomarker for patients with triple-negative breast cancer treated with immune checkpoint inhibitors. *Oncology letters*, *19*(4), 2817-2824.

Cozzetto, D., Minneci, F., Currant, H., & Jones, D. T. (2016). FFPred 3: feature-based function prediction for all Gene Ontology domains. *Scientific reports*, *6*(1), 31865.

DeLano, W. L. (2002). Pymol: An open-source molecular graphics tool. *J CCP4 Newsl. Protein Crystallogr*, *40*(1), 82-92.

Deng, N. A., Zhou, H., Fan, H., & Yuan, Y. (2017). Single nucleotide polymorphisms and cancer susceptibility. *Oncotarget*, *8*(66), 110635.

Economopoulou, P., Dimitriadis, G., & Psyrri, A. (2015). Beyond BRCA: new hereditary breast cancer susceptibility genes. *Cancer treatment reviews*, *41*(1), 1-8.

Emadi, E., Akhoundi, F., Kalantar, S. M., & Emadi-Baygi, M. (2020). Predicting the most deleterious missense nsSNPs of the protein isoforms of the human HLA-G gene and in silico evaluation of their structural and functional consequences. *BMC genetics*, *21*, 1-27.

Joerger, A., & Fersht, A. R. (2007). Structure–function–rescue: the diverse nature of common p53 cancer mutants. *Oncogene*, *26*(15), 2226-2242.

Jones, D. T. (1999). Protein secondary structure prediction based on position-specific scoring matrices. *Journal of molecular biology*, *292*(2), 195-202.

Kasilingam, T., & Elengoe, A. (2018). In silico molecular modeling and docking of apigenin against the lung cancer cell proteins. *Asian J. Pharm. Clin. Res*, *11*(9), 246-252.

Khan, K., Shah, H., Rehman, A., Badshah, Y., Ashraf, N. M., & Shabbir, M. (2022). Influence of PRKCE non-synonymous variants on protein dynamics and functionality. *Human Molecular Genetics*, *31*(13), 2236-2261.

Li, X., Chen, X., Wen, L., Wang, Y., Chen, B., Xue, Y., . . . Liao, N. (2020). Impact of TP53 mutations in breast cancer: Clinicopathological features and prognosisImpact of TP53 mutations in breast CA. *Thoracic Cancer*, *11*(7), 1861-1868.

Lilyquist, J., Ruddy, K. J., Vachon, C. M., & Couch, F. J. (2018). Common genetic variation and breast cancer risk—past, present, and future. *Cancer Epidemiology, Biomarkers & Prevention*, *27*(4), 380-394.

Liu, Y., Wang, X., Wang, G., Yang, Y., Yuan, Y., & Ouyang, L. (2019). The past, present and future of potential small-molecule drugs targeting p53-MDM2/MDMX for cancer therapy. *European journal of medicinal chemistry*, *176*, 92-104.

Lu, T., Zou, Y., Xu, G., Potter, J. A., Taylor, G. L., Duan, Q., . . . Ye, D. (2016). PRIMA-1Met suppresses colorectal cancer independent of p53 by targeting MEK. *Oncotarget*, *7*(50), 83017.

Lukong, K. E. (2017). Understanding breast cancer–The long and winding road. *BBA clinical*, *7*, 64-77.

Lundberg, P. C., & Phoosuwan, N. (2022). Life situations of Swedish women after mastectomy due to breast cancer: A

qualitative study. *European Journal of Oncology Nursing, 57*, 102116.

Martin, A. C. R., Facchiano, A. M., Cuff, A. L., Hernandez-Boussard, T., Olivier, M., Hainaut, P., & Thornton, J. M. (2002). Integrating mutation data and structural analysis of the TP53 tumor-suppressor protein. *Human mutation, 19*(2), 149-164.

Meric-Bernstam, F., Zheng, X., Shariati, M., Damodaran, S., Wathoo, C., Brusco, L., . . . Basho, R. K. (2018). Survival outcomes by TP53 mutation status in metastatic breast cancer. *JCO precision oncology, 2*, 1-15.

Mooney, S. (2005). Bioinformatics approaches and resources for single nucleotide polymorphism functional analysis. *Briefings in bioinformatics, 6*(1), 44-56.

Nounou, M. I., ElAmrawy, F., Ahmed, N., Abdelraouf, K., Goda, S., & Syed-Sha-Qhattal, H. (2015). Breast cancer: conventional diagnosis and treatment modalities and recent patents and technologies. *Breast cancer: basic and clinical research, 9*, BCBCR-S29420.

O'Connor, P. M., Jackman, J., Bae, I., Myers, T. G., Fan, S., Mutoh, M., . . . Weinstein, J. N. (1997). Characterization of the p53 tumor suppressor pathway in cell lines of the National Cancer Institute anticancer drug screen and correlations with the growth-inhibitory potency of 123 anticancer agents. *Cancer research, 57*(19), 4285-4300.

Pollock, N. C., Ramroop, J. R., Hampel, H., Troester, M. A., Conway, K., Hu, J. J., . . . Ziv, E. (2022). Differences in somatic TP53 mutation type in breast tumors by race and receptor status. *Breast cancer research and treatment, 192*(3), 639-648.

Rentzsch, P., Witten, D., Cooper, G. M., Shendure, J., & Kircher, M. (2019). CADD: predicting the deleteriousness of variants throughout the human genome. *Nucleic acids research, 47*(D1), D886-D894.

Reva, B., Antipin, Y., & Sander, C. (2011). Predicting the functional impact of protein mutations: application to cancer genomics. *Nucleic acids research, 39*(17), e118-e118.

Selga, C., Koc, A., Chawade, A., & Ortiz, R. (2020). A bioinformatics pipeline to identify a subset of SNPs for genomics-assisted potato breeding. *Plants, 10*(1), 30.

Siegel, R. L., Miller, K. D., & Jemal, A. (2018). Cancer statistics, 2018. *CA: a cancer journal for clinicians, 68*(1), 7-30.

Sim, N.-L., Kumar, P., Hu, J., Henikoff, S., Schneider, G., & Ng, P. C. (2012). SIFT web server: predicting effects of amino acid substitutions on proteins. *Nucleic acids research, 40*(W1), W452-W457.

Singh, A. K., Olsen, M. F., Lavik, L. A. S., Vold, T., Drabløs, F., & Sjursen, W. (2021). Detecting copy number variation in next generation sequencing data from diagnostic gene panels. *BMC Medical Genomics, 14*(1), 214.

Sohail, S., & Alam, S. N. (2007). Breast cancer in Pakistan-awareness and early detection.

Wang, H., Guo, M., Wei, H., & Chen, Y. (2023). Targeting p53 pathways: Mechanisms, structures and advances in therapy. *Signal transduction and targeted therapy, 8*(1), 92.

Young, K. H., Leroy, K., Møller, M. B., Colleoni, G. W. B., Sánchez-Beato, M., Kerbauy, F. R., . . . Gaulard, P. (2008). Structural profiles of TP53 gene mutations predict clinical outcome in diffuse large B-cell lymphoma: an international collaborative study. *Blood, The Journal of the American Society of Hematology, 112*(8), 3088-3098.

Zhou, X., Hao, Q., & Lu, H. (2019). Mutant p53 in cancer therapy—the barrier or the path. *Journal of molecular cell biology, 11*(4), 293-305.

UCP Journal of Science and Technology
Vol. 3, Issue 2 (January - June 2026)
Journal website: http://ojs.ucp.edu.pk/index.php/ucpjst/index

Valorization of Date Pits into a Functional Coffee Alternative: Compositional, Antioxidant, and Sensory Evaluation

Hiba Naveed[1], Kanza Aziz Awan[1], Zahid Bashir[1*], Waleed Sultan[1], Ahmad Faraz[1], Momina Noor[1], Arzoo Fatima[1]

Abstract

Functional foods, which provide health benefits beyond basic nutrition, have historical roots in ancient dietary traditions. Thus, the incorporation of functional foods into daily diets helps in promoting health and well-being. In this regard, date fruit pits emphasize the unexploited byproduct with significant functional and nutritional properties. Pakistan faces substantial post-harvest losses. Date fruit pits are often wasted despite their nutritional and bioactive moieties. This research explores date pits as a sustainable coffee substitute while minimizing food waste. Three formulations were analyzed: (T_0) 100% black coffee, (T_1) 100% date pit coffee, and (T_2) 70% black coffee and 30% date pit coffee blend. Results show that T_0 had the highest ash content (3.99±0.01), and T_2 had the highest pH (9.11±0.03) and moisture content (8.84±0.01). Date pit coffee proposes acceptable sensory attributes, a strong antioxidant profile, low calorie content, and distinguishable health and environmental sustainability benefits. These outcomes uphold its potential as an eco-friendly, functional, caffeine-free coffee substitute, an imperative need for waste reduction and elevating sustainable food system practices.

Keywords: Functional Food, Date Pits, Waste Reduction, Caffeine-Free, Antioxidants.

1. Introduction

Approximately 8 million tons of date fruit are globally produced each year. Normally, the seeds of the fruit account for about 10-15% of the fruit's weight and are often discarded as waste. Date pit coffee is an eco-friendly solution for the functional food industry that substitutes conventional coffee with a caffeine-free version. An increase in demand for both functional and sustainable food supply has resulted in the boom of coffee substitutes with new health and environmental advantages (Awan, Yaqoob, et al., 2025; Naveed et al., 2024). Traditional coffee manufacturing is resource-consuming, with high water usage and environmental effects linked with widespread cultivation. Coffee drinking has spread globally, with huge demand for alternatives with health benefits that tackle issues of sustainability (Samoggia & Riedel, 2019). Within these options, date pit coffee has been validated to be a sustainable alternative as a result of its functional potential and environmental advantages. Date pits, a secondary product of the date fruit, are generally discarded, contributing to agricultural waste (Munir et al., 2024).

The health-promoting effects are attributed to the nutritional content of date pits and other minerals like potassium and

[1]Department of Food and Nutritional Sciences, Faculty of Science and Technology, University of Central Punjab,
[*]Corresponding author's E-mail: zbsdk26@gmail.com
Received: 23 October 2025; Received in revised form: 26 April 2026; Accepted: 15 May 2026.
Available online: 13 July 2026.

DOI: https://doi.org/10.24312/ucp-jst.03.02.715

magnesium (Attia et al., 2021). Phenolic compounds, flavonoids, and other antioxidants found in date pits have been reported to have potential restorative, anti-inflammatory, and antioxidant properties, paralleling some of the benefits traditionally associated with coffee consumption (Awan, 2017; Awan, Butt, et al., 2025). Additionally, date pit coffee is caffeine-free, making it suitable for individuals sensitive to caffeine or those seeking alternatives without the stimulant effects (Awan, Butt, Sharif, & Hussain, 2018). Although coffee is common worldwide, overconsumption of caffeine poses serious health risks, such as heart disease, stomach ulcers, and a negative impact on the nervous system. The major research gaps exist in the development and quality assessment of coffee substitutes made from date pits. Although date pits are nutritious, little research has been done on how they can be converted into a coffee substitute, particularly in terms of sensory attributes such as taste, aroma, and mouthfeel. Furthermore, there is a considerable lack of comprehensive hedonic response and consumer acceptability studies, which is crucial to understand the market potential of such products among several population subgroups (Mahmud, Shellie, & Keast, 2020). Additionally, the optimal processing parameters, including roasting, grinding, and brewing methods that would best replicate the flavor profile of traditional coffee, remain insufficiently explored and optimized. While the functional benefits of date pits, like their antioxidant assay and dietary fiber content, have been identified, their specific health impacts when consumed as a beverage have yet to be clinically validated. Safety aspects such as the presence of anti-nutritional factors, contaminants, or microbial risks following processing have also not been properly investigated (Tahmouzi et al., 2024). However, limited studies have been carried out on the roasted date pit product shelf life and storage stability, which raises questions regarding their quality maintenance over time. Closing these gaps is essential for proper development, quality control, and commercialization of date-pit coffee products.

Although coffee is popular worldwide, excessive consumption of caffeine is associated with serious health issues that include arrhythmias, cardiovascular disease, and diabetes. Coffee has furan as a constituent, which at high levels can be carcinogenic or tumorigenic (Zawirska-Wojtasiak et al., 2018). In addition, coffee can suppress gastric acid secretion and lead to gastrointestinal upsets. In conclusion, coffee substitute consumption is a possible measure to prevent the mentioned health impacts. Date pit coffee is certainly a possible substitute (Diaz-Rojas et al., 2019).

This study aims to determine the quality and development of coffee extracted from date pits by examining its physicochemical properties, nutritional value, and sensory panel. Through an extensive quality evaluation, this study hopes to contribute to the larger research domain of sustainable food innovation by proving date pit coffee as a sustainable alternative. Using date pit coffee as a recycling of agricultural waste fits the current trend of implementing sustainable actions and incorporating healthy items into a healthy food system. The study will add to the research on the use of date pits as evidence of the thinking on the conversion of farming waste into useful foods.

2. Materials and Methods

This investigation was performed in the Postgraduate Research Laboratory within the Department of Food and Nutritional Sciences, Faculty of Science and Technology at the University of Central Punjab (UCP), Lahore, and the Pakistan Council of Scientific and Industrial Research (PCSIR), Lahore. Focusing on the preparation and quality

analysis of date pit-based coffee. Multiple treatments were devised for the development of date pit coffee as a substitute for traditional coffee. The detailed methodology and procedures are outlined below, as shown in Figure 1.

2.1 Raw Materials

The date pits were procured from the local food points. For comparison, the black coffee of Nestle was bought from the local market of Johar Town, Lahore.

2.2 Chemicals

All chemicals and reagents used in this study were of analytical grade and obtained from Sigma-Aldrich, USA.

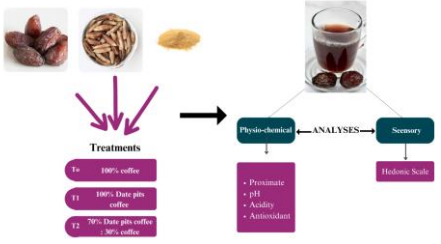

Figure 1. Methodological framework for the valorization of date pits into a functional coffee alternative.

2.3 Development of Date Pit Coffee

The date pits were first rinsed with clean water to remove any dirt or debris. After rinsing, the date pits were left at room temperature (25-30 °C) to dry. The date pits were then roasted in a pan for about 25-30 minutes at a temperature of 180°C (Fikry et al., 2019). This roasting condition (180°C) was chosen to prevent nutritional deterioration and enhance flavor. During roasting, the pits were continuously stirred to avoid burning. After the roasting was done, the date pits were removed and allowed to cool at room temperature. Lastly, the roasted date pits were ground to make a fine coffee powder using the coffee grinder (Model: ZCG495-120V, PSCIR, Pakistan). Different ratios of date pit coffee (%) and coffee (%), e.g., T_0 (100% coffee), T_1 (100% date pit coffee), and T_2, a combination of (30-70%) coffee and date pit coffee, were used. To achieve standardized brewing of these treatments, a ratio of powder to water of 1:15 was used, in which water was kept at 92-96°C. Individual samples were left to steep for an immersion time of 5-7 minutes to extract all bioactive compounds and sensory volatiles before actual sampling was done to analyze utilizing additional physicochemical and antioxidant assays (Muzykiewicz-Szymańska, Nowak, Wira, & Klimowicz, 2021).

Table 1. Treatment plan for the development of date pit coffee

Treatments	Coffee (%)	Date Pits Coffee (%)
T_0 – 100% traditional coffee	100	-
T_1 – 100% date pit coffee	-	100
T_2 – Blend (30% coffee + 70% date pit coffee)	30	70

2.4 Physicochemical Analyses of the Developed Coffee

To determine the proximate composition of the developed coffee, including moisture, ash, and protein, to evaluate its nutritional profile and quality attributes using the protocol of AOAC (2023). To ensure the credibility of the results, all the analyses were performed in triplicate (n=3).

2.4.1 Moisture Content

In this procedure, 10 g of the sample was subjected to drying in a hot air oven (Model: DO-1-30-02, UCP Lahore, Pakistan), followed by AOAC using the official method No. 1-93401 at a controlled temperature of 105±5°C according to the method of AOAC (2023). The moisture loss percentage was calculated by subtracting the weight of the

dried sample from the initial weight, and then expressing this difference as a percentage relative to the initial weight as:

$$\text{Moisture content (\%)} = \frac{\text{(Initial sample weight- Weight of dried sample)}}{\text{Initial sample weight}} \times 100$$

2.4.2 Ash Content

A 5 g sample of date pit coffee was carefully placed in a crucible and directly exposed to flame until it was completely charred without any visible fumes as per the procedure of AOAC (2023). Subsequently, the charred sample was ignited in a muffle furnace (Model: MF-1/02, UCP Lahore, Pakistan) by the AOAC method No. 943-05 at a temperature range of 550-600 ºC for approximately 5-6 hours, until greyish white residues were obtained. The ash percentage was calculated as:

$$\text{Ash content(\%)} = \frac{\text{Weight of Ash}}{\text{Initial sample weight}} \times 100$$

2.4.3 Protein Content

The protein content was analyzed by the AOAC using the official method No. 1-98413. Two grams of the coffee sample was subjected to digestion with concentrated H_2SO_4 using a digestion mixture (K_2SO_4:$FeSO_4$:$CuSO_4$::100:5:10) according to the protocol of AOAC (2023). The digestion process lasted around three to four hours until the color turned light greenish. The digested sample was then transferred to a 250 mL volumetric flask and diluted with distilled water up to the mark. Next, in the distillation apparatus, 10 mL of 40% sodium hydroxide and 10 mL of the digested sample were added. The liberated ammonia was combined with a beaker containing a 4% solution of boric acid and methyl red indicator. This chemical reaction resulted in the formation of ammonium borate, which enabled the determination of the nitrogen content in the sample. The distillate was titrated against a 0.1 N solution of H_2SO_4 until a light golden color emerged. To calculate the crude protein content, the percentage of nitrogen was multiplied by a factor of 5.80.

$$\text{Nitrogen (\%)} = \frac{\text{(Volume of 0.1 N sulphuric acid used} \times 0.0014 \times 250)}{\text{Sample weight} \times \text{Aliquot volume)}} \times 100$$

$$\text{Crude protein (\%)} = \text{Nitrogen (\%)} \times 5.80$$

2.4.4 pH

The pH of the date pit coffee sample was determined using a digital pH meter (Model: InoLab 720, Germany) in accordance with the AOAC (2023) guidelines. A small quantity of the sample was carefully placed in the chamber block of the digital pH meter. The meter was then turned on to commence the pH measurement process.

2.4.5 Acidity

The acidity of the date pit coffee sample was determined using a digital acidity meter (Model: QA supplies LLC, USA) following the method of AOAC (2023). Accordingly, 10 g of date pit powder sample was first mixed in 30 mL of distilled water. The resultant solution was then poured on the electronic detector of the digital acidity meter and expressed as % acidity on a citric acid basis.

2.5 Antioxidant Assay of Developed Coffee

The antioxidant assay was assessed using the protocol of Awan et al. (2018) to determine the total phenol content and DPPH (1,1-diphenyl-2-picrylhydrazyl). All measurements were made 3 times (n=3).

2.5.1 Total Phenol Content

To assess the total phenolic content of the coffee samples, the Folin-Ciocalteu reagent-based method was employed, and for comparison, Gallic acid was used as the standard as per the methodology of Yaqoob et al. (2025). For analysis, 0.2 mL of extract of each sample and 0.5 mL of Folin-Ciocalteu phenol reagent (0.2 M/L) were added to test tubes and allowed to stand at room temperature for 5 minutes. Then, 0.4 mL of 0.75% sodium carbonate (Na_2CO_3) was added to the samples and mixed thoroughly. The samples were

incubated for 60 minutes at 25°C. The amount of phenolic content under analysis was measured by absorbance at 750 nm in the presence of a microplate reader (Model: ELx-800 BioTek, USA). The final values were expressed in milligrams of Gallic acid equivalents (mg GAE) per 100g as a standard curve. A coefficient of determination (R^2 >0.99) was used to determine the accuracy of this measure. The concentration of the phenolic content was calculated by use of the data of the absorbance in a linear regression standard curve equation:

$$y = mx + c$$

2.5.2 DPPH (1,1-diphenyl-2-picrylhydrazyl)

The methanolic coffee sample was measured by mixing 0.9 mL of freshly prepared solution with 0.1 mL of DPPH (1,1-diphenyl-2-picrylhydrazyl) solution following the method used by Yaqoob et al. (2025). Methanol of the same volume was taken as a control in comparison. The coffee treatments were incubated for 30 minutes at room temperature in the dark. After that, the optical density (OD) was measured at 517nm by using a microplate reader. The following equation was used to calculate the scavenging activity:

$$\text{DPPH activity (\%)} = \text{OD}_{\text{control}} - \frac{\text{OD sample}}{\text{OD}_{\text{control}}} \times 100$$

2.6 Storage Stability Assessment

All the treatments of date pits coffee (Table 1) were stored in an airtight jar at room temperature (25-30ºC) for 15 days using the method of Awan et al. (2017) with modifications. The objective of storage was to study the effect on their quality. The physicochemical and sensory tests of coffee treatments were performed in triplicate (n=3) at intervals of 0 and 15 days.

2.7 Sensory Evaluation

For the sensory evaluation of the three treatments, T_0, T_1 and T_2 (Table 1), a hedonic response approach was employed using a 9-point hedonic scale system. This system, as described by Awan et al. (2017), ranged from 9 (like extremely) to 1 (dislike). The evaluation of date pit coffee was conducted by both students and faculty members from the Department of Food Science & Technology at the University of Central Punjab, Lahore. The sensory attributes assessed included sample appearance, taste, color, aroma, and overall acceptability. To improve reliability, every sample was evaluated in triplicate (n=3). To ensure unbiased evaluations, the serving glasses were cleaned between samples using water at a temperature of 28ºC.

2.8 Statistical Analysis

In order to determine the importance of the data obtained in relation to each parameter, a careful statistical study was done. Statistical Package Version 8.1 was used to analyze a Completely Randomized Design (CRD), a two-way factorial design that would enable a strict and systematic approach to the analysis.

3. Results and Discussion

3.1 Physicochemical Analyses of the Developed Coffee

3.1.1 Moisture Content

The means for the moisture content (%) of date pits coffee at the intervals of 0 and 15 days are shown in Table 2. From the mean results, it is evident that the highest moisture content value among the treatments at 0 days was in T_2 8.84±0.01 followed by T_0 (control treatment) and T_1 (8.82±0.01 and 8.78±0.01, respectively. After storage for 15 days, a slight increase in the moisture content was observed in all treatments. The maximum increase among all treatments was observed in T_2 as 8.86±0.02, followed by T_0 and T_1 at 8.85±0.02 and 8.81±0.01. The

Table 2. Means for proximate analyses (moisture, ash, protein content) of date pits coffee samples

Parameters (%)	Treatments	Storage Days	
		0 day	15 days
Moisture Content	T_0	8.82±0.01	8.85±0.02
	T_1	8.78±0.01	8.81±0.01
	T_2	8.84±0.01	8.86±0.02
Ash Content	T_0	3.99±0.01	3.98±0.02
	T_1	3.98±0.01	3.97±0.01
	T_2	3.97±0.01	3.96±0.01
Protein Content	T_0	4.84±0.03	4.81±0.04
	T_1	4.99±0.02	4.97±0.01
	T_2	5.11±0.01	5.09±0.01

Values represent mean±SD

slight increase in moisture content over the 15-day storage period is likely due to humidity absorption from the surrounding environment. Even in controlled conditions, powdered substances like date pit coffee can absorb moisture from the air, especially if the storage containers are not completely airtight. This minor absorption raises the overall moisture content, as seen in all treatments, with T_2 showing the highest increase, likely due to its initial higher moisture level, making it more prone to further moisture absorption. Analysis showed that there were significant differences between treatments, especially for T_2 ($p < 0.05$). The present findings are aligned with the previous research studies that have explored the moisture content of date pit powder. Hossain et al. (2014) noted that the date

pits from different varieties revealed moisture contents between 3.1 and 12.5%, with some samples falling within the 7 to 9% range, which can be attributed to several factors: date variety, harvest and drying conditions, storage conditions, and processing methods.

3.1.2 Ash Content

The ash content (%) of date pits coffee at the intervals of 0 and 15 days is shown in Table 2. From the mean results, it is evident that the highest ash content (%) across the samples at 0 days was in T_0 (control treatment), 3.99±0.01, followed by T_1 and T_2, 3.98±0.01 and 3.98±0.01, respectively. After storage for 15 days, a slight decrease in the ash content was observed in all treatments, ranging from 3.97±0.01 to 3.98±0.02. Mean values for ash content at 15 days were 3.98±0.02 for T_0, 3.97±0.01 for T_1, and 3.96±0.01 for T_2. The slight decrease in ash content over the 15-day storage period could be due to moisture absorption. During storage, even minimal exposure to air can lead to moisture absorption in the powdered coffee, especially if the storage conditions are not perfectly airtight. This moisture content adds to the weight of the sample without affecting the mineral content, and this is reflected in a small apparent decrease in the percentage of ash content

in weight. Statistical comparison indicated significant differences ($p < 0.05$) between T_0 and T_2 at day 15 despite the minimal declines. The results of the current research are relatively in line with Al-Khalili, Al-Habsi, and Rahman (2023), who discovered that date pits are about 4.2% ash on a dry weight basis, reflecting a notable mineral content.

3.1.3 Protein Content

The means of date pit coffee protein content (100%) are shown in Table 2, at the intervals of 0 and 15 days. From the mean results, it is evident that the highest protein content (%) among the treatments at 0 days was in T_2 as 5.11±0.01, followed by T_1 and T_0 (control treatment) as 4.99±0.02 and 4.84±0.03, respectively. After storage for 15 days, a slight decrease in the protein content (%) was observed in all treatments. The maximum decrease among all treatments was noted in T_2 as 5.09±0.01, followed by T_1 and T_0 as 4.97±0.01 and 4.81±0.04, respectively. The slight decrease in protein content after 15 days of storage could be attributed to protein oxidation. During storage, especially in powdered form, proteins are more susceptible to exposure to air and potential oxidation. Despite being minor, the observed declines were statistically significant ($p < 0.05$), with T_2 exhibiting the highest initial protein and, hence, the most significant proportional loss. The findings of this study were also in accordance with the comprehensive analysis of date pits powder by Nwachukwu et al. (2024), who found that the protein content in date pits varies between 4.0 and 5.6%, depending on the variety and maturity of the seeds.

3.1.4 pH Value

The means for the pH values of date pits coffee at the time intervals of 0 and 15 days are presented in Table 3. At day 0, the maximum pH was measured in T_1 (6.78±0.01), then in T_2 (6.73±0.01) and T_0 (6.64±0.03). After 15 days of storage, all treatments recorded a small reduction in pH, with the greatest decrease in T_0 (6.54±0.01), whereas T_1 (6.76±0.01) and T_2 (6.63±0.02) maintained relatively higher stability. The small drop can be explained by the reaction with air and light, yielding minute acidic compounds. However, the capacity of date pits as a buffer constrained the overall change, and the pH stayed in a nearly neutral interval. The change was statistically significant ($p < 0.05$). The current results agree with the research study of Ghnimi et al. (2015), which found a 6-7 pH for date seed coffee as a neutral to slightly acidic pH nature,

Table 3. Means and mean squares of pH and titratable acidity of date pits coffee samples

Attributes	Treatments	Storage Days	
		0 day	15 days
pH	T_0	6.78±0.01	6.77±0.01
	T_1	6.73±0.01	6.72±0.01
	T_2	6.64±0.03	6.64±0.02
Acidity (%)	T_0	1.66±0.04	1.70±0.04
	T_1	1.86±0.04	1.91±0.07
	T_2	2.29±0.16	2.29±0.11

Values represent mean±SD

less bitter than conventional coffee, whose pH range is from 4.85-5.10.

3.1.5 Acidity Content

The means for the acidity content (%) of date pit coffee at the intervals of 0 and 15 days are shown in Table 3. The levels of acidity in the date pit coffee samples, as the concentration of hydrogen ions, were found to increment in order of T_0 and T_2, corresponding with a negative correlation with the measured values of pH. At T_0, the acidity was the lowest at 1.66±0.04, and the highest concentration was in T_2 at 2.29±0.16, indicating that the greater the percentage of date pits, the higher the organic acid release. There was a slight but significant increase in the concentration observed over the 15-day storage period in all treatments. Even so, increases in these will neither affect the standard deviations; hence, it shares a characteristic of good sample stability. This determines the date pit blend as a low-acid substitute that has a consistent chemical composition suitable for sensitive consumers. Research on the acidity content of date pits in coffee is limited. Alhamdan et al. (2021) noted that in most date beverages, the acidity tends to rise over extended storage, due to organic acid development and Maillard reaction products.

3.2 Antioxidant Assay of Developed Coffee

3.2.1 Total Phenol Content

The means for the TPC (mg GAE/100g) of date pits coffee at the intervals of 0 and 15 days are displayed in Figure 2. The highest TPC (mg GAE/100g) value among the treatments at 0 days was in T_1 as 144.13±1.59 mg GAE/100g, followed by T_2 and T_0 (control treatment) as 140.18±0.51 and 129.51±1.31 mg GAE/100g, respectively. After storage for 15 days, a slight decrease was observed in the TPC of all treatments. The maximum decrease was in T_0, at 127.19±1.26 mg GAE/100g, followed by T_2 and T_1, 139.65±0.62 and 140.19±1.19 mg GAE/100g, respectively. The highest decrease was in T_0, possibly because it initially had a higher TPC, making these sensitive compounds more prone to degradation over time. The present results are consistent with Lemine et al. (2014), who reported the TPC (mg GAE/100g) of date pits ranging from 121.55 to 741.63 mg GAE/100g. The TPC value also serves as a key indicator of the date pits coffee's potential for functional food applications.

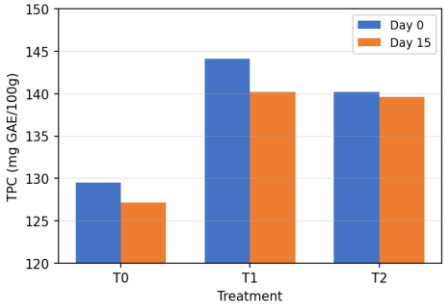

Figure 2. TPC analyses of coffee

3.2.2 DPPH (1,1-diphenyl-2-picrylhydrazyl)

The means for the DPPH (%) of date pits coffee at the intervals of 0 and 15 days are illustrated in Figure 3. The highest DPPH (%) value among the treatments at 0 days was in T_1 as 60.46±0.75, followed by T_2 and T_0 (control treatment) as 58.43±0.45 and 47.94±0.85, respectively. After storage for 15 days, it was observed that there is a slight decrease in DPPH (%) of T_1, T_2, and T_0 as 60.42±0.46, 55.36±0.37, and 43.91±0.31. The current findings align with those of Bijami et al. (2020), who reported the DPPH of date pits ranging from 49.25 to 71.35%. The T_1 had the highest radical scavenging activity of 60.46±0.75. The presence of hydroxycinnamic acids, flavonoids, and tannins gives it this high antioxidant potential. Date pit coffee's phenolic matrix, which contains substances like gallic acid and catechins that donate protons to eliminate free radicals, explains its significant DPPH scavenging action.

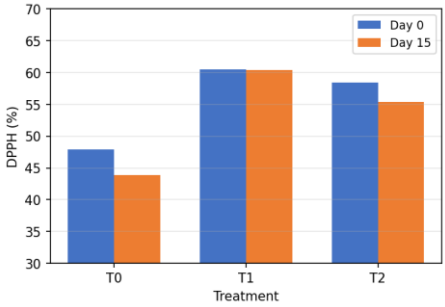

Figure 3. DPPH analyses of coffee

3.3 Sensory Evaluation of Developed Coffee

The sensory evaluation was conducted by a panel of 12 participants using a 9-point hedonic scale. Figure 4 shows the mean hedonic score of the hedonic response to all coffee treatments based on the characteristics of color, taste, flavor, aroma, and overall acceptability. The data were compared through factorial analysis of variance (ANOVA) to identify the primary effect of two variables, Treatment (T_0, T_1, T_2) and Storage Time (Day 0, Day 15), and the interaction of both. The radar graph shows the sensory profile of the products with scores between 6 and 9, with high scores implying a high degree of consumer preference. Sample T_1 (100% date pit coffee) achieved the greatest result in all characteristics, especially in taste and general acceptability, reflecting high consumer appeal. Sample T_0 (conventional coffee) scored lower in most of the traits, particularly aroma, making it the least preferred of the three treatments. Sample T_2 maintained a middle-ground profile with the highest score in colour and aroma. The present findings comply with those made by Babiker et al. (2020), who demonstrated that roasted date pits could be used in the creation of a palatable drink that resembles coffee but has functional health properties.

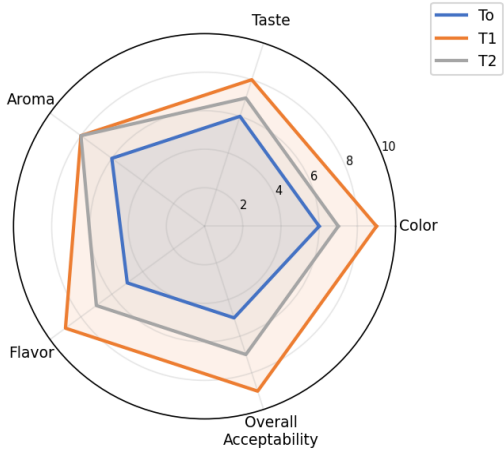

Figure 4. Hedonic response to developed coffee

4. Conclusion & Further Research

This study shows the feasibility of converting date pits into a potential coffee substitute with significant health benefits and powerful antioxidant properties. The 100% T_1 and blended T_2 date pit coffee formulations demonstrated promising sensory qualities in aroma, mouthfeel, and overall acceptability across tested formulations. The caffeine-free aspect and the positive nutritional balance position date pit coffee as a low-calorie and functional beverage appropriate for health-conscious people. Moreover, the innovation will help reduce agricultural waste, which is one of the stated objectives of global sustainability through the upcycling of date pits into value-added products. Although these are promising results, the research still needs more studies to prove the health benefits by means of clinical trials, such as blood sugar control and metabolic effects in the long run. Long shelf-life testing of the product under different storage conditions is also required to test commercial stability. In addition, the process of scaling to pilot and industrial production stages will involve the optimization of processing conditions and a full study of consumer

acceptability among various consumer groups.

5. Funding

The authors state that there was no funding, grant, or any other assistance in the process of preparing this manuscript.

5.1 Competing Interests

There are no relevant non-financial or financial interests of the authors.

5.2 Acknowledgment

The authors are grateful to Lab System, University of Central Punjab, Lahore, Pakistan, for supplying them with the equipment to undertake this investigation.

References

Al-Khalili, M., Al-Habsi, N., & Rahman, M. S. (2023). Applications of date pits in foods to enhance their functionality and quality: A review. Frontiers in Sustainable Food Systems, 6, 1101043.

Alhamdan, A. M., Al Juhaimi, F. Y., Hassan, B. H., Ehmed, K. A., & Mohamed Ahmed, I. A. (2021). Physicochemical, microbiological, and sensorial quality attributes of a fermented milk drink (Laban) fortified with date syrup (dibs) during cold storage. Foods, 10(12), 3157.

AOAC. (2023). Official Methods of Analysis, 22nd Edition.

Attia, A. I., Reda, F. M., Patra, A. K., Elnesr, S. S., Attia, Y. A., & Alagawany, M. (2021). Date (Phoenix dactylifera L.) by-products: Chemical composition, nutritive value and applications in poultry nutrition, an updating review. Animals, 11(4), 1133.

Awan, K., Butt, M., Haq, I., Ashfaq, F., & Suleria, H. (2017). Storage stability of garlic fortified chicken bites. J. Food Chem. Nanotechnol, 3(2), 80-85.

Awan, K. A. (2017). Probing the restorative potential of dates (Phoenix dactylifera) against atherogenic diet-induced cardiac and hepatic stress. University of Agriculture, Faisalabad, Pakistan.

Awan, K. A., Butt, M. S., Munir, H., Sultan, W., Yaqoob, S., Nayik, G. A., ... & Gere, A. (2025). Restorative potential of Phoenix dactylifera fruit and extract against oxidative stress-mediated cardiac dysfunction in rodent experimental modeling. Journal of Functional Foods, 128, 106845.

Awan, K. A., Butt, M. S., Sharif, M. K., & Hussain, F. (2018). Compositional profiling of selected Pakistani date cultivars. Pakistan Journal of Agricultural Sciences, 55(3).

Awan, K. A., Yaqoob, S., Ul-Haq, I., Naveed, H., Imtiaz, A., Shaukat, A., ... & Shen, Q. (2025). Therapeutic Power of Date Fruit (Phoenix dactylifera L.): A Nutrient-Rich Superfood for Holistic Health and Disease Prevention. Food Science & Nutrition, 13(9), e70896.

Babiker, E. E., Atasoy, G., Özcan, M. M., Juhaimi, F. A., Ghafoor, K., Ahmed, I. A. M., & Almusallam, I. A. (2020). Bioactive compounds, minerals, fatty acids, color, and sensory profile of roasted date (Phoenix dactylifera L.) seed. Journal of Food Processing and Preservation, 44(7), e14495.

Bijami, A., Rezanejad, F., Oloumi, H., & Mozafari, H. (2020). Minerals, antioxidant compounds and phenolic profile regarding date palm (Phoenix dactylifera L.) seed development. Scientia Horticulturae, 262, 109017.

Fikry, M., Yusof, Y. A., M. Al-Awaadh, A., Abdul Rahman, R., Chin, N. L., & Ghazali, H. M. (2019). Antioxidative and quality properties of full-fat date seeds brew as influenced by the roasting conditions. Antioxidants, 8(7), 226.

Ghnimi, S., Almansoori, R., Jobe, B., Hassan, M., & Afaf, K. (2015). Quality evaluation of coffee-like beverage from date seeds (Phoenix dactylifera, L.). J. Food Process. Technol, 6(12), 1-6.

Hossain, M. Z., Waly, M. I., Singh, V., Sequeira, V., & Rahman, M. S. (2014). Chemical composition of date-pits and its potential for developing value-added product - a review. Polish Journal of Food and Nutrition Sciences, 64(4).

Lemine, F. M. M., Ahmed, M. V. O. M., Maoulainine, L. B. M., Zein el Abidine, O. B., Samb, A., & Boukhary, A. O. M. S. O. (2014). Antioxidant activity of various Mauritanian date palm (Phoenix dactylifera L.) fruits at two edible ripening stages. Food Science & Nutrition, 2(6), 700.

Mahmud, M. C., Shellie, R. A., & Keast, R. (2020). Unravelling the relationship between aroma compounds and consumer acceptance: Coffee as an example. Comprehensive Reviews in Food Science and Food Safety, 19(5), 2380-2420.

Munir, H., Yaqoob, S., Awan, K. A., Imtiaz, A., Naveed, H., Ahmad, N., ... & Ma, Y. (2024). Unveiling the Chemistry of Citrus Peel: Insights into Nutraceutical Potential and Therapeutic Applications. Foods, 13(11), 1681.

Muzykiewicz-Szymańska, A., Nowak, A., Wira, D., & Klimowicz, A. (2021). The effect of brewing process parameters on antioxidant activity and caffeine content in infusions of roasted and unroasted Arabica coffee beans originated from different countries. Molecules, 26(12), 3681.

Naveed, H., Sultan, W., Awan, K. A., Imtiaz, A., Yaqoob, S., Al-Asmari, F., ... & Mugabi, R. (2024). Glycemic impact of cereal and legume-based bakery products: Implications for chronic disease management. Food Chemistry: X, 101959.

Nwachukwu, S. C., Edo, G. I., Samuel, P. O., Jikah, A. N., Oloni, G. O., Ezekiel, G. O., & Agbo, J. J. (2024). The botanical details, pharmacological activities and industrial applications of date seed (Phoenix dactylifera L.). Phytochemistry Reviews, 1-25.

Samoggia, A., & Riedel, B. (2019). Consumers' perceptions of coffee health benefits and motives for coffee consumption and purchasing. Nutrients, 11(3), 653.

Tahmouzi, S., Nasab, S. S., Alizadeh-Salmani, B., Zare, L., Mollakhalili-Meybodi, N., & Nematollahi, A. (2024). Coffee substitutes: A review of the technology, characteristics, application, and future perspective. Comprehensive Reviews in Food Science and Food Safety, 23(6), e70041.

Yaqoob, S., Imtiaz, A., Awan, K. A., Naveed, H., Faraz, A., Sobhy, R., ... & Shen, Q. (2025). Synergistic impact of multi-frequency ultrasound on sea buckthorn juice fermentation: A holistic study on bioactive compounds, micromorphology, sensory quality, and computational evidence. Ultrasonics Sonochemistry, 107571.

UCP Journal of Science and Technology
Vol. 3, Issue 2 (January - June 2026)
Journal website: http://ojs.ucp.edu.pk/index.php/ucpjst/index

Association of Smog and Fog with the Prevalence of Asthma and Pneumonia in the Population of Punjab

Farah Ashaf[1], Farkhanda Manzoor[1], Ahmad Bakhsh[3], Asifa[1], Sadaf Aman[2*]

Abstract

The present study was conducted to assess the prevalence of asthma and pneumonia due to smog and fog in the affected and normal population of males and females. The data were collected by means of questionnaires and interviews in DHQ (District Headquarters) Hospital, Chiniot, on 500 subjects. All subjects were categorized into two groups with respect to their age. Group A (age ≤ 43) and Group B (age ≤ 84); Group A contained n_A = 376 and Group B contained n_B = 124 subjects, respectively. The parameters like height, weight, BMI, age, and gender were included. The socio-economic status and family history were also included. All the data and parameters were analyzed statistically by chi-square using SPSS software (version 22). 73.6% of subjects showed the presence of Asthma and Pneumonia. 33.6% of samples were affected by Asthma ($p \leq 0.0001$), 40% were infected by Pneumonia (For A group $p \leq 0.0001$) (For B group $p \leq 0.002$), and 26.4% were normal and did not show any symptoms. The climatic conditions such as temperature, humidity, and weather (smog, fog) played a vital role. The increased level of smog and fog is the cause of the prevalence of many respiratory diseases such as shortness of breath (asthma) and pneumonia. The average temperature during October was 31°C, November 21°C, December 18°C, January 16°C, February 19°C and March was 27°C. The results of this study revealed that smog, fog, education, and socio-economic status were also related to the prevalence of these diseases.

Keywords: Asthma, Pneumonia, Smog, Fog, Population of Punjab.

1. Introduction

Smog is a bothersome concoction of gases and airborne particles that is created by smoke and fog in the presence of sunlight. Smog formation is directly correlated with the land's topography and weather (Chang, Xu et al. 2016). Incinerators, landfills, and sewage treatment plants are examples of facilities that treat human waste and release a variety of harmful gases into the atmosphere. Landfills release more than 100 harmful gases. Among them, hydrogen sulfide and methane are the most prevalent (Filippini, Heck et al. 2015).

There are numerous chemicals (a total of 187) that are known to be air toxics, including benzene, chloroform, acetaldehyde, dioxin, polycyclic organic matter, chromium, lead, nickel, and mercury compounds. Cancer and other major health problems, such as birth defects and human reproduction, can be brought on by air pollutants (Mulikat 2022). According to EPA estimates, half of all cancers brought on by air pollution are caused by air toxics released by cars and

[1]Department of Zoology, Lahore College for Women University, Lahore
[2]School of Biology, Minhaj University, Lahore
[3]School of Biochemistry, Minhaj University, Lahore
[*]Corresponding author's E-mail: sadafaman.zoology@mul.edu.pk
Received: 03 July 2026; Received in revised form: 09 July 2026; Accepted: 10 July 2026.
Available online: 13 July 2026.

DOI: https://doi.org/10.24312/ucp-jst.03.02.609

trucks, such as benzene, acetaldehyde, and 1, 3-butadiene. The National Emissions Inventory measures VOC emissions. Numerous compounds, including nitric oxide, nitrogen dioxide, and nitrous oxide, can be created when nitrogen and oxygen combine (Thompson, Shimabuku et al. 2016).

The human body's cardio respiratory system is the primary target of CO. Power plants that burn coal and automobiles that run on diesel produce sulfur dioxide (SO_2). Rain that contains sulfur dioxide (SO_2) dissolves and turns into sulfuric acid, or acid rain, which is harmful to plants. The biggest health risk to young children and asthmatics is sulfur dioxide, which can react in the atmosphere to form fine particles. Pregnancy loss occurs when SO_2 disrupts fetal growth in females (Chen, Kuschner et al. 2007).

PM_{10} is defined as particulates such as dust, pollen, and mold, with a diameter smaller than 10 µm. PM2.5 frequently contains heavy metals such as Cd, Cr, Cu, Fe, Mn, Ni, As, and Pb. Some PM2.5 particles can have sizes as small as 0.1 mm, which is very close to the range of nanoparticles. These particles can adhere to the lungs and enter the bloodstream; some of them even start in the brain (Maher et al., 2016). Over the past few decades, there has been an increasing trend in the frequency of fog over South Asia during the winter months (Syed, Körnich et al., 2012). The phenomenon's crippling effects extend beyond human health because ozone in smog also inhibits vegetation growth, severely damaging crops and forests. It can also hasten the deterioration of rubber tires, paints, and textile dyes (Yoon, Burrows et al., 2014).

Areas with higher ambient pollution levels had higher death rates. Smog is thought to be the cause of over 2 million premature infant deaths in China and India (Jia and Wang, 2017). An increase in pneumonia-related deaths was the immediate result. Many pneumonia-related deaths are referred to as “acute respiratory distress syndrome” or “acute lung injury”. Diseases of the heart, lungs, skin, and eyes, as well as disorders of the nervous system, inflammatory response, and cancer, are all closely linked to exposure to smog, according to numerous studies. The country's economy, irrigation system, and human life have all been impacted in different ways by the rising trend of fog frequencies over the past ten years (Jacquemin, Sunyer et al. 2009).

Children's health and quality of life are greatly impacted by asthma, which is the primary cause of illness and hospitalizations in this age group. The most common non-infectious illness in children is asthma (Zar and Ferkol 2014), which impacts 235 million individuals worldwide, with a rising incidence in low- and middle-income nations. There is strong evidence that preexisting asthma can be made worse by postnatal air pollution (Orellano, Quaranta et al. 2017).

Numerous studies have shown that air pollution has a negative impact on cardio-respiratory disorders (Forouzanfar, Alexander et al. 2015). According to other research, children who live close to roads or wood industries are more likely to get pneumonia, and a ban on diesel-powered cars may lower the number of hospital admissions for the illness (World Health Organization, 2005). According to available data, a number of risk factors could contribute to the development of pediatric pneumonia (Jackson, Mathews et al. 2013, Walker, Rudan et al. 2013, Sonego, Pellegrin et al. 2015). Asthma is a persistent illness. It results in recurring airway narrowing and inflammation (Mehta, Shin et al. 2013, Atkinson, Kang et al. 2014).

2. Materials and Methods

The data were collected from 500 subjects from the general population of Lahore, DHQ (District Headquarters) Hospital, Chiniot, and from different cities of Punjab. The purposely designed questionnaire was used to obtain data in

the present study. The study was conducted on 500 subjects who were divided into two groups on the basis of age: group A and group B. Group A contains 182 males and 194 females; on the other hand, group B contains 72 males and 52 females. The study was carried out from October 2017 to March 2018.

2.1 Experimental Design

To assess the prevalence of Asthma and Pneumonia due to smog and fog in the population of Punjab in 500 subjects, a questionnaire was designed, and information regarding anthropometric measurements like age, gender, family history of that disease, and socioeconomic status was noted as well.

2.2 BMI (Body Mass Index)

BMI is a simple calculation using a person's height and weight. The formula is:

$$BMI = Kg/m^2$$

Where Kg is a person's weight in kilograms, and m^2 is their height in square meters. In order to calculate the BMI, the height must be converted to meters. For that purpose, first the feet of height were converted into inches, then into centimeters (cm), and then into meters (m). At the end, the square of the meter value was taken:

12 inch = 1 feet

1 m = 100 cm

According to the above values, the height in feet was converted into meters. By that procedure, the different BMIs of different samples were obtained.

Underweight = < 18.5; Normal = 18.5–24.9;

Overweight = 25.0–29.0; Obesity = 30.0–>40

2.3 Asthma

Many people had symptoms like coughing, and the duration of coughing was very long and severe in smog and fog during the months of October, November, December, and January. But some people had no symptoms like that. The presence and absence of that symptom showed the presence or absence of some disorders. Shortness of breath was very common. Due to air pollution, some people had difficulty breathing, and this problem was present in samples collected from different areas of Punjab. The duration of these symptoms definitely shows the prevalence of some disorders.

2.4 Pneumonia

Chest pain was also observed on the foggy days. The questionnaire and interview taken from the people estimated that the weather was the reason for the prevalence of these symptoms. In collected samples, some people had this symptom along with other symptoms. Conversely, some did not have this symptom, and some had only this symptom with no other disorders. Some people had a severe type of cold and shivering on smoggy days; some had no problem with that, and some had a mild effect.

The people who had these symptoms had a family history related to them, and some subjects who were affected by these symptoms had no family history, showing that the cause was not related to family history. They might be affected by weather conditions instead.

2.5 Climate Conditions

2.5.1 Temperature

Temperature was the climatic factor that affected many seasonal and other disorders. The temperature was recorded during the smoggy and foggy days from October to March, and was low during December, January, and February. The temperature was around 22–24 °C.

2.5.2 Humidity

Humidity was also very high during 3–4 months, becoming low to high at around 63–74%. Humidity was recorded from October 2017 to March 2018. At high humidity, the temperature was low, e.g., at 74% humidity the temperature was 24°C.

2.5.3 Weather

Smog was recorded from October 2017 to January 2018. In low temperatures

and high humidity, the weather was smoggy. Fog was also recorded in the winter months, e.g., in January and February, typically in the morning before sunrise. The weather was mostly cloudy during October 2017 and January 2018, and partly cloudy during October and January. Passing clouds, scattered clouds, and morning clouds were also present during those months. Haze, overcast conditions, scattered showers, and sprinkles were present in October, November, and December, while light and heavy rain was recorded during February 2018.

2.6 Statistical Analysis

Continuous variables (BMI, height, weight, and age) were expressed as mean ± standard deviation, and qualitative variables (coughing, fever, wheezing, chest pain, shortness of breath, and cold symptoms) were expressed as mean and percentage. The chi-square test was used to measure the significance of differences between qualitative parameters of the two respiratory diseases (asthma, pneumonia) using p-values.

3. Results

This study was conducted on 500 subjects, including males, females, and children of different ages. The ages ranged from 3 to 84 years. These subjects were divided into two groups, group A and group B. Group A consisted of 376 subjects with ages ranging from 3 to 43 years. Group B consisted of 124 subjects with ages ranging from 44 to 84 years.

3.1 Continuous Variables of Group A and Group B

Table 1 shows the mean with standard deviation of both Group A and Group B. The continuous variables used in this study were age, gender, height, weight, and BMI. The mean age with standard deviation of Group A was 25.11±9.74, and of Group B was 58.32±10.91. The mean height with standard deviation of Group A was 1.648±0.25, and of Group B was 1.79±0.14. The mean weight with standard deviation of Group A was 55.20±12.21, and of Group B was 63.09±8.35. The mean BMI with standard deviation of Group A was 19.66±3.44, and of Group B was 19.78±3.31.

Table 1. Continuous variables of group A and group B

Group	Age (years) Mean ±SD	Height (m) Mean ±SD	Weight (kg) Mean ±SD	BMI Mean ±SD
A	25.11±9.74	1.648±0.25	55.20±12.21	19.66±3.44
B	58.32±10.91	1.79±0.14	63.09±8.35	19.78±3.31

3.2 Qualitative Characteristics of Group A

The sample size of this group was 376, with age ranging from 3 to 43 years. The qualitative characteristics of this group were assessed according to two respiratory diseases: asthma and pneumonia. In asthma, the symptoms of coughing, wheezing, chest pain, and shortness of breath were included. In pneumonia, the symptoms of coughing, fever, chest pain, and cold were included. The symptoms of both asthma and pneumonia are much alike because these are respiratory diseases sharing similar symptoms. The family histories of these diseases were also recorded.

3.2.1 Symptoms of Asthma

Table 2 shows the symptoms of asthma. In group A, the total number of males was 182, and the total number of females was 194. The affected people were 284, and the normal were 92. Of the 376 subjects, 130 were affected by coughing, and 246 were normal with no effect of coughing; the mean of the coughing cases

was 0.345 with a percentage of 35% (p = 0.0001, highly significant). Normal cases had a mean of 0.65 and a percentage of 65%. For wheezing, 125 people were affected, with a mean and percentage of 0.33 and 33% (p = 0.0001); normal cases had mean 0.65 and percentage 65%. Shortness of breath affected 130 people, with mean 0.345 and percentage 35%; normal cases showed the same values as above. All the above symptoms indicated that 130 people were suffering from asthma in group A. A total of 130 cases of asthma were found in group A.

Table 2. Prevalence of asthma symptoms due to smog and fog in the population of Punjab from 3 to 43 years, male and female

Symptoms of Asthma	Total n=376	Mean	Percentage %	P-value
Coughing				
+ve	130	0.345	35%	P<0.0001
-ve	246	0.645	65%	
Wheezing				
+ve	125	0.332	33%	P<0.0001
-ve	251	0.667	67%	
Chest pain				
+ve	130	0.345	35%	P<0.0001
-ve	246	0.654	65%	
Shortness of Breath				
+ve	130	0.345	35%	P<0.0001
-ve	246	0.654	65%	
Cases of Asthma				
+ve	130	0.345	35%	P<0.0001
-ve	246	0.654	65%	

3.2.2 Symptoms of Pneumonia

Table 3 shows the symptoms of pneumonia: 150 coughing cases were recorded with a mean value of 0.398 and a percentage of 40% (p = 0.0001, highly significant); 236 normal cases had mean 0.627 and percentage 63%. Chest pain affected 154 people, with mean 0.409 and percentage 41%; 222 normal cases had mean 0.59 and percentage 59%. For cold, 150 people were affected, with a mean value of 0.398 and percentage 40%, matching the coughing symptom values. These symptoms indicated a total of 154 people affected, with p = 0.0001 (highly significant).

Table 3. Prevalence of pneumonia symptoms due to smog and fog in the population of Punjab from 3 to 43 years, male and female

Symptoms of Pneumonia	Total n=376	Mean	Percentage %	P-value
Coughing				
+ve	150	0.398	40%	P<0.0001
-ve	226	0.601	60%	
Fever	140	0.372	37%	P<0.0001
+ve	236	0.627	63%	

-ve				
Chest pain	154	0.409	41%	P<0.0001
+ve				
-ve	222	0.590	59%	
Cold	150	0.398	40%	P<0.0001
+ve				
-ve	226	0.601	60%	
Cases of Pneumonia	154	0.409	41%	P<0.0001
+ve				
-ve	222	0.590	59%	

4. Discussion

This study consisted of 500 subjects; samples were collected via questionnaires and interviews from the local population of Punjab with respect to the two respiratory diseases, asthma and pneumonia. This study included males and females of different age groups. The sample consisted of 254 males and 246 females, conducted on two groups: group A (376 subjects) and group B (124 subjects). The current study showed that of the 500 samples, 368 were affected and 132 were normal. The symptoms of both respiratory diseases were not identical, but shared some overlap, such as coughing and chest pain. Samples were collected from people via questionnaires and interviews. The occurrence of symptoms indicated the presence of a respiratory defect; some people showed no disorder, while others had severe infection. The present study showed that smog and fog during the winter directly and indirectly affected human health, particularly through respiratory diseases such as asthma and pneumonia. The prevalence of asthma and pneumonia due to smog and fog was also measured against weather conditions such as smog, fog, rain, cloud cover, scattered clouds, and sprinkles.

This study revealed that weather pollution such as smog and fog highly affected human health from October to February. Gases released by motors, factories, and chlorofluorocarbons combine with other air pollutants to form smog. Clark and coworkers (2010) studied the effect of smog on human health; when fuels burn, the gases or pollutants that cause smog are released into the atmosphere. In predisposed individuals, the main cause of allergic symptoms is the presence of airborne pollutants. Chronic inflammation is one of the most harmful allergic reactions, and can gradually harm tissue wherever it arises; in some parts of the body, recurring allergic reactions can cause organ damage (Clark, Demers et al. 2010). This confirms that the present findings are related to Clark and colleagues' work.

In the present study, the prevalence of asthma was examined; in group A, of the 182 males and 194 females, 130 members were affected by asthma — 61 of 182 males and 69 of 194 females. Chang (2012) studied asthma patients and concluded that in some cases breathing problems lead to heart problems, even though asthmatics typically only have brief episodes of trouble breathing.

The gases nitrogen dioxide (NO_2), ozone (O_3), volatile organic compounds (VOCs), and particulate matter (PM), which includes soot, are the pollutants that have been studied the most (Bates and Sizto 1987). More than 3% of the yearly disability-adjusted life years lost in 2010 were caused by outdoor air pollution. According to a study of ten European Cities, exposure to pollutants associated with traffic was responsible for 15% of all

exacerbations of childhood asthma and 14% of incident asthma cases in children. This confirms that Chang's work is related to the present work, while the work of Bates, Sizto and Brunekreef is somewhat different but still connected (Chang, Xu et al. 2016).

The consistent rise in asthma prevalence in developed nations has numerous detrimental effects on cardiopulmonary health that have been linked to air pollution, both indoors and outdoors. The gases nitrogen dioxide (NO_2), ozone (O_3), volatile organic compounds (VOCs), and particulate matter (PM), which includes soot, are the pollutants that have been studied the most (Bates and Sizto 1987).

More than 3% of the yearly disability-adjusted life years lost in 2010 were caused by outdoor air pollution. According to a study of ten European Cities, exposure to pollutants associated with traffic was responsible for 15% of all exacerbations of childhood asthma and 14% of incident asthma cases in children. Asthma is significantly exacerbated by urbanization, which may be partially caused by higher levels of outdoor air pollution. The prevalence of asthma is expected to rise globally as a result of fast population growth and rising levels of outdoor air pollution in many developing world cities (Brunekreef, Stewart et al. 2009). While Chang's work is connected to the current work, Bates, Sizto, and Brunekreef's work is somewhat different but still connected. Children of educated mothers have a better outcome than others because they are able to identify the signs and symptoms of pneumonia early and seek medical attention sooner (Sharma, Jain et al. 2013).

Pneumonia is one such infectious killer that has contributed to the deaths of countless people worldwide. Numerous health problems that can result in pneumonia are caused by smog; therefore, those who smoke regularly, have kidney-related conditions, or have diabetes are particularly vulnerable to pneumonia. A lung infection brought on by bacteria, viruses, fungi, or parasites in the air we breathe is known as pneumonia (Marsh, Gilroy et al. 2008). When determining the burden attributable to air pollution, the set of pollutants significantly linked to pneumonia raises the question of which one to use. According to the Global Burden of Disease study (GBD), which took into account both PM and O_3, the former was identified as the primary cause of disability globally (Ghimire, Bhattacharya et al. 2012).

5. Conclusion

The increased level of smog and fog is the cause of the prevalence of many respiratory diseases such as shortness of breath (asthma) and pneumonia. In this study, family history and socioeconomic status played an important role; poorer children were mostly infected with pneumonia. The present study concluded that when temperature was between 18–27°C and humidity was between 61–94% during smoggy and foggy days, 12% of males in group A were affected by asthma and 14% by pneumonia, while in group B, 4% of males were affected by asthma and 5% by pneumonia. In group A, 14% of females were affected by asthma and 20% by pneumonia; in group B, 4% of females were affected by asthma and 4% by pneumonia. Elevated air pollution played a vital role in respiratory diseases, and temperature and humidity were also involved in the prevalence of these diseases. It is concluded that persons who face more exposure to the atmosphere during smog and fog are the major victims of pneumonia and asthma prevalence.

References

Atkinson, R., et al. (2014). "Epidemiological time series studies of PM2.5 and daily mortality and hospital admissions: a systematic review and meta-analysis." Thorax 69(7): 660-665.

Bates, D. V. and R. Sizto (1987). "Air pollution and hospital admissions in

Southern Ontario: the acid summer haze effect." Environmental Research 43(2): 317-331.

Brunekreef, B., et al. (2009). "Self-reported truck traffic on the street of residence and symptoms of asthma and allergic disease: a global relationship in ISAAC phase 3." Environmental Health Perspectives 117(11): 1791-1798.

Chang, C. (2012). "Asthma in children and adolescents: a comprehensive approach to diagnosis and management." Clinical Reviews in Allergy & Immunology 43: 98-137.

Chang, L., et al. (2016). "Impact of the 2015 El Niño event on winter air quality in China." Scientific Reports 6(1): 34275.

Chen, T.-M., et al. (2007). "Outdoor air pollution: nitrogen dioxide, sulfur dioxide, and carbon monoxide health effects." The American Journal of the Medical Sciences 333(4): 249-256.

Clark, N. A., et al. (2010). "Effect of early life exposure to air pollution on development of childhood asthma." Environmental Health Perspectives 118(2): 284-290.

Filippini, T., et al. (2015). "A review and meta-analysis of outdoor air pollution and risk of childhood leukemia." Journal of Environmental Science and Health, Part C 33(1): 36-66.

Forouzanfar, M. H., et al. (2015). "Global, regional, and national comparative risk assessment of 79 behavioural, environmental and occupational, and metabolic risks or clusters of risks in 188 countries, 1990–2013: a systematic analysis for the Global Burden of Disease Study 2013." The Lancet 386(10010): 2287-2323.

Ghimire, M., et al. (2012). "Pneumonia in South-East Asia region: public health perspective." Indian Journal of Medical Research 135(4): 459-468.

Jackson, S., et al. (2013). "Risk factors for severe acute lower respiratory infections in children – a systematic review and meta-analysis." Croatian Medical Journal 54(2): 110-121.

Jacquemin, B., et al. (2009). "Association between modelled traffic-related air pollution and asthma score in the ECRHS." European Respiratory Journal 34(4): 834-842.

Jia, H. and L. Wang (2017). "Peering into China's thick smog." C&EN Global Enterprise 95(4): 19-22.

Marsh, D. R., et al. (2008). "Community case management of pneumonia: at a tipping point?" Bulletin of the World Health Organization 86: 381-389.

Mehta, S., et al. (2013). "Ambient particulate air pollution and acute lower respiratory infections: a systematic review and implications for estimating the global burden of disease." Air Quality, Atmosphere & Health 6: 69-83.

Mulikat, S. O. (2022). Assessment of Heavy Metals, Persistent Organic Pollutants and Polycyclic Aromatic Hydrocarbons Contamination of Soil and Underground Water of Selected Abattoir Markets in North Central Nigeria, Kwara State University (Nigeria).

Orellano, P., et al. (2017). "Effect of outdoor air pollution on asthma exacerbations in children and adults: systematic review and multilevel meta-analysis." PloS One 12(3): e0174050.

Sharma, S. B., et al. (2013). "The effects of air pollution on the environment and human health." Indian Journal of Research in Pharmacy and Biotechnology 1(3): 391.

Sonego, M., et al. (2015). "Risk factors for mortality from acute lower respiratory infections (ALRI) in children under five years of age in low and middle-income countries: a systematic review and meta-analysis of observational studies." PloS One 10(1): e0116380.

Syed, F. S., et al. (2012). "On the fog variability over South Asia." Climate Dynamics 39: 2993-3005.

Thompson, K. A., et al. (2016). "Environmental comparison of biochar and activated carbon for tertiary

wastewater treatment." Environmental Science & Technology 50(20): 11253-11262.

Walker, C. L. F., et al. (2013). "Global burden of childhood pneumonia and diarrhoea." The Lancet 381(9875): 1405-1416.

Yoon, J., et al. (2014). "Changes in atmospheric aerosol loading retrieved from space-based measurements during the past decade." Atmospheric Chemistry and Physics 14(13): 6881-6902.

Zar, H. J. and T. W. Ferkol (2014). "The global burden of respiratory disease — impact on child health." 49: 430-434.

UCP Journal of Science and Technology
Vol. 3, Issue 2 (January – June 2026)
Journal website: http://ojs.ucp.edu.pk/index.php/ucpjst/index

Manuscript Submission Guidelines

Manuscript Submission

Submission of a manuscript implies: that the work described has not been published before; that it is not under consideration for publication anywhere else; that its publication has been approved by all co-authors, if any, as well as by the responsible authorities – tacitly or explicitly – at the institute where the work has been carried out. The publisher will not be held legally responsible should there be any claims for compensation.

Permissions

Authors wishing to include figures, tables, or text passages that have already been published elsewhere are required to obtain permission from the copyright owner(s) for both the print and online format and to include evidence that such permission has been granted when submitting their papers. Any material received without such evidence will be assumed to originate from the authors.

Online Submission

Please follow the hyperlink "Submit manuscript" and upload all of your manuscript files following the instructions given on the screen.

Source Files

Please ensure you provide all relevant editable source files at every submission and revision. Failing to submit a complete set of editable source files will result in your article not being considered for review. For your manuscript text please always submit in common word processing formats such as .docx or LaTeX.

Title Page

The title page should include:

- The name(s) of the author(s)
- A concise and informative title
    - Please avoid acronyms in the title of your article
    - For local studies, please indicate the name of the region and country in the title.
- The affiliation(s) and address(es) of the author(s)
- The e-mail address, telephone and fax numbers of the corresponding author

Abstract

Please provide an abstract of about 200 words for review and research article and 100 words for a case study. The abstract should begin with a brief but precise statement of the problem or issue, followed by a description of the research method and design, the major findings, and the conclusions reached.

Keywords

Please provide 3 to 5 keywords which can be used for indexing purposes.

Text Formatting

- Manuscripts should be submitted in Word.
- Use a normal, plain font (e.g., 10-point Times Roman) for text with 1 line spacing.
- Use the automatic page numbering function to number the pages.
- Do not use field functions.
- Use tab stops or other commands for indents, not the space bar.
- Use the table function, not spreadsheets, to make tables.
- Use the equation editor or MathType for equations.

Tables

- All tables are to be numbered using Arabic numerals such as **Table 1**
- Tables should always be placed and cited in text in consecutive numerical order.
- For each table, please supply a table caption (title) explaining the components of the table.
- Table captions begin with the term Figure. in bold type, followed by the figure number, also in bold type.
- Identify any previously published material by giving the original source in the form of a reference at the end of the table caption.
- Footnotes to tables should be indicated by superscript lower-case letters (or asterisks for significance values and other statistical data) and included beneath the table body.

Figure Lettering

- To add lettering, it is best to use Helvetica or Arial (sans serif fonts).
- Keep lettering consistently sized throughout your final-sized artwork, usually about 2–3 mm (8 pt).
- Avoid effects such as shading, outline letters, etc.
- Do not include titles or captions within your illustrations.

Figure Numbering

- All figures are to be numbered using Arabic numerals such as **Figure 1**
- Figures should always be cited in text in consecutive numerical order.
- Figure parts should be denoted by lowercase letters (a, b, c, etc.).

Figure Captions

- Each figure should have a concise caption describing accurately what the figure depicts. Include the captions in the text file of the manuscript, not in the figure file.
- Figure captions begin with the term Figure. in bold type, followed by the figure number, also in bold type.
- Identify all elements found in the figure in the figure caption; and use boxes, circles, etc., as coordinate points in graphs.
- Identify previously published material by giving the original source in the form of a reference citation at the end of the figure caption.

- Figures should be provided in our required file formats, .jpg, .tif. If your figure is not in .jpg, .tif or .pdf, please convert to the accepted file type that allows the highest quality having 900-1200 dpi (resolution).
- Artwork is of high quality (correct resolution, not blurred, stretched or pixelated)

Headings

Please use no more than three levels of displayed headings.
Main heading should be bold with the font size 12-point Times Roman and sub headings should be 10-ponit Times New Roman and Bold.

Abbreviations

Abbreviations should be defined at first mention and used consistently thereafter.

Footnotes

Footnotes can be used to give additional information, which may include the citation of a reference included in the reference list. They should not consist solely of a reference citation, and they should never include the bibliographic details of a reference. They should also not contain any figures or tables.
Footnotes to the text are numbered consecutively; those to tables should be indicated by superscript lower-case letters (or asterisks for significance values and other statistical data). Footnotes to the title or the authors of the article are not given reference symbols.
Always use footnotes instead of endnotes.

Acknowledgments

Acknowledgments of people, grants, funds, etc. should be placed in a separate section on the title page. The names of funding organizations should be written in full.

Additional Information Text Formatting

All manuscripts should be formatted containing continuous line numbering. Use the page and line numbering function to number the pages.

References

APA Citation Style Guide (7th Ed.)

Citation

Cite references in the text by name and year in parentheses. Some examples:
Negotiation research spans many disciplines (Thompson, 1990).
This result was later contradicted by Becker and Seligman (1996).
This effect has been widely studied (Derwing, Rossiter, & Munro, 2002; Krech Thomas, 2004)

Reference list

The list of references should only include works that are cited in the text and that have been published or accepted for publication. Personal communications and unpublished works should only be mentioned in the text.

If available, please always include DOIs as full DOI links in your reference list (e.g. "https://doi.org/abc").

- **Journal article**
  Derwing, T. M., Rossiter, M. J., & Munro, M. J. (2002). Teaching native speakers to listen to foreign-accented speech. *Journal of Multilingual and Multicultural Development,* 23(4), 245-259.

- **Article by DOI**
  David, H., & Juyuan, J. (2013). A study of smog issues and PM 2.5 pollutant control strategies in China. *Journal of Environmental Protection*, 21(3), 16-21 DOI:10.4236/jep.2013.47086
- **Book**
  Referring a book should follow format: Author, Initial. (Year). Book title. City of publication, Country/State: Publisher.
  Gazda, G. M., Balzer, F. J., Childers, W. C., Nealy, A. U., Phelps, R. E., & Walters, R. P. (2005). *Human relations development: A manual for educators* (7th ed.). Boston, MA: Pearson Educational
- **Book chapter**
  Easton, B. (2008). Does poverty affect health? In K. Dew & A. Matheson (Eds.), *Understanding health inequalities in Aotearoa New Zealand* (pp. 97–106). Dunedin, New Zealand: Otago University Press.
- **Dissertation**
  Krech Thomas, H. (2004). Training strategies for improving listeners' comprehension of foreign-accented speech (Doctoral dissertation). University of Colorado, Boulder.

Statements & Declarations

The following statements must be included in your submitted manuscript under the heading 'Statements and Declarations'. This should be placed after the References section. Please note that submissions that do not include required statements will be returned as incomplete.

Funding

Please describe any sources of funding that have supported the work. The statement should include details of any grants received (please give the name of the funding agency and grant number).

Example statements:

"This work was supported by […] (Grant numbers […] and […]). Author A.B. has received research support from Company A."

"The authors declare that no funds, grants, or other support were received during the preparation of this manuscript."

Competing Interests

Authors are required to disclose financial or non-financial interests that are directly or indirectly related to the work submitted for publication. Interests within the last 3 years of beginning the work (conducting the research and preparing the work for submission) should be reported. Interests outside the 3-year time frame must be disclosed if they could reasonably be perceived as influencing the submitted work.
Example statements:
"Financial interests: Author A and B declare they have no financial interests. Author C has received speaker and consultant honoraria from Company M. Dr. C has received speaker honorarium and research funding from Company M and Company N. Author D has received travel support from Company O. Non-financial interests: Author D has served on advisory boards for Company M and Company N."
"The authors have no relevant financial or non-financial interests to disclose."
Please refer to the "Competing Interests" section below for more information on how to complete these sections.